The impact of inflammation, hypoxia, and vasculopathy on pain development in the α-galactosidase A mouse model of Morbus Fabry

Der Einfluss von Inflammation, Hypoxie und Vaskulopathie auf die Schmerzentwicklung des Morbus Fabry-spezifischen α-Galaktosidase A Mausmodells

Doctoral thesis for a doctoral degree

at the Graduate School of Life Sciences,

Julius-Maximilians-Universität Würzburg,

Section Neuroscience

submitted by

Marlene Spitzel

from

Munich

Würzburg 2023

Submitted on: ……

Office stamp

Members of the *Promotionskomitee*:

Chairperson: Prof. Dr. David Stegner

Primary Supervisor: Prof. Dr. Claudia Sommer

Supervisor (Second): Prof. Dr. Nurcan Üçeyler

Supervisor (Third): Prof. Dr. Robert Blum

Supervisor (Fourth): Prof. Carmen Ruiz de Almodóvar

Date of Public Defense: ……

Date of Receipt of Certificates: ……...

Affidavit

I hereby confirm that my thesis entitled **"The impact of inflammation, hypoxia, and vasculopathy on pain development in the α-galactosidase A mouse model of Morbus Fabry"** is the result of my own work. I did not receive any help or support from commercial consultants. All sources and / or materials applied are listed and specified in the thesis.

Furthermore, I confirm that this thesis has not yet been submitted as part of another examination process neither in identical nor in similar form.

……..

Place, Date Signature

Eidesstattliche Erklärung

Hiermit erkläre ich an Eides statt, die Dissertation **„Der Einfluss von Inflammation, Hypoxie und Vaskulopathie auf die Schmerzentwicklung des Morbus Fabry-spezifischen α-Galaktosidase A Mausmodells"** eigenständig, d.h. insbesondere selbständig und ohne Hilfe eines kommerziellen Promotionsberaters, angefertigt und keine anderen als die von mir angegebenen Quellen und Hilfsmittel verwendet zu haben.

Ich erkläre außerdem, dass die Dissertation weder in gleicher noch in ähnlicher Form bereits in einem anderen Prüfungsverfahren vorgelegen hat.

……..

Ort, Datum Unterschrift

Table of contents

Parts of the presented results in this thesis were published:

Spitzel M., Wagner E., Breyer M., Henniger D., Bayin M., Hofmann L., Mauceri D., Sommer C., Üçeyler N. (2022). Dysregulation of Immune Response Mediators and Pain-Related Ion Channels Is Associated with Pain-like Behavior in the GLA KO Mouse Model of Fabry Disease. *Cells 11*(11), 1730.

Published manuscripts and this thesis contain similar text passages and figures in adapted version in some sections (marked).

Parts of the presented methods and results were acquired during the doctoral thesis project “Untersuchung von Inflammation und Globotriaosylceramid-Ablagerungen im α-Galaktosidase A-defizienten Mausmodell von M. Fabry” of Elise Wagner, Cand. med.

1. Abstract

Fabry disease (FD), an X-linked lysosomal storage disorder, is caused by variants in the gene α-galactosidase A (*GLA*). As a consequence, the encoded homonymous enzyme GLA is not produced in sufficient amount or does not function properly. Subsequently, globotriaosylceradmide (Gb3), the target substrate of GLA, starts accumulating in several cell types, especially neurons and endothelial cells. FD patients suffer from multiorgan symptoms including cardiomyopathy, nephropathy, stroke, and acral burning pain. It is suggested that the impact of pathological Gb3 accumulation, inflammatory and hypoxic processes, and vasculopathy are contributing to the specific FD pain phenotype. Thus, we investigated the role of inflammation, hypoxia, and vasculopathy on molecular level in dorsal root ganglia (DRG) of the GLA knockout (KO) mouse model. Further, we investigated pain-like characteristics of GLA KO mice at baseline (BS), after capsaicin administration, and after repeated enzyme replacement therapy (ERT) administration for a period of 1.5 years. Acquired data showed disturbances in immune response markers represented by downregulated inflammation-associated genes and lower numbers of $CD206^{+}$ macrophages in DRG of GLA KO mice. Hypoxic mechanisms were active in DRG of GLA KO mice reflected by increased gene expression of hypoxia- and DNA damage-associated targets, higher numbers of hypoxia-inducible factor 1α-positive ($HIF1α^{+}$) and carbonic anhydrase 9-positive ($CA9^{+}$) neurons in DRG of GLA KO mice, and DRG neuronal HIF1α cytosolic-nuclear translocation in GLA KO mice. Vascularization in DRG of GLA KO mice was reduced including lower numbers of blood vessel branches and reduced total blood vessel length. Pain-like behavior of the GLA KO mouse model revealed no mechanical hypersensitivity at BS but age-dependent heat hyposensitivity, which developed also age-matched wild type (WT) mice. Capsaicin administration under isoflurane anesthesia did not elicit the development of nocifensive behavior in GLA KO mice after mechanical or heat stimulation. Repeated ERT administration did not show a clear effect in GLA KO mice in terms of restored heat hyposensitivity to BS paw withdrawal latencies. In summary, we demonstrated the impact of disturbed immune response markers, active hypoxic mechanisms, and reduced vascularization on molecular FD pathophysiology.

2. Zusammenfassung

Morbus Fabry (M. Fabry oder Fabry disease, FD) ist eine X-chromosomal vererbte, lysosomale Speichererkrankung, die durch Varianten im Gen α-Galaktosidase A (*GLA*) verursacht wird. Das durch *GLA* kodierte gleichnamige Enzym GLA kann somit nicht in ausreichender Menge produziert werden oder erhält nicht die volle Funktionalität. Als Folge akkumuliert das Glykosphingolipid Globotriaosylceramid (Gb3), welches das Zielsubstrat von GLA ist und durch dieses Enzym normalerweise abgebaut wird. Gb3 Akkumulationen sind in verschiedenen Zelltypen zu finden, jedoch bevorzugt in Neurone und Endothelzellen. FD-Patienten leiden unter Symptome, die verschiedene Organe betreffen, insbesondere Kardiomyopathien, Nephropathien, Schlaganfälle, und brennende Schmerzen in den Extremitäten. Es wird vermutet, dass neben dem pathologischen Einfluss der Gb3 Ablagerungen auch inflammatorische und hypoxische Prozesse und Vaskulopathien zum spezifischen FD-Schmerzphänotyps beitragen. Daher wurde die Rolle der Inflammation, Hypoxie und Vaskulopathie auf molekularer Ebene in Spinalganglien (dorsal root ganglion, DRG) eines FD-spezifischen GLA knockout (KO) Mausmodells untersucht. Des Weiteren wurde der Schmerz-ähnliche Phänotyp in GLA KO Mäusen unter nativen Bedingungen, nach Capsaicingabe und unter Enzymersatztherapie (enzyme replacement therapy, ERT) während einer Dauer von 1,5 Jahren untersucht. Unsere erhobenen Daten zeigten eine Beeinträchtigung von Faktoren der Immunantwort, die sich durch herunterregulierter Genexpression Inflammations-assoziierter Gene und einer geringeren Anzahl an $CD206^+$ Makrophagen in DRG von GLA KO Mäusen nachweisen ließ. Zu aktiven Hypoxiemechanismen trugen eine hochregulierte Genexpression Hypoxie- und DNA-Schäden-assoziierter Gene, eine höhere Anzahl an hypoxia-inducible factor 1α-positiver ($HIF1α^+$) und carbonic anhydrase 9-positiver ($CA9^+$) Neurone in DRG von GLA KO Mäusen, und die DRG neuronale HIF1α Translokation zwischen Zytosol und Nukleus bei. Die Vaskularisierung der DRG in GLA KO Mäusen war reduziert zusätzlich zu der geringeren Anzahl an Blutgefäßverzweigungen und einer Reduzierung der gesamten Blutgefäßlänge. Die Untersuchungen des nativen Schmerz-ähnlichen Verhaltens der GLA KO Mäuse zeigte keine Entwicklung mechanischer Hypersensitivität, während sich eine Hitzehyposensitivität mit steigendem Alter der Tiere entwickelte, die sich auch in altersangepassten Wildtyp (WT) Mäusen zeigte. Eine Capsaicingabe unter Isoflurannarkose zeigte keine erhöhte Sensitivität der GLA KO Mäuse nach mechanischer oder Hitzestimulation. Wiederholte

ERT-Gaben zeigten keine Verbesserung der Hitzehyposensitivität auf ein natives Niveau der Pfotenrückzuglatenz. Wir konnten den Einfluss beeinträchtigter Faktoren der Immunantwort, aktiver Hypoxieprozesse und reduzierter Vaskularisierung in DRG von GLA KO Mäusen auf die molekulare FD-Pathophysiologie zeigen.

3. Introduction

3.1 Fabry disease (FD)

3.1.1 Genetics

Fabry disease (FD) is a hereditary X-chromosomal lysosomal storage disorder with a prevalence between 1:40 000 and 1:117 000 (Burand & Stucky, 2021). Different variants in the gene α-galactosidase A (*GLA*) causes malfunction or insufficient production of the homonymous enzyme GLA (Burand & Stucky, 2021; Germain et al., 2022). GLA is a glucoside hydrolase localized in lysosomes of several cell types and degrades the glycosphingolipids globotriaosylceramide (Gb3) and its deacetylated form globotriaosylsphingosine (lyso-Gb3) (Germain et al., 2022; Kok et al., 2021). Based on the involved type of genetic mutation including deletions, insertions, frameshifts, duplications, missense and nonsense mutations, and splicing deficits ((Saito et al., 2011), fabry-database.org, last access: 19.07.2023), FD genetic variants can be distinguished between five different classifications: (1) pathogenic, (2) likely pathogenic, (3) uncertain significance, (4) likely benign, or (5) benign (Richards et al., 2015). Such genetic classification is reflected in the FD clinical phenotype as “classic” and “late-onset” phenotype (Arends et al., 2017; Germain et al., 2022). Classical FD presents early childhood manifestation with life-progression of nephropathy, cardiomyopathy, and neurological symptomatic, while “late onset” FD shows a less severe phenotype, mostly with clinical involvement of one organ. Another possibility to classify FD-specific variants is based on the localization of the resulting amino acid exchange in the tertiary structure of GLA. Variants resulting in alterations at the active site or buried areas of the enzyme are associated with a severe clinical FD phenotype (Rickert et al., 2020).

3.1.2 Clinical phenotype

Due to non-proper degradation of Gb3, as main target substrate of GLA, Gb3 accumulation occurs in lysosomes of several cell types with a preference for kidney cells, endothelial and smooth muscle cells, and neurons (Tuttolomondo et al., 2021). Consequently, FD patients suffer from multiorgan symptoms (Simonetta et al., 2020) including nephropathy, cardiomyopathy, cerebral stroke, and microvasculopathy (Tuttolomondo et al., 2021). Further symptoms can also involve the gastrointestinal tract, the skin in terms of angiokeratomas and dyshidrosis, the ears and eyes in terms of tinnitus and cornea verticillata, respectively, and a psychiatric phenotype like depression (Mehta et al., 2010). Additionally, small fiber neuropathy (SFN) is present in FD patients and is related to episodic pain attacks displayed as acral burning pain, thermal hypo- and mechanical hypersensitivities triggerable via heat, fever, or physical activity (Üçeyler et al., 2014; Üçeyler et al., 2013; Weissmann et al., 2021). Molecular pathomechanisms of FD are still not fully understood (Simonetta et al., 2020; Tuttolomondo et al., 2021), but besides the contribution of pathological Gb3 accumulation, several systemic components involving inflammatory (Rozenfeld & Feriozzi, 2017), hypoxic, and vascular impairment (Lorenzen et al., 2013; Mishra et al., 2020) are proposed to contribute, in parallel to impaired GLA enzymatic activity and Gb3 accumulation, to the specific molecular and phenotypical FD profile.

3.1.3 Treatment options

Dependent on specific gene variants present in *GLA*, chaperone therapy with orally administered Migalastat (Galafold®, Amicus Therapeutics, Philadelphia, PA, USA) is used to restore misfolded GLA proteins. Based on the localization of the variant, folding properties in the tertiary structure of GLA can be impaired leading to an abolished functionality of the enzyme itself. Chaperones are molecular scaffolds supporting the process of protein folding and structural rearrangement to restore proper degradational function of enzymes (Weidemann et al., 2022). Nevertheless, this therapy option is only suitable for FD patients carrying *GLA* variants, which affect directly the 3D protein structure of GLA. Another treatment option for FD patients with other gene variants in *GLA* are two differently produced recombinant GLA enzyme agents, which are administered intravenously. One agent is agalsidase α (Replagal®, Takeda Pharmaceutical, Tokyo, Japan), which is produced in human fibroblasts, while the other agent is agalsidase β (Fabrazyme®, Sanofi Genzyme, Cambridge, MA, USA) being produced in Chinese ovary cells. Both ERT agents ensure a sufficient supply with GLA enzyme targeting accumulated Gb3 in different cell types (Lee et al., 2003; Oder et al., 2021). The kinetics and efficacy of both agalsidase α and β are very similar (Lee et al., 2003). The majority of studies on FD patients showed reduction of Gb3 and lyso-Gb3 load in plasma, urine, and cardiac cells, while other studies report differential effects of ERT on Gb3 load reduction dependent on the usage of either agalsidase α or β and the duration of ERT administration (Germain et al., 2019). ERT administration in FD rodent models showed a reduction of Gb3 and lyso-Gb3 in various tissues including heart, kidney, and liver, but not in brain tissue and no alleviation of pain-like behavior regarding thermal and mechanical thresholds (Ashe et al., 2015; Marshall et al., 2010). While some FD patients receiving ERT show improvement of various symptoms including nephropathy, cardiomyopathy, and pain, other FD patients do not show improved thermal or mechanical detection thresholds (Germain et al., 2019; Üçeyler et al., 2011). ERT has some limitations like infusion adverse reactions, development of antibodies against ERT or limited molecular passage of ERT through the blood-brain-barrier (Azevedo et al., 2020). For some FD patients, treatment with non-steroidal anti-inflammatory drugs (NSAID) yields transient alleviation of pain symptoms, suggesting a potential impact of inflammatory processes in FD pain pathophysiology (Politei et al., 2016; Rozenfeld & Feriozzi, 2017; Üçeyler et al., 2014) or potential stabilization properties of e.g., acetylsalicylic acid on chaperones used to

refold GLA for proper functionality (Monticelli et al., 2022). Other treatment options are in pre-clinical and clinical studies like plant-derived ERT (Pegunigalsidase α®, Protalix Biotherapeutics, Carmiel, Israel and moss-aGal®, Greenovation biopharmaceuticals, Freiburg, Germany) or substrate reduction therapy (SRT, Venglustat®, Sanofi Genzyme, Cambridge, MA, USA and Lucerastat®, Idorsia Pharmaceuticals, Allschwill, Switzerland) (Oder et al., 2021). The idea behind SRT is to reduce the initial production of Gb3 via inhibiting glucosylceramide synthase, which is involved in Gb3 anabolism, resulting into more balanced tissue Gb3 levels (Ashe et al., 2015; Kok et al., 2021). Beside specific treatment options for FD pathology, it is recommended to symptomatically treat clinical symptoms like nephropathy, cardiomyopathy and neurological complications with available options according to the Fabry S1-Leitlinie of the German Society for Neurology (Deutsche Gesellschaft für Neurologie; Üçeyler et al., Diagnose und Therapie des Morbus Fabry, S1-Leitlinie, 2022; in: Deutsche Gesellschaft für Neurologie (Hrsg.), Leitlinien für Diagnostik und Therapie in der Neurologie. Online: https://dgn.org/leitlinie/interdisziplinare-leitlinie-fur-die-diagnose-und-therapie-des-morbus-fabry (last access: 03.08.2023)) to minimize multiorgan complications and maximize the life-expectancy of FD patients.

So far, sufficient therapy for FD patients is highly individual and still lacking. Thus, this study aimed to investigate molecular pathomechanisms involving inflammatory and hypoxia pathways, and vascular characteristics to understand better their role in the development of FD pathophysiology and to find further potent druggable targets for FD therapy.

3.2 Inflammatory contribution to FD

Several studies reported the contribution of inflammatory processes in FD as potential immune response against pathological Gb3 accumulation (Mauhin et al., 2015; Rozenfeld & Feriozzi, 2017). Human studies using isolated FD patients' peripheral blood mononuclear cells (PBMC) found pro-inflammatory profiles represented by upregulated gene and protein expression of tumor necrosis factor alpha (TNFα), toll-like receptor 4 (TLR4), and interleukin-1beta (IL-1β). Gb3 accumulation seems to directly induce pro-inflammatory mechanisms via TNFα and TLR4 activation (De Francesco et al., 2013; Üçeyler et al., 2019). In parallel studies using FD animal models, similar findings on the impact of immune response components of FD pathomechanisms were reported. In a FD rat model, higher numbers of macrophages and T-cells in skin were found (Miller et al., 2019), while gene expression analysis of differentially regulated mRNA in a FD mouse model revealed downregulation of genes involved in immune response-related pathways in murine DRG (Kummer et al., 2017). Our study aimed to investigate the role of inflammatory processes and key players specifically in the FD mouse model GLA knockout (KO) mouse on gene and protein expression level.

3.3 Vasculopathy and hypoxia in FD

Clinical studies in FD patients reported vasculopathies affecting different organs including e.g., the heart, kidney, and brain (Lorenzen et al., 2013; Mishra et al., 2020; Tapia et al., 2021). In a magnetic resonance imaging (MRI) study, FD patients reduced perfusion of DRG (Godel et al., 2017). In *in vitro* studies and studies with FD animal models, altered endothelial cell functionality and morphology was reported (Choi et al., 2023; Park et al., 2008; Pollmann et al., 2021; Shen et al., 2007), suggesting the subsequent involvement of activated hypoxic mechanisms to counteract insufficient tissue blood supply and promote angiogenesis (Lin et al., 2011). Together with potential inflammatory responses to Gb3 accumulation, vasculopathy and hypoxia enter a vicious cycle worsening each other's effect systemically in FD patients and FD cellular and animal models (Taylor & Colgan, 2017). The effects of hypoxia mechanisms in FD pathophysiology have hardly been investigated. Only one study reported reduced blood flow and a relative hypoxic state of the extremities in FD

patients (Inagaki et al., 1992). Thus, this work aimed to investigate the role of vascular properties and hypoxic pathways in DRG of GLA KO mice in more depth.

3.4 Experimental *in vitro* and animal models of FD

Due to limitations in biomaterial availability, especially of nervous tissue, FD *in vitro* and animal models were developed. Among FD *in vitro* models, induced pluripotent stem cell (iPSC) lines can be generated from PBMC (Cui et al., 2021; Zhu et al., 2021) or FD-patients' skin punch biopsies (Breyer et al., 2022; Duarte et al., 2020; Klein et al., 2018; Qin et al., 2023) and used for molecular experimental approaches. To investigate neuropathic characteristics of FD in more detail, FD patients' iPSC-derived neurons or neuronal cell cultures from rodent FD models are widely used as *in vitro* models (Choi et al., 2015; Hofmann et al., 2018; Kaneski et al., 2022a, 2022b; Miller et al., 2018; Namer et al., 2017). For systemic experimental approaches, FD animal models including *Drosophila* fruit flies (Braunstein et al., 2020), zebrafish (Elsaid, Furriol, et al., 2022; Elsaid, Tjeldnes, et al., 2022), rat (Kanack et al., 2021; Miller et al., 2019; Miller et al., 2018; Waltz et al., 2021), and mouse models (Ishii et al., 2020; Ohshima et al., 1997), mimicking FD pathophysiology at different levels, are used for molecular and behavioral investigations. While *Drosophila* and zebrafish are best to investigate genomic and molecular mechanisms (Braunstein et al., 2020; Elsaid, Tjeldnes, et al., 2022), rodent models are more common for systemic approaches (Ashe et al., 2015; Hofmann et al., 2018; Marshall et al., 2010; Miller et al., 2018; Namer et al., 2017; Üçeyler et al., 2016). To mimic the FD pathology, a knockin/knockout (KI/KO) mouse model was developed by knocking in the Gb3 synthase and knocking out Gb3 (Maruyama et al., 2018; Shiozuka et al., 2011; Taguchi et al., 2013). This model shows similar clinical symptoms like seen in FD patients including elevated Gb3 levels in major organs like heart, kidney, liver, and brain tissue and a FD-like phenotype including renal and cardiac dysfunction (Taguchi et al., 2023; Taguchi et al., 2013). A negative aspect of the KI/KO mouse model is that while in human FD pathology only GLA is genetically altered, in this model the Gb3 synthase is also impaired (Kok et al., 2021). Other rodent models like the GLA KO rat and mouse model display a milder FD phenotype including lower levels of Gb3 in major organs and a milder pain-like phenotype (Ashe et al., 2015; Hofmann et al., 2018; Marshall et al., 2010; Miller et al., 2018; Namer et al., 2017). Nevertheless, the pain-like phenotype

and molecular FD characteristics in FD rodent models sufficiently mimic human FD pathophysiology to make these *in vivo* models suitable to investigate the involvement of the nervous system in FD pathophysiology.

3.5 Pain-like characteristics of the GLA KO mouse model

Different FD animal models are used to unravel molecular pathomechanisms of FD. One well characterized model is the GLA KO mouse model (Ohshima et al., 1997). The GLA KO mouse has been used by several investigators and shows some phenotypic and genotypic characteristics also seen in FD patients. The GLA KO mouse model was generated with total *GLA* gene KO in all cell types resulting into Gb3 accumulation in kidney cells, endothelial cells, and DRG neurons (Jabbarzadeh-Tabrizi et al., 2020). Further, GLA KO mice show reduced intraepidermal nerve fiber densities (IENFD), increased transient receptor potential vanilloid 1 (TRPV1) protein expression in DRG, and age-dependent heat hyposensitivity, cold hyposensitivity, and mechanical hypersensitivity mimicking findings reported in FD patients (Hofmann et al., 2018; Lakoma et al., 2016; Spitzel et al., 2022; Üçeyler et al., 2016). The GLA KO mouse model is also used to investigate effects of different treatment options including ERT with recombinant GLA agalsidase α and β (Ashe et al., 2015; Marshall et al., 2010). The efficacy of ERT especially on alleviating neuropathy in FD is not fully unraveled. Thus, we aimed to perform extensive assessments of the GLA KO behavioral profile with GLA KO mice receiving capsaicin, at different doses, as TRPV1 agonist to elicit nocifensive behavioral reactions. Further, we aimed to assess the effect of ERT over the mice's lifespan and investigated the behavioral profile and potential alleviation under treatment.

3.6 Aim of the study

We aimed to investigate molecular pathomechanisms involving inflammation, hypoxia, and malperfusion in DRG of the GLA KO mouse model to unravel molecular key players contributing to the FD-specific profile on molecular, morphological, and behavioral levels.

We hypothesized that:

1) Inflammatory and hypoxic molecular mechanisms interfere reciprocally on DRG level of GLA KO mice
2) This results in malperfusion of the DRG level in GLA KO mice
3) A nocifensive pain profile develops in GLA KO mice
4) The nocifensive pain profile of GLA KO mice is triggerable and rescuable via capsaicin and ERT administration, respectively.

4. Materials and Methods

4.1 GLA KO mouse model

GLA KO mice and respective WT littermates were used for all *in vivo* and *in vitro* studies. To ensure an identical genetic background in GLA KO and WT mice, heterozygous GLA KO/WT female mice were cross bred with hemizygous WT/- male mice for the F1 offspring generation. Obtained F1 offspring was crossbred as follows: For the GLA KO line homozygous GLA KO female and male mice were crossbred. For the WT line homozygous WT female and male mice were crossbred. Resulting F2 offspring was used for all approved *in vivo* experiments and for tissue collection needed for *in vitro* analysis. To ensure the correct genotype of each offspring, ear punch biopsies were analyzed with the Taq PCR Master Mix Kit (Qiagen, Hilden, Germany) using the following primers: oIMR5947, AGGTCCACAGCAAAGGATTG; oIMR5948, GCAAGTTGCCCTCTGACTTC; oIMR7415, GCCAGAGGCCACTTGTGTAG (Invitrogen, Carlsbad, CA, USA). GLA KO breeding and animal experiments were approved by the Bavarian state authorities (Regierung von Unterfranken, #1052-22, #1053-18). Animals were kept at the of the Centre for Experimental Molecular Medicine (Zentrum für Experimentelle Molekulare Medizin, ZEMM), University of Würzburg, Germany. Commercially available standard chow and water were available *ad libitum*.

4.2 Tissue collection

Animals were anesthetized with 4% isoflurane (CP-Pharma, Burgdorf, Germany) and exsanguinated. By opening the sciatic nerve and following up until it splits up into three branches innervating L3-5 DRG, L4 DRG were collected in tubes for qRT PCR analysis, while L3 and L5 DRG were embedded in cryomolds filled with optimal cutting temperature medium (Tissue-Tek® O.C.T.™ Compound, Sakura Finetek, Tokyo, Japan) for immunohistological analysis (Fig. 1). Tissue was flash-frozen in liquid nitrogen-cooled 2-methylbutane (Carl Roth, Karlsruhe, Germany) and stored at -80°C upon further processing.

For DRG neuronal cell cultures, animals were euthanized as described above. The whole spine was removed and cut into two halves in the sagittal plane. The now visible spinal cord was gently shifted aside to reveal the DRG located within the intervertebral foramina. After removing the surrounding meninges, DRG were grabbed gently by the

dorsal root and pulled out of the intervertebral foramina. DRG were collected in a tissue culture dish with ice-cold DRG medium containing DMEM/F-12 + GlutaMAX™ (Thermo Fisher Scientific, Waltham, MA, USA), 100 U/ml penicillin-100 µg/ml streptomycin (PenStrep, Thermo Fisher Scientific, Waltham, MA, USA), and 10% fetal calf serum (FCS, Merck, Darmstadt, Germany), were cleaned from attached dorsal and ventral root, and transferred into a tube filled with ice-cold DRG medium for further processing according to the DRG neuronal cell culture protocol in the next section 4.3.

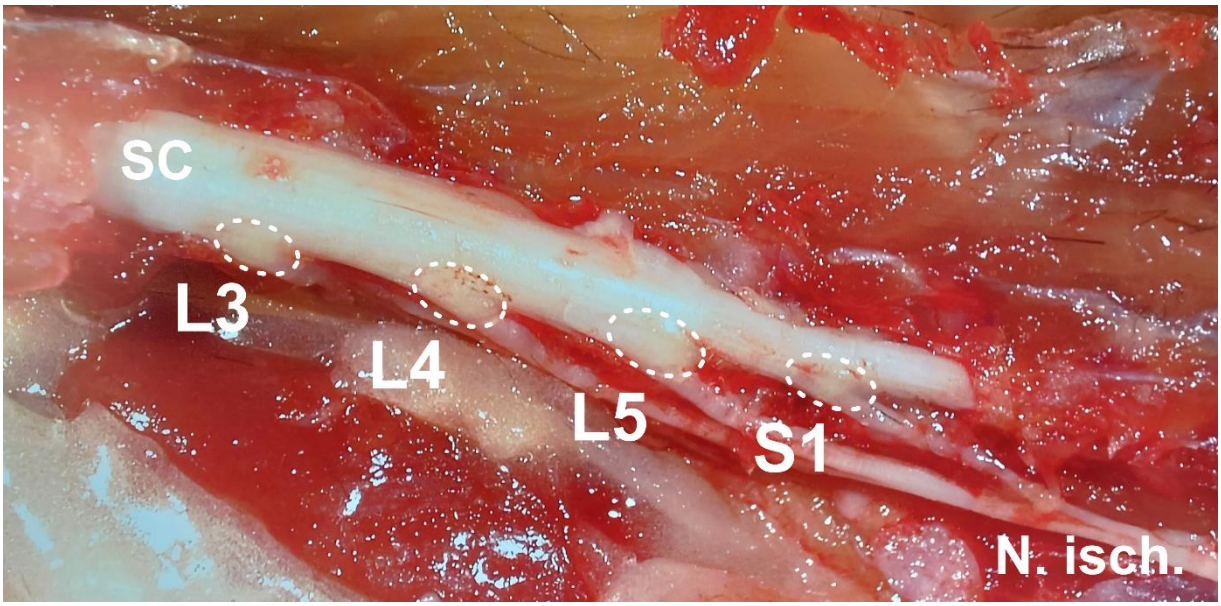

Figure 1: Anatomic overview of dissected murine L3, L4, L5, and S1 DRG.
Representative anatomic overview of L3, L4, L5, and S1 DRG (white dotted line) localization of a WT mouse attached to the spinal cord (SC). The Nervus ischiadicus (N.isch.) is depicted in the lower right corner splitting disto-proximally and innervating the marked DRG. Abbreviations: DRG: dorsal root ganglion; L3/4/5 DRG: lumbar 3/4/5 DRG; N.isch.: Nervus ischiadicus; S1 DRG: sacral 1 DRG; SC: spinal cord.

4.3 DRG neuronal cell culture protocol

Collected DRG were spun down in a centrifuge (Eppendorf centrifuge 4517R, Eppendorf, Hamburg, Germany) at 3000 revolutions per minute (rpm) for 3 min at room temperature (RT), followed by incubation with DMEM/F-12 + GlutaMAX™ and 1.92 mg/ml Liberase TH enzyme (Roche, Basel, Switzerland) in a thermo shaker (PCMT Grant Bio, Grant Instruments Ltd., Cambridgeshire, UK) at 37°C and 900 rpm for 30 min. After another spin-down step at RT and 3000 rpm for 3 min, DRG were incubated with DMEM/F-12 + GlutaMAX™ and 1.92 mg/ml Liberase TM enzyme (Roche, Basel, Switzerland) in a thermos shaker at 37°C and 900 rpm for 10 min. After 3 min at RT and 3000 rpm in a centrifuge, detached DRG neurons were dissociated in 1 ml pure DMEM/F-12 + GlutaMAX™ and pipetted slowly into a 15 ml tube on top of 7.5 ml 3.5% bovine serum albumin (BSA)/DMEM/F-12 + GlutaMAX™ solution until two separate phases were visible with the top phase containing the DRG neurons ready to be filtered through the BSA/DMEM/F-12 + GlutaMAX™ solution. The tubes placed in a centrifuge (Rotina 420R, Hettich, Tuttlingen, Germany) for 10 min at RT and 500 rpm. The DRG neuron pellet was dissociated in DRG medium plus 10 µg/ml nerve growth factor (NGF, Alomone Labs, Jerusalem, Israel). DRG neurons were cultivated in 4-well plates (Greiner Bio One, Frickenhausen, Germany) on poly-D-lysine/laminin-coated coverslips (Corning Inc., Corning, NY, USA) in 1 ml DRG medium + NGF at 37°C in a cell culture incubator (HERAcell™ VIOS 150i CO_2 incubator, Thermo Fisher Scientific, Waltham, MA, USA) for at least 24 h until further experiments.

4.4 *In vitro* hypoxia experiments on DRG neuronal cell cultures

To mimic a hypoxic environment, we built a hypoxia chamber of acrylic glass (300 x 200 x 160 mm) in modified version according to (Wang et al., 2014) (Fig. 2). DRG neuronal cell cultures of old WT and GLA KO mice were placed into the hypoxia chamber, which was sealed with gas-tight tape (DIOP, Rosbach, Germany) and filled via implemented valves with a 2% O_2 hypoxia gas mixture (2% O_2, 5% CO_2, 93% N_2 [v/v], Rießner Gase GmbH, Lichtenfels, Germany) for 2 min. The prepared chamber containing DRG neuronal cell cultures was kept for 24 h in an incubator at 37°C. As control, DRG neuronal cell cultures from old WT and GLA KO mice were kept for 24 h at 37°C in an incubator at normoxic conditions (21% O_2, 5% CO_2, 74% N_2 [v/v], Rießner Gase GmbH, Lichtenfels, Germany). After 24 h, DRG neuronal cell cultures were either

fixed with 4% PFA for immunocytochemistry (ICC) or lysed with QIAzol Lysis Reagent (miRNeasy mini Kit, Qiagen, Hilden, Germany) for gene expression analysis.

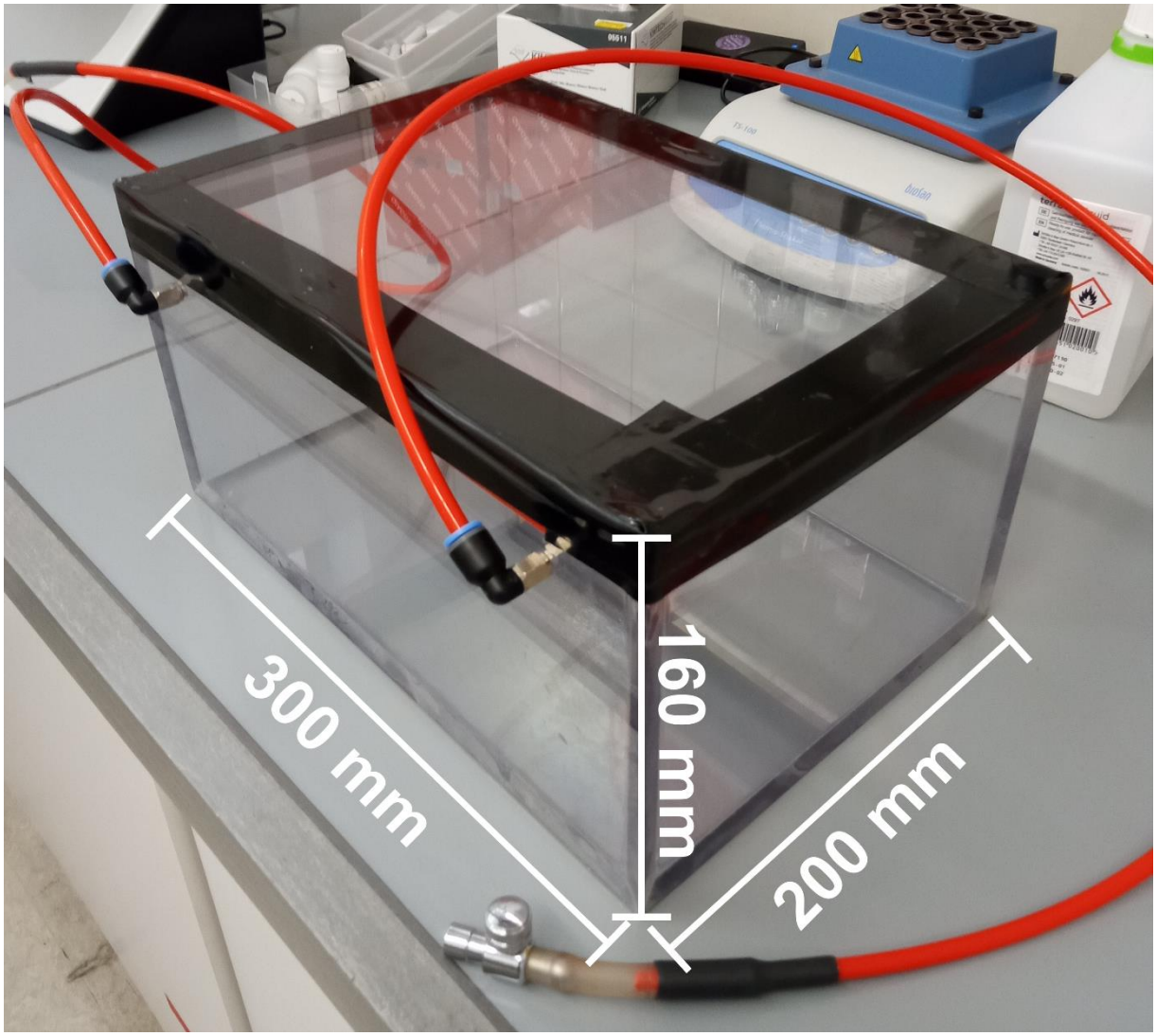

Figure 2: Hypoxia chamber for *in vitro* hypoxia experiments.
Customized hypoxia chamber (W: 200 mm; L: 300 mm; H:160 mm) used for *in vitro* hypoxia experiments with DRG neuronal cell cultures of WT and GLA KO mice with incorporated valves to fill the chamber with 2% O_2 gas mixture and sealed with gas-tight tape. Abbreviations: DRG: dorsal root ganglion; GLA KO: alpha-galactosidase A knockout; H: height; L: length; mm: millimeter; W: width. Hypoxia chamber construction in modified version according to (Wang et al., 2014).

4.5 Gene expression analysis

For RNA extraction of whole DRG, L3 and L5 DRG were pooled per animal and processed in QIAzol Lysis Reagent (miRNeasy mini Kit, Qiagen, Hilden, Germany) with the Polytron PT 3100 homogenizer (Kinematica, Luzern, Switzerland). For RNA extraction out of DRG neuronal cell culture, DRG neurons were lysed only using QIAzol Lysis Reagent. Further steps were applicable for whole DRG tissue and DRG neuronal cell culture. For RNA extraction, the miRNeasy mini Kit (Qiagen, Hilden, Germany) was used. Extracted RNA was reverse-transcribed into cDNA with TaqMan™ Reverse Transcription Reagents (Applied Biosystems, Darmstadt, Germany) (detailed reverse transcription reagents mixture and respective protocols are listed under section 8.9). Transcribed cDNA of whole DRG was used either as pooled samples for gene expression array analysis screening for inflammation- (TaqMan™ Array Mouse Immune Response, Applied Biosystems, Darmstadt, Germany) and hypoxia- (RT² Profiler PCR Array, Mouse Hypoxia Signaling Pathway, Qiagen, Hilden, Germany) associated target genes or as single samples for gene expression assay analysis (all tested target genes are listed in section 8.5 with respective IDs) validating single target gene expression. cDNA of DRG neuronal cell culture was used only for single gene expression assay analysis. Standard (0.1-ml) TaqMan™ Array Plates (Applied Biosystems, Darmstadt, Germany) were loaded with cDNA, TaqMan™ Fast Advanced Mastermix (Applied Biosystems, Darmstadt, Germany), specific mouse TaqMan™ Gene Expression Assays (Applied Biosystems, Darmstadt, Germany) tagged with FAM-MGB reporter dye and the endogenous control TaqMan™ Gene Expression Assay for ribosomal protein L13a (RPL13A) tagged with VIC-MGB reporter dye. qRT PCR plates were run with the StepOnePlus™ Real-Time PCR System (Applied Biosciences, Darmstadt, Germany) at following settings: 2 min, 50°C; 2 min, 95°C; (3 sec, 95°C; 30 sec, 60°C) 40x. qRT PCR raw data was acquired with the StepOne software v2.3 and relative gene expression was analyzed according to the ΔΔCt method (Livak & Schmittgen, 2001).

4.6 Immunocytochemistry (ICC)

For ICC, DRG neuronal cell cultures were fixed with 4% PFA for 15 min at RT and washed with phosphate-buffered saline (PBS, Sigma-Aldrich, St. Louis, MO, USA) three times for 5 min each. Neurons were blocked with 10% bovine serum albumin/phosphate-buffered saline (BSA/PBS, Sigma-Aldrich, St. Louis, MO, USA) for 30 min at RT and incubated with respective primary antibodies diluted in blocking solution plus either 0.1% saponin for extranuclear targets or 0.3% Triton-X for intranuclear targets at respective concentration over night at 4°C (used primary antibodies are listed under section 8.6). After three washing steps with PBS for 5 min each, DRG neuronal cell cultures were incubated with the respective secondary antibody diluted in blocking solution for 30 min at RT (used secondary antibodies are listed under section 8.6). Incubation with the nuclear staining agent DAPI diluted in the blocking solution for 5 min at RT and two washing steps with PBS for 5 min each at RT followed. Stained DRG neuronal cell cultures were preserved on microscope slides (R. Langenbrinck, Emmendingen, Germany) using Aqua-Poly/Mount (Polysciences, Warrington, PA, USA) and stored in the dark at 4°C until further processing. For further analysis, photomicrographs were acquired with a fluorescence microscope (Axio Imager M.2, Zeiss, Oberkochen, Germany) at the same exposure time and duration with a 20x objective.

4.7 Immunohistochemistry (IHC)

L4 DRG were cut in 10-µm (for Gb3 visualization and cell counting) or 50-µm (for blood vessel analysis) cryosections using a cryostat (Leica Microsystems, Wetzlar, Germany). Per animal, 3 sections were collected per slide and either stored at -20°C upon further processing or used immediately.

3,3'-diaminobenzidine (DAB) staining was performed by E.W. and for assessing immune cell infiltration rates in murine DRG. Therefore, 10-µm cryosections were fixed in acetone (Sigma-Aldrich, St. Louis, MO, USA) for 10 min at -20°C and blocked with 10% bovine serum albumin/tris-hydroxymethyl-aminomethane (BSA/Tris, Sigma-Aldrich, St. Louis, MO, USA) for 30 min at RT. Primary antibodies were diluted in 1% BSA/Tris and 2% milk powder (Sigma-Aldrich, St. Louis, MO, USA) and incubated over night at 4°C. Used primary antibodies and respective dilutions are listed under section 8.6. Cryosections were further washed three times with Tris for 5 min each and blocked

with methanol/30% hydrogen peroxide (H_2O_2) (Sigma-Aldrich, St. Louis, MO, USA) for 20 min at RT. Secondary antibodies were diluted in 1% BSA/Tris and 2% milk powder for 30 min at RT. Used secondary antibodies and respective dilutions are listed in under section 8.6. After 3 washing steps sections were treated with the Avidin/Biotin blocking kit and DAB substrate kit, peroxidase (with nickel) (both Vector Laboratories, Inc., Burlingame, CA, USA). Next, incubation with hematoxylin–eosin (Sigma-Aldrich, St. Louis, MO, USA) for 30 sec at RT to visualize nuclei and were dehydration with an ascending alcohol row and two washing steps with xylole (Carl Roth, Karlsruhe, Germany) for 10 min at RT followed. Sections were mounted with Vitro-Clud® (R. Langenbrick GmbH, Emmendingen, Germany) and stored at 4°C until further processing.

Immunofluorescence was performed to assess Gb3 load via fluorophore-coupled Shiga toxin 1, subunit B (STxB, Sigma Aldrich, St. Louis, MO, USA), hypoxia-positive neurons, and blood vessel properties in murine DRG. For Gb3 and cell count analysis, 10-µm sections were used, while 50-µm section were used for blood vessel analysis. Sections were fixed in acetone (Sigma-Aldrich, St. Louis, MO, USA) for 10 min at -20°C and blocked with 10% BSA/PBS (Sigma-Aldrich, St. Louis, MO, USA) for 30 min at RT. Primary antibodies were diluted in 1% BSA/PBS and 0.1% saponin (Sigma-Aldrich, St. Louis, MS, USA) for extranuclear targets and in 1% BSA and 0.3% Triton X (Sigma-Aldrich, St. Louis, MS, USA) for intranuclear targets overnight at 4 °C. Primary antibodies and their dilutions are listed under section 8.6. After three washing steps with PBS for 5 min each secondary antibodies were diluted in 1% BSA/PBS for 2 h at RT. Secondary antibodies and their dilutions are listed in under section 8.6. The staining was finalized with three washing steps, and cryosections were mounted with VECTASHIELD® containing the nuclear staining agent 4',6-diamidino-2-phenylindole (DAPI, Vector Laboratories, Berlingame, CA, USA). Stained sections were stored light-protected at 4°C upon further processing. For further analysis, photomicrographs were acquired with a bright field (DMi8 Leica Microsystems, Wetzlar, Germany) and fluorescence microscope (Axio Imager M.2, Zeiss, Oberkochen, Germany) at the same exposure time and duration with a 20x objective.

4.8 Intensity measurements and cell count analysis

4.8.1 Gb3 load assessment in DRG cryosections of WT and GLA KO mice

Gb3 accumulation in DRG cryosections of young and old WT and GLA KO mice was analyzed indirectly via STxB intensity measurement. Three 10-µm cryosections were analyzed per animal using ImageJ (Schindelin et al., 2012). The cell body-rich area was defined by the neuronal marker protein gene product 9.5 (PGP9.5) as region of interest (ROI). The ROI was applied on the StxB staining, mean intensity values were measured and compared between young and old WT and GLA KO mouse DRG. The GLA KO/WT ratio for young and old mice was calculated and used for further statistical analysis.

4.8.2 Nuclear HIF1α intensity measurement in DRG neurons of WT and GLA KO mice

For nuclear HIF1α intensity measurements, whole DRG cryosections and DRG neuronal cell cultures of WT and GLA KO mice were analyzed.

For whole DRG samples, three cryosections per animal were used of young and old WT and GLA KO mice and analyzed with ImageJ. The cell body-rich area (CBRA) was defined using peripherin (PRPH) staining. Nuclei stained with DAPI within the CBRA were used to define a ROI. The nuclei ROI was applied on the HIF1α staining and mean intensity values were measured for each nucleus located within the CBRA. HIF1α mean intensities of GLA KO mouse DRG were normalized to mean HIF1α intensities of age-matched WT mouse DRG and used for further statistical analysis.

For DRG neuronal cell cultures of old WT and GLA KO mice, five ROI were analyzed per experimental condition. Neurons within the predefined ROI were visualized via PGP9.5 staining, while nuclei were stained with DAPI and used to define a mask with ImageJ. The nucleus mask was applied on the HIF1α staining and mean intensities were measured within the nuclei. The mean of all intensity measurements within the five ROI per experimental condition was calculated and, normalized to WT DRG neuronal cell cultures cultivated under normoxia and used for further statistical analysis.

4.8.3 HIF1α$^+$ and CA9$^+$ cell count in whole DRG and DRG neuronal cell cultures of WT and GLA KO mice

For HIF1α$^+$ and CA9$^+$ neurons located in whole DRG, three 10-µm cryosections per animal were analyzed. Using ImageJ, the CBRA was defined as a ROI using the PRPH or β-III-tubulin staining. Within this ROI, HIF1α$^+$ and CA9$^+$ neurons were counted and normalized per mm² CBRA. Acquired data was used for further statistical analysis.

For HIF1α$^+$ and CA9$^+$ neurons in DRG neuronal cell cultures, five ROI were acquired per experimental condition. Total number of PGP9.5$^+$ neurons was assessed and used for normalization of HIF1α$^+$ and CA9$^+$ counted neurons per ROI. The percentage of positively counted neurons per PGP9.5$^+$ neurons in one ROI was calculated and used for further statistical analysis.

4.8.4 Immune cell count and analysis in whole DRG of WT and GLA KO mice

Immune cell infiltration rates were assessed by counting positively stained cells per mm² CBRA of whole DRG cryosections using ImageJ. Three 10-µm cryosections per animal were analyzed. CD3$^+$ (T-cell specific marker), CD11b$^+$ (pan-macrophages specific marker), F4/80$^+$ (pan-macrophages specific marker), CD80$^+$ (M1 pro-inflammatory specific marker), and CD206$^+$ (M2 anti-inflammatory specific marker) immune cells were counted within the defined CBRA and normalized to mm² CBRA. Acquired data was used further for statistical analysis.

4.8.5 Blood vessel analysis in DRG of WT and GLA KO mice

A set of morphological blood vessel characteristics was analyzed in three 10-µm cryosections per animal. CD31$^+$ blood vessels within the CBRA, defined by PRPH staining, were used to assess total blood vessel area, total blood vessel length, the number of blood vessel branching points and average blood vessel thickness. Additionally, total DRG area was measured. Blood vessel characteristics were normalized to mm² per CBRA.

4.9 Behavioral assessment

All tests were performed by the same investigator blinded to the genotype and treatment group (M.S.). Animals were placed into acrylic glass boxes one hour prior to the behavioral experiments to adapt to the testing environment.

4.9.1 Von Frey test

The von Frey test assesses mechanical withdrawal thresholds upon hind paw stimulation with different standardized von Frey filaments (Touch Test™ Monofilaments, FMI GmbH, Seeheim-Ober Beerbach, Germany) according to the up-and-down-method (Chaplan et al., 1994). Young (≤ 3 months) and old (> 6 months) WT and GLA KO mice were placed separately into acryl glass boxes on a wire mesh for accommodation until exploration and grooming behavior ceased (Fig. 3). The hind paws of the calm animals were stimulated with the 0.6 g von Frey filament for up to 3 sec. Upon paw withdrawal, the next thinner filament was applied for stimulation, while without any paw withdrawal reaction, the next thicker filament was applied. In total, six repeated measurement per hind paw were performed and analyzed according to (Chaplan et al., 1994).

Figure 3: Von Frey testing setup with mice placed within acrylic glass boxes on a wire mash plateau. Representative image of the von Frey setup for behavioral testing of mechanical sensitivities of young and old WT and GLA KO mice placed within acrylic glass boxes on a wire mash plateau. Mice spent 1 h before and during experimental examination within the boxes for adaption and experimental assessment. Abbreviations: GLA KO: alpha-galactosidase A knockout; h: hour; WT: wild type.

4.9.2 Hargreaves test

The Hargreaves test assesses paw withdrawal latencies upon heat stimulation of the hind paws. For accommodation to the setup, young and old WT and GLA KO mice were placed separately into acryl glass boxes on a glass plate until exploration and grooming behavior ceased (Fig. 4). The hind paws of the calm animals were stimulated with a radiant heat stimulus (25 IR) using a standard Ugo Basile Algometer (Ugo Basile Inc., Comerio, Italy). The stimulation lasted maximally up to 16 sec to avoid tissue damage. Six repeated measurement per hind paw were performed and the mean paw withdrawal latency per hind paw was calculated according to (Hargreaves et al., 1988).

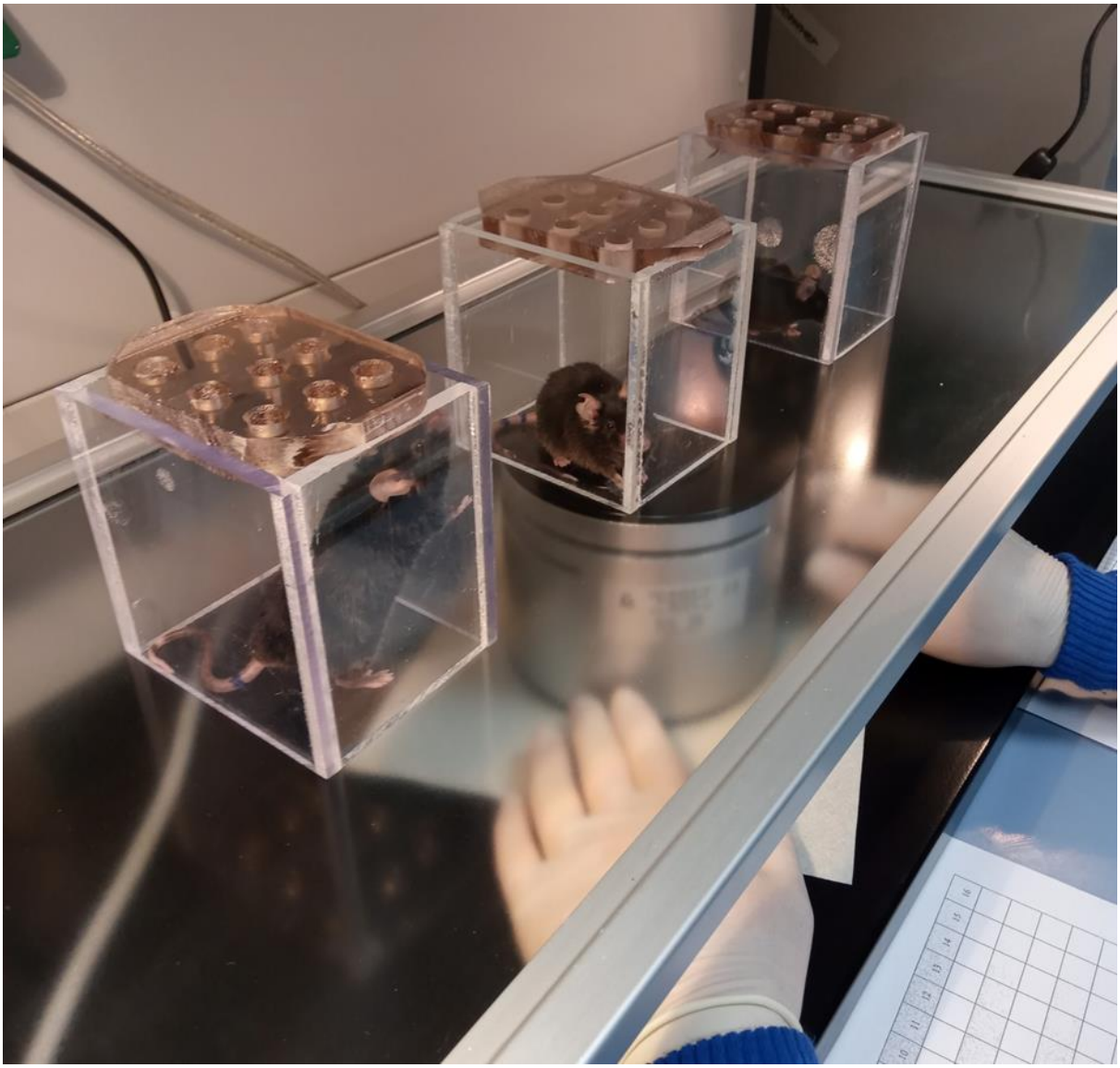

Figure 4: Hargreaves testing setup with mice placed within acrylic glass boxes on a glass plateau.
Representative image of the Hargreaves setup for behavioral testing of heat sensitivities of young and old WT and GLA KO mice placed within acrylic glass boxes on a glass plateau. Mice spent 1h before and during experimental examination within the boxes for adaption and experimental assessment. Abbreviations: GLA KO: alpha-galactosidase A knockout; h: hour; WT: wild type.

4.9.3 Capsaicin administration

Three different capsaicin doses (Sigma-Aldrich, St. Louis, MO, USA) were tested to evaluate the optimal capsaicin dose eliciting nocifensive behavior in GLA KO mice but not in WT mice. 0.2, 1, and 5 µg capsaicin per 10 µl sodium chloride (NaCl) were administered subcutaneously into the right hind paw of young and old WT and GLA KO mice under isoflurane anesthesia. As control, 10 µl NaCl was injected into the right hind paw of young and old WT and GLA KO mice. After the procedure, treated animals were placed into acryl glass boxes on a glass plate and Hargreaves testing was performed after 1h post-capsaicin administration (in the following referred to as "post-capsaicin". Subsequently, animals were tested with the von Frey test. Both tests were repeated after 1d, 2d, and 7d post-capsaicin to screen for the maximal pain behavior at different capsaicin doses (Fig. 5).

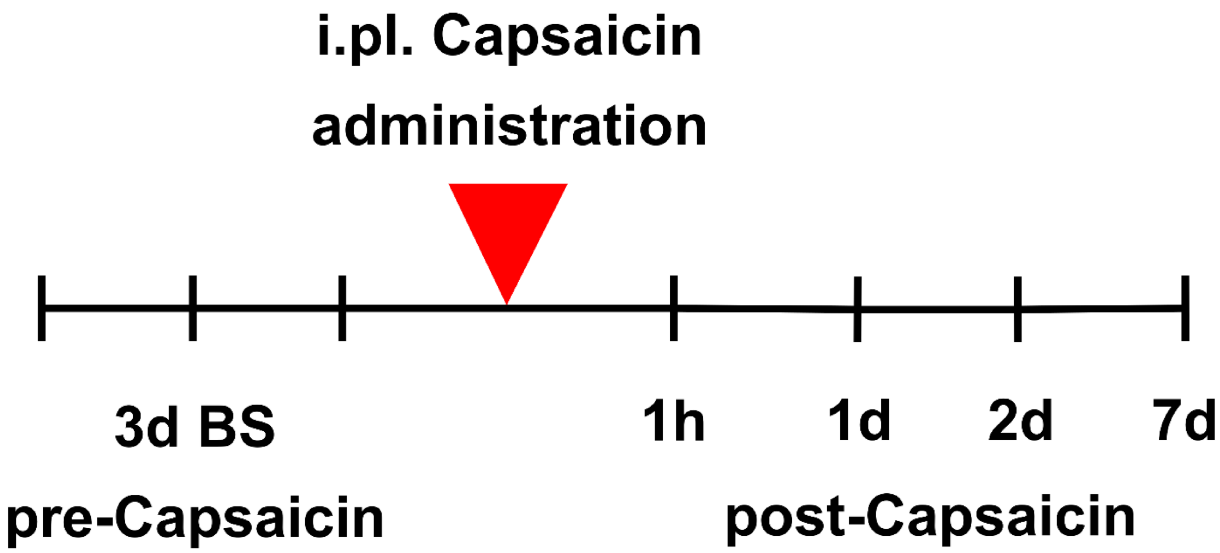

Figure 5: Timeline of von Frey and Hargreaves testing and i.pl. capsaicin administration.
Schematic overview of timepoints for experimental assessment including baseline (BS) behavioral assessment before i.pl. capsaicin administration (pre-Capsaicin) and post-Capsaicin administration at different time points (1h, 1d, 2d, 7d after i.pl. capsaicin administration). Tested animals included young and old WT and GLA KO mice treated with 0.2 µg, 1 µg, and 5 µg capsaicin per 10 µl NaCl i.pl. into the right hindpaw under isoflurane anesthesia. 10 µl NaCl was used in control groups including young and old WT and GLA KO mice. Abbreviations: µg: microgram; µl: microliter; BS: baseline; d: days; h: hour; i.pl.: intraplantar.

4.9.4 Long-term follow up after ERT

To assess long-term effects of repeated ERT administration in WT and GLA KO mice, young WT (2 months) and GLA KO (3 months) mice were treated every other month with 1 mg/kg ERT (agalsidase β, Genzyme, Cambridge, MA, USA) via tail vein injection under isoflurane anesthesia. As control, 1 µl/g NaCl was administered to age-matched WT and GLA KO intravenously. Animals underwent von Frey and Hargreaves testing before ERT administration (pre-ERT) and every third month during regular ERT administration (follow-up). Animals were investigated for up to 1.5 years. Tissue was collected and stored appropriately for further molecular analysis (Fig. 6).

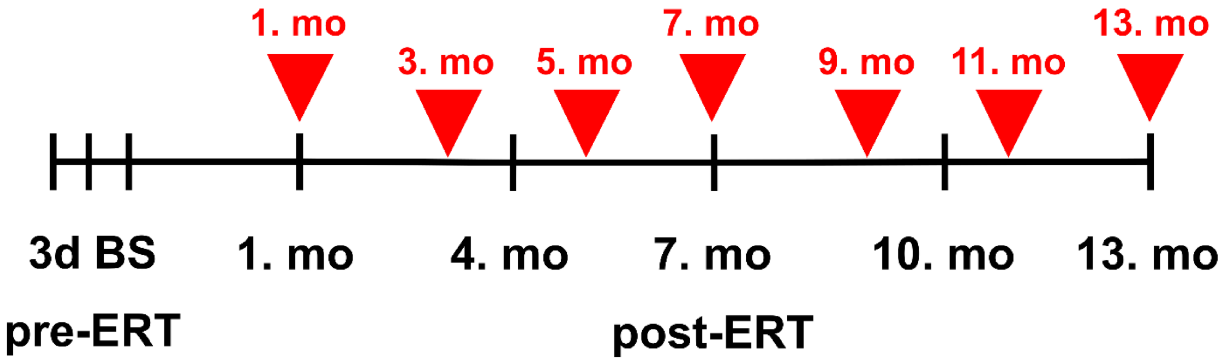

Figure 6: Timeline of von Frey and Hargreaves testing and i.v. ERT administration.
Schematic overview of timepoints for experimental assessment including baseline (BS) behavioral assessment before i.v. ERT administration (pre-ERT) and follow-up behavioral assessment every third month (months in black below the timeline) and long-term i.v. ERT administration every other month (months in red above the timeline and red arrows) (post-ERT). Tested animals included young WT and GLA KO mice treated with 1 µg/g BW ERT i.v. into the tail vein under isoflurane anesthesia. 1 µl/g BW NaCl was used in control groups including young WT and GLA KO mice. Abbreviations: µg: microgram; µl: microliter; BS; baseline; BW: body weight; ERT: enzyme replacement therapy; g: gram; GLA KO: alpha-galactosidase A knockout; i.v.: intravenous; mo: month; WT: wild type.

4.10 Statistical analysis

For statistical analysis, IBM SPSS Statistics 29 was used. Normal distribution was tested with the Kolmogorov-Smirnov and Shapiro-Wilk test. For normally distributed data, Student's t-test for independent two-group comparison and repeated measures analysis of variance (RM ANOVA) with Bonferroni correction for dependent multiple-group comparison was applied. For normally distributed, independent multiple-group comparison, one-way ANOVA with Bonferroni correction was applied, while for non-normally distributed, independent multi-group comparison, Kruskal-Wallis test with Bonferroni correction was used. For non-normally distributed data, Mann-Whitney-U test for independent two-group comparison and Friedman's test with Bonferroni correction for multiple-group comparison was performed. Analyzed data sets are visualized as boxplots depicting the median value with the upper 75% and lower 25% quartile with plotted single data points and whiskers. For M1/M2 ratio analysis, Pearson's correlation analysis was applied due to normally distributed data and visualized as correlation graph with incorporated Pearson's correlation coefficient *r*. Significance was considered at a *p* value of <0.05.

5. Results

5.1 Gb3 accumulations in DRG of young and old GLA KO mice

The load of Gb3 accumulation within DRG cryosections of young and old GLA KO and WT mice was assessed via fluorescent intensity signal of STxB binding (Fig. 7A-D). WT DRG had hardly any STxB fluorescence. In DRG of young GLA KO, we found higher StxB intensities compared to young WT mice ($p<0.05$, Fig. 7E). The same result was found in DRG of old GLA KO mice compared to WT mice ($p<0.01$, Fig. 7E). No StxB signal intensity difference was visible between DRG of young and old GLA KO mice (Fig. 7F).

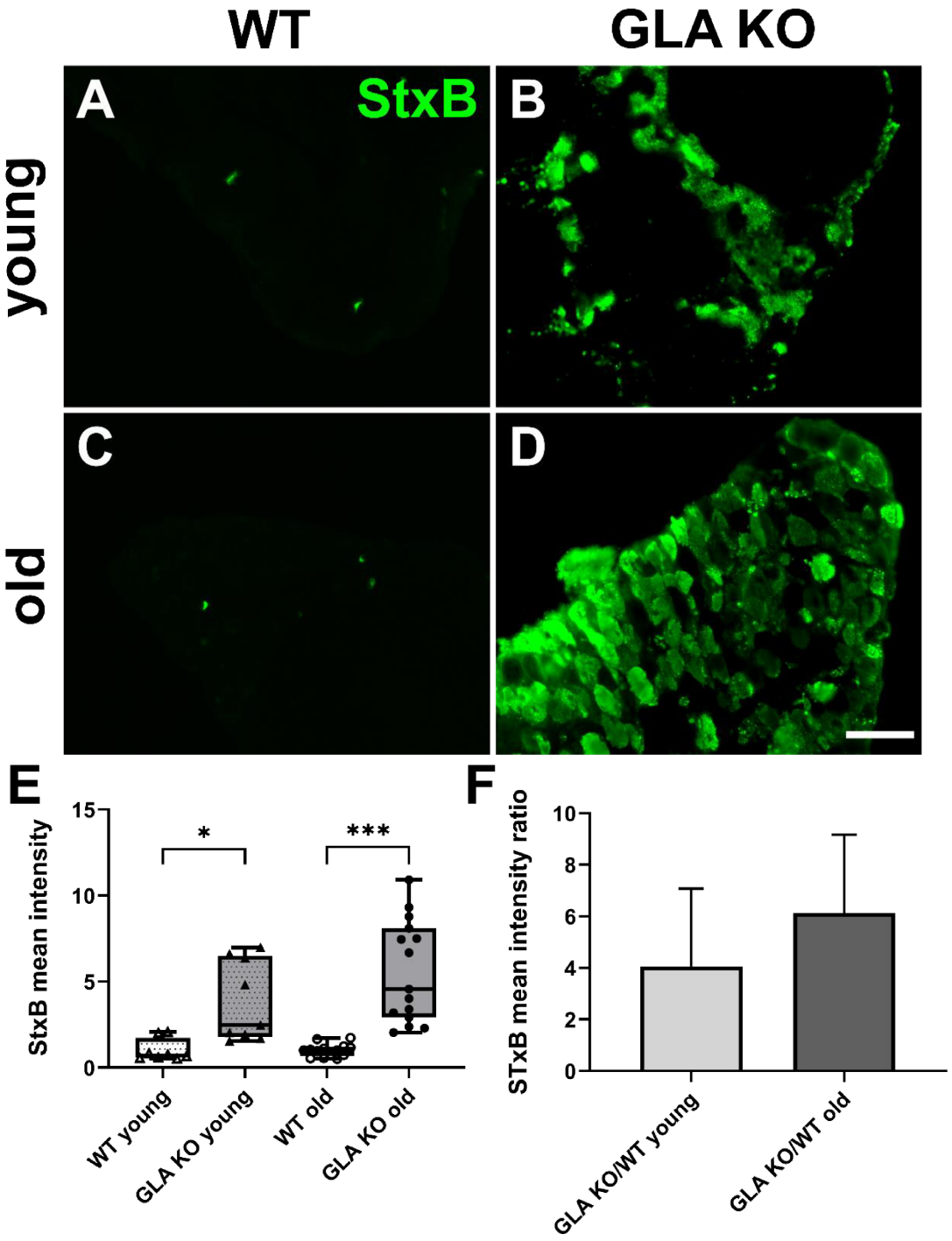

Figure 7: Gb3 accumulation in DRG of young and old WT and GLA KO mice.
(A-D) Representative photomicrographs of Gb3 load in DRG cryosections of young and old WT and GLA KO mice stained with fluorophore-coupled STxB. (E) StxB intensity measurements in DRG cryosections of young and old WT and GLA KO mice for indirect Gb3 load assessment via STxB mean intensities. (F) StxB mean intensity GLA KO-to-WT ratios of young and old mice. Abbreviations: DRG: dorsal root ganglion; Gb3: globotriaosylceramide; GLA KO: alpha-galactosidase A knockout; STxB: Shiga toxin subunit B; WT: wild type. *p<0.05; ***p<0.001. Scale bar: 100 µm. Adjusted from (Spitzel et al., 2022).

5.2 Dysregulation of DRG immune responses in GLA KO mice

5.2.1 Downregulation of inflammation-associated target genes in DRG of old GLA KO mice compared to old WT mice

To screen for dysregulated target genes, we performed a qRT PCR array analysis with a set of preloaded inflammation-associated gene assays on DRG tissue from old WT and GLA KO mice. We chose potentially dysregulated genes based on fold changes (up-regulated genes >0.5, down-regulated genes <0.5) and Ct values (<30) (Fig. 8A), which were validated by qRT PCR analysis. This revealed downregulation in DRG of GLA KO mice compared to WT mice of the following four target genes: glial fibrillary acidic protein (*GFAP)*, interleukin-1beta (*IL-1β)*, interleukin 10 (*IL10)*, and leucine-rich alpha-2-glycoprotein 1 (*LRG1*) (p<0.05, Fig. 8B-E).

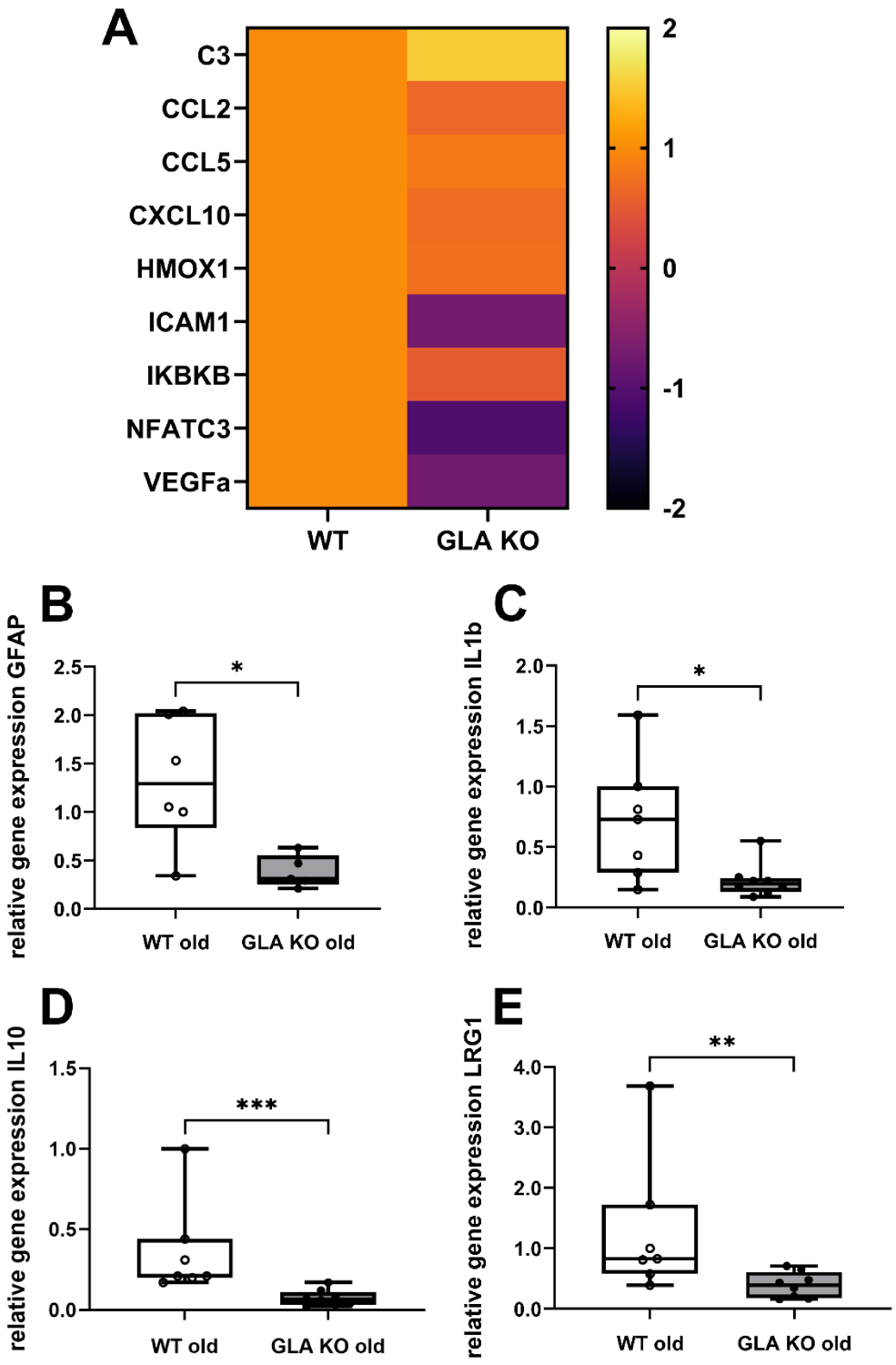

Figure 8: Gene expression analysis of inflammation-associated targets in whole DRG of old WT and GLA KO mice.
(A) Target gene screening via gene expression array analysis of inflammation-associated target genes using pooled DRG material of seven old WT and DRG mice each. Single duplex qRT PCR of selected inflammation-associated target genes including *GFAP* (B), *IL1b* (C), *IL10* (D), and *LRG1* (E) using whole DRG of old WT and GLA KO mice. Abbreviations: C3: complement 3; CCL2/5: C-C motif chemokine 2/5; CXCL10: C-X-C motif chemokine ligand 10; DRG: dorsal root ganglion; GFAP: glial fibrillary acidic protein; GLA KO: alpha galactosidase A knockout; HMOX1: heme oxygenase 1; ICAM1: intercellular adhesion molecule 1; IKBKB: inhibitor of nuclear factor kappa-B kinase subunit beta; IL1b/10: interleukin 1b/10; LRG1: leucine-rich alpha-2-glycoprotein 1; NFATC3: nuclear factor of activated T-cells, cytoplasmic 3; VEGFα: vascular endothelial growth factor alpha; WT: wild type. *p<0.05; **p<0.01; ***p<0.001. Adjusted from (Spitzel et al., 2022).

5.2.2 Similar numbers of CD3⁺ T-cells and CD11b⁺ M0 macrophages in DRG of old GLA KO mice and old WT mice

Based on gene expression dysregulation in DRG of old GLA KO mice, we investigated infiltration rates of immune cells including CD3⁺ T-cells and CD11b⁺ M0 macrophages (Fig. 9A-D). Investigation of DRG of old WT and GLA KO mice revealed no differences in immune cell count between the two genotypes for CD3 and CD11b (Fig. 9E,F).

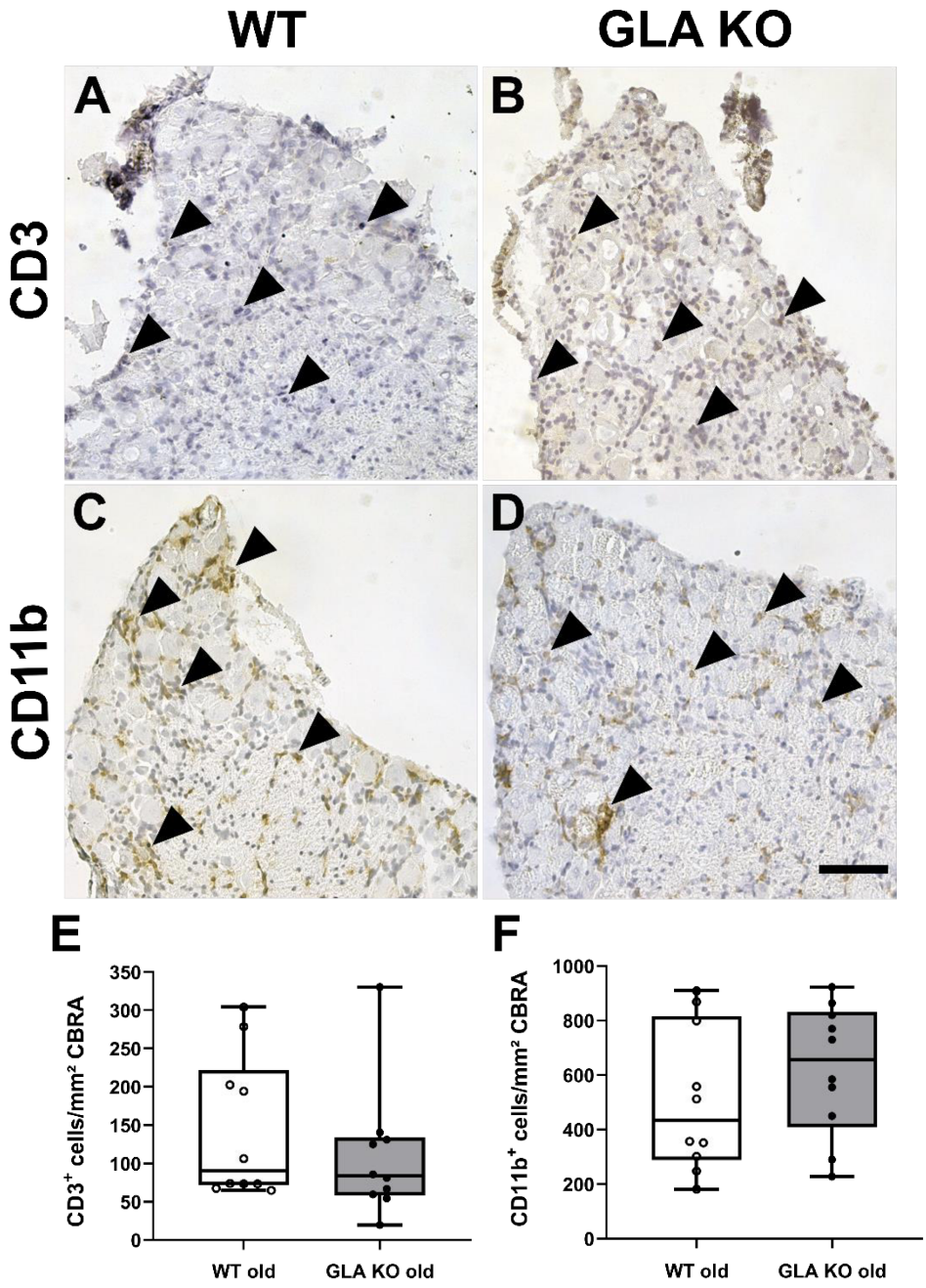

Figure 9: Immune cell quantification in DRG of old WT and GLA KO mice.
(A-D) Representative photomicrographs of DRG cryosections of old WT and GLA KO mice stained against CD3⁺ T-cells (A,B) and CD11b⁺ pan-macrophages (C,D) (full black arrow heads). (E) Quantification of CD3⁺ T-cells/mm² CBRA in DRG of old WT and GLA KO mice. (F) Quantification of CD11b⁺ pan-macrophages/mm² CBRA in DRG of old WT and GLA KO mice. Abbreviations: CBRA: cell body-rich area; CD3/11b: cluster of differentiation 3/11b; DRG: dorsal root ganglion; GLA KO: alpha-galactosidase A knockout; mm²: square millimeter; WT: wild type. Scale bar: 100 µm. Adjusted from (Spitzel et al., 2022).

5.2.3 Equal numbers of F4/80$^+$ M0 and CD80$^+$ M1 pro-inflammatory macrophages in DRG of old GLA KO mice compared to old WT mice

Analysis of additional M0 and M1 pro-inflammatory macrophage-specific markers F4/80 and CD80, respectively, showed no differences in cell count numbers in DRG of old GLA KO mice compared to old WT mice (Fig. 10).

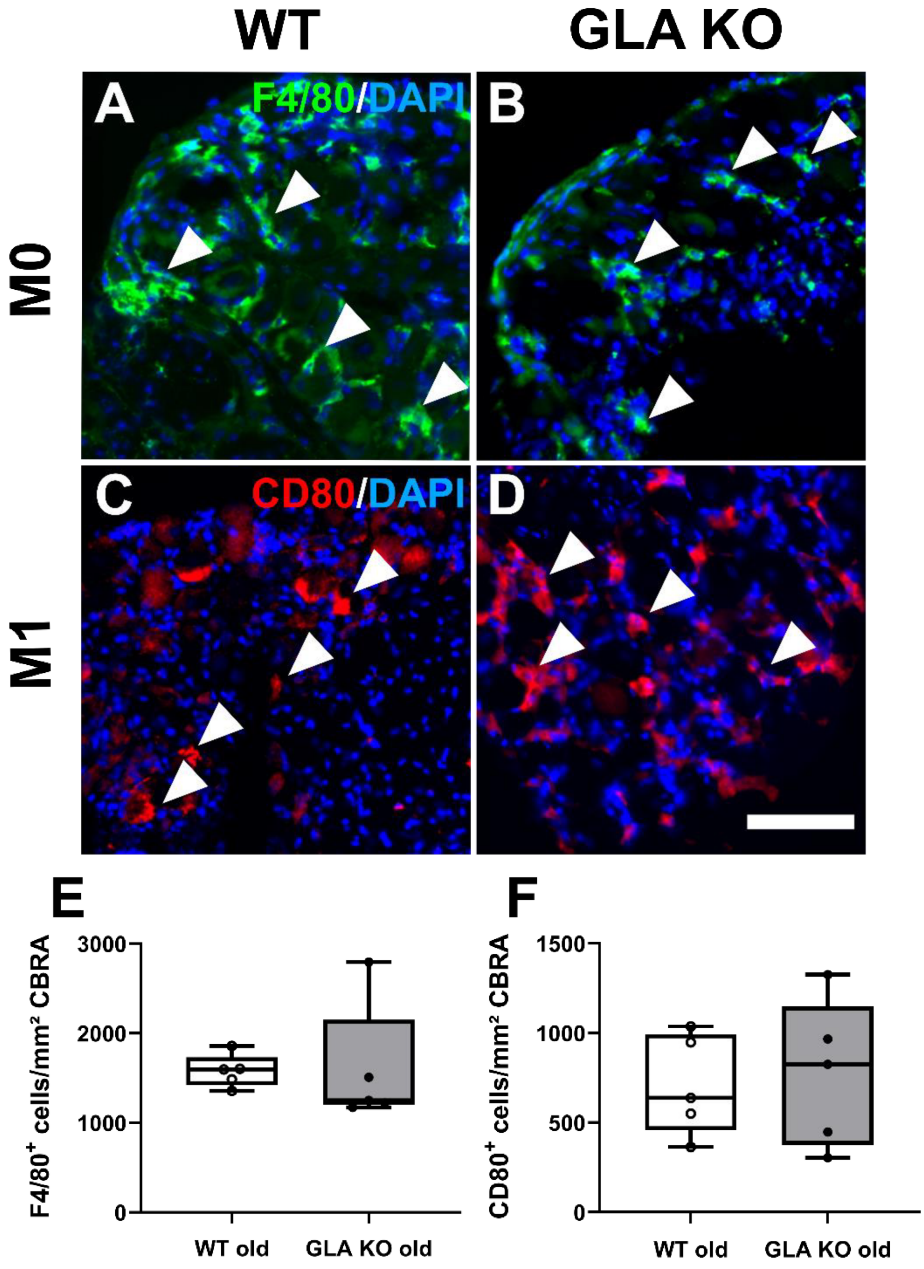

Figure 10: M0 and M1 macrophage subtype quantification in DRG of old WT and GLA KO mice.
(A-D) Representative photomicrographs of DRG cryosections of old WT and GLA KO mice stained against F4/80$^+$ M0 pan-macrophages (A,B) and CD80$^+$ M1 pro-inflammatory macrophages (C,D) (full white arrow heads). (E) Quantification of F4/80+ M0 pan-macrophages/mm² CBRA in DRG of old WT and GLA KO mice. (F) Quantification of CD80$^+$ M1 pro-inflammatory macrophages/mm² CBRA in old WT and GLA KO mice. Abbreviations: CBRA: cell body-rich area; CD80: cluster of differentiation 80; DRG: dorsal root ganglion; F4/80: pan-macrophages-specific marker; GLA KO: alpha-galactosidase A knockout; M0: pan-macrophages; M1: pro-inflammatory macrophages; mm²: square millimeter; WT: wild type. Scale bar: 25 µm. Adjusted from (Spitzel et al., 2022).

5.2.4 Lower numbers of CD206$^+$ anti-inflammatory macrophages in DRG of old GLA KO mice compared to old WT mice

Complementary to M1 pro-inflammatory macrophages we investigated the number of CD206$^+$ M2 anti-inflammatory macrophages in DRG of old GLA KO mice compared to old WT mice (Fig. 11A,B) and found lower numbers of CD206$^+$ macrophages in DRG of old GLA KO mice compared to old TW mice (p<0.01, Fig. 11C).

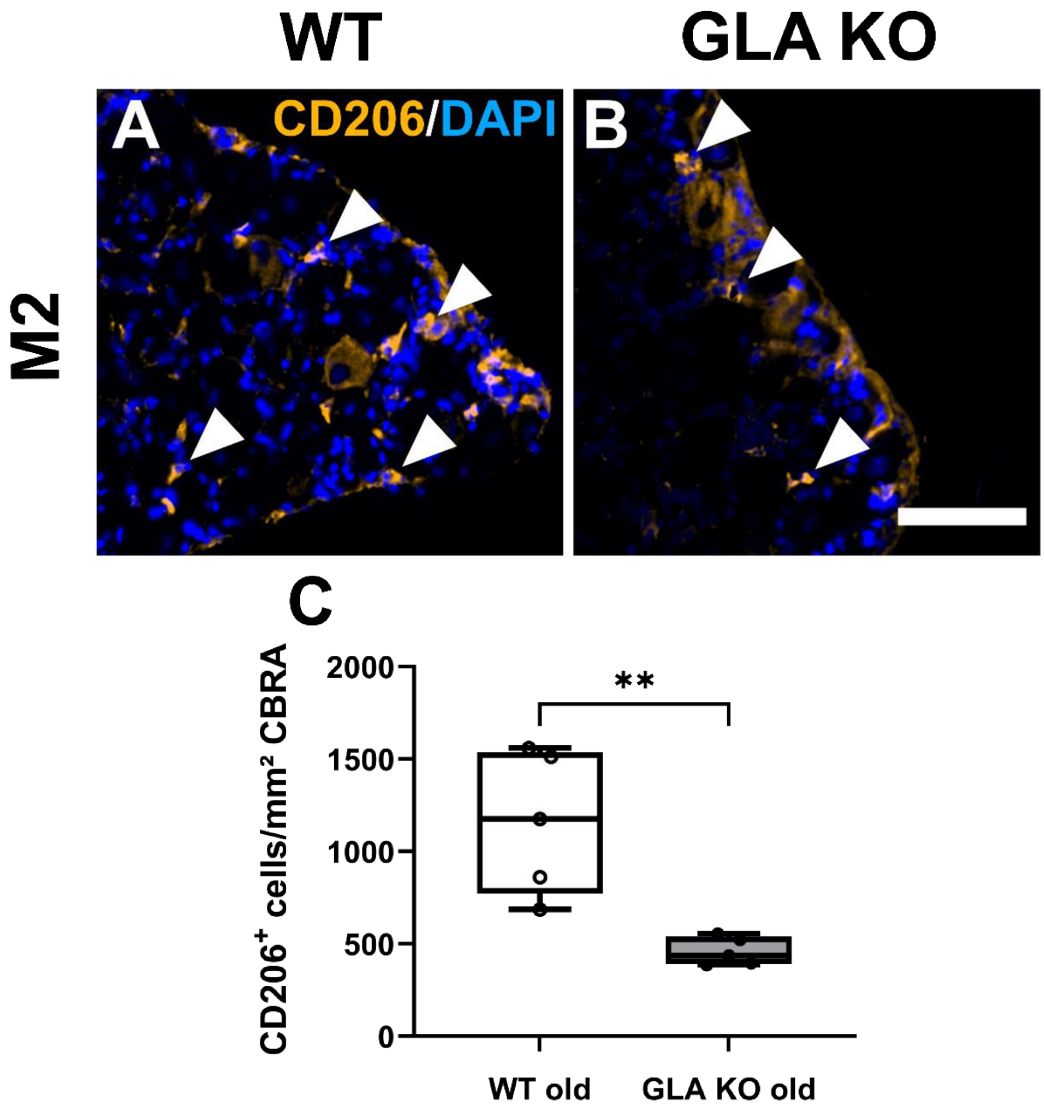

Figure 11: M2 macrophage subtype quantification in DRG of old WT and GLA KO mice.
(A,B) Representative photomicrographs of DRG cryosections of old WT and GLA KO mice stained against CD206$^+$ M2 anti-inflammatory macrophages (full white arrow heads). (C) Quantification of CD206$^+$ M2 anti-inflammatory macrophages/mm² CBRA in DRG of old WT and GLA KO mice. Abbreviations: CBRA: cell body-rich area; CD206: cluster of differentiation 206; DRG: dorsal root ganglion; GLA KO: alpha-galactosidase A knockout; M2: anti-inflammatory macrophages; mm²: square millimeter; WT: wild type. **p<0.01. Scale bar: 25 µm.
Adjusted from (Spitzel et al., 2022).

5.2.5 No bidirectional polarization into M1 and M2 macrophage subtypes in DRG of old GLA KO mice

We further analyzed the protein expression ratio of M1 to M2 macrophages in DRG of old WT mice and old GLA KO mice. In both groups we found no bidirectional regulation between M1 and M2 macrophage numbers in DRG tissue (Fig. 12).

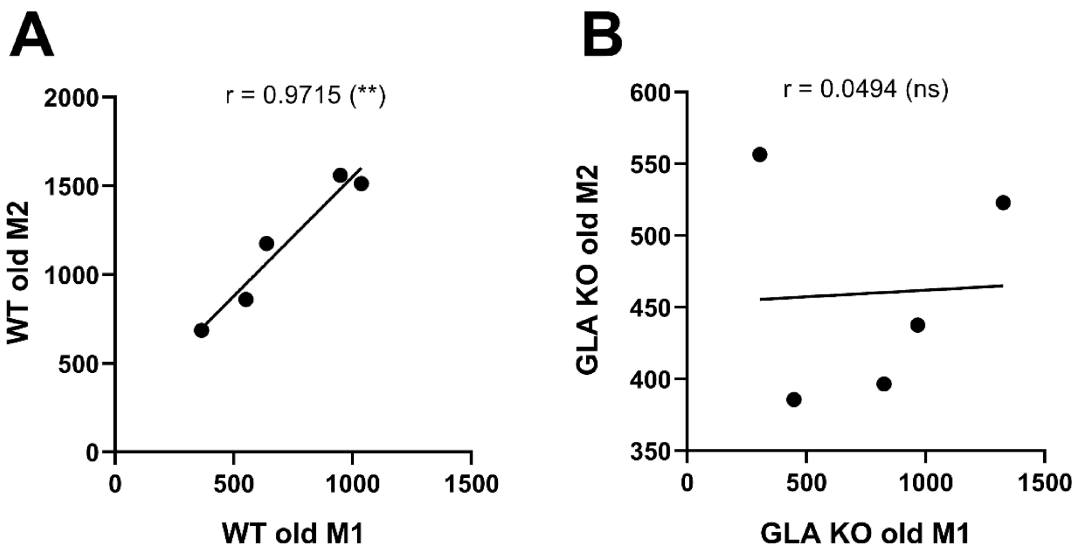

Figure 12: M1-to-M2 macrophage subtype ratio analysis in DRG of WT and GLA KO mice.
(A) Correlation analysis of M1-to-M2-ratio in DRG of old WT mice. (B) Correlation analysis of M1-to-M2-ratio in DRG of old GLA KO mice. Abbreviations: DRG: dorsal root ganglion; GLA KO: alpha-galactosidase A knockout; M1: pro-inflammatory macrophages; M2: anti-inflammatory macrophages; r: Pearson's coefficient; WT: wild type. $^{**}p<0.01$. Adjusted from (Spitzel et al., 2022).

5.3 Hypoxic environment in the DRG of GLA KO mice

5.3.1 Upregulation of hypoxia-associated target genes in DRG of old GLA KO mice compared to old WT mice

We performed a multitarget array and screened for a selection of dysregulated target genes based on fold change values (up-regulated genes >1.5, down-regulated genes < -1.5) and suitable Ct values (<30) (Fig.13A). A selection of dysregulated target genes was validated via single qRT PCR analysis using DRG tissue of old WT and GLA KO mice. DNA damage inducible factor 4 (*DDIT4*), proto-oncogene cFOS (*FOS*), hexokinase 2 (*HK2*), galectin 3 (*LGALS3*), and transferrin receptor 1 (*TFRC*) were upregulated in DRG of old GLA KO mice compared to old WT mouse DRG ($p<0.05$, Fig. 13B-F).

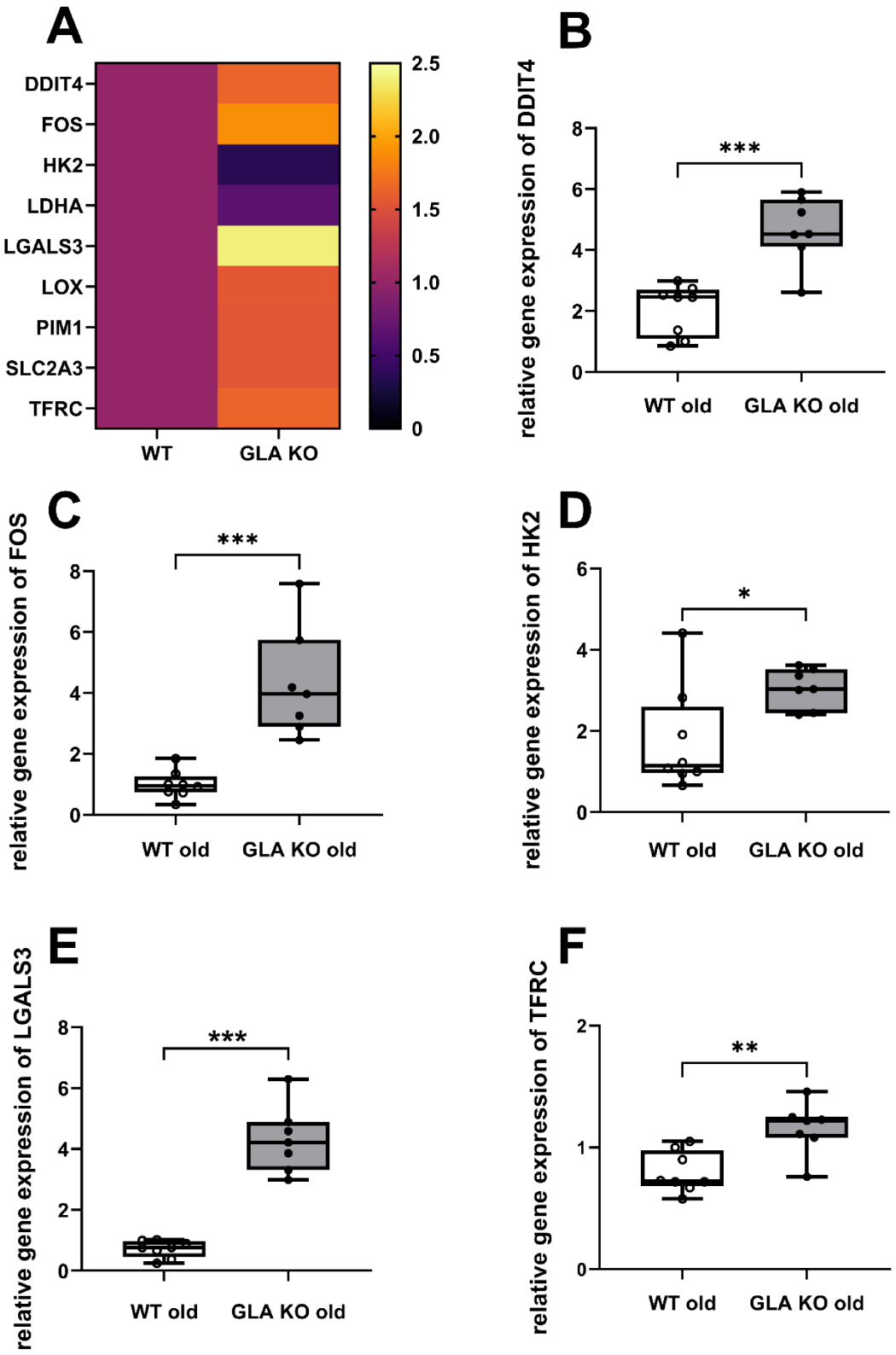

Figure 13: Gene expression analysis of hypoxia-associated targets in whole DRG of old WT and GLA KO mice.

(A) Target gene screening via gene expression array analysis of hypoxia-associated target genes using pooled DRG material of seven old WT and DRG mice each. Single duplex qRT PCR of selected hypoxia-associated target genes including *DDIT4* (B), *FOS* (C), *HK2* (D), *LGALS3* (E), and *TFRC* (F) using whole DRG of old WT and GLA KO mice. Abbreviations: DDIT4: DNA-damage-inducible transcript 4; DRG: dorsal root ganglion; FOS: proto-oncogene cFOS; GLA KO: alpha-galactosidase A knockout; HK2: hexokinase 2; LDHA: lactate dehydrogenase; LGALS3: galectin 3; LOX: lysyl oxidase; PIM1: proto-oncogene Pim1; SLC2A3: solute carrier family 2 member 3; TFRC: transferrin receptor; WT: wild type. *p<0.05; **p<0.01; ***p<0.001.

5.3.2 Lower numbers of HIF1α⁺ neurons with cytosolic distributed signal in DRG of young and old GLA KO mice compared to age-matched WT mice

Complementary to the gene expression data, we assessed the protein distribution of the cellular hypoxia sensor hypoxia-inducible factor 1 alpha (HIF1α) (Fig. 14A-D). Analysis of HIF1α⁺ DRG neurons with cytosolic protein distribution revealed a lower number of HIF1α⁺ DRG neurons in young and old GLA KO mice compared to respective age-matched WT mice (p<0.01, Fig. 14E,F).

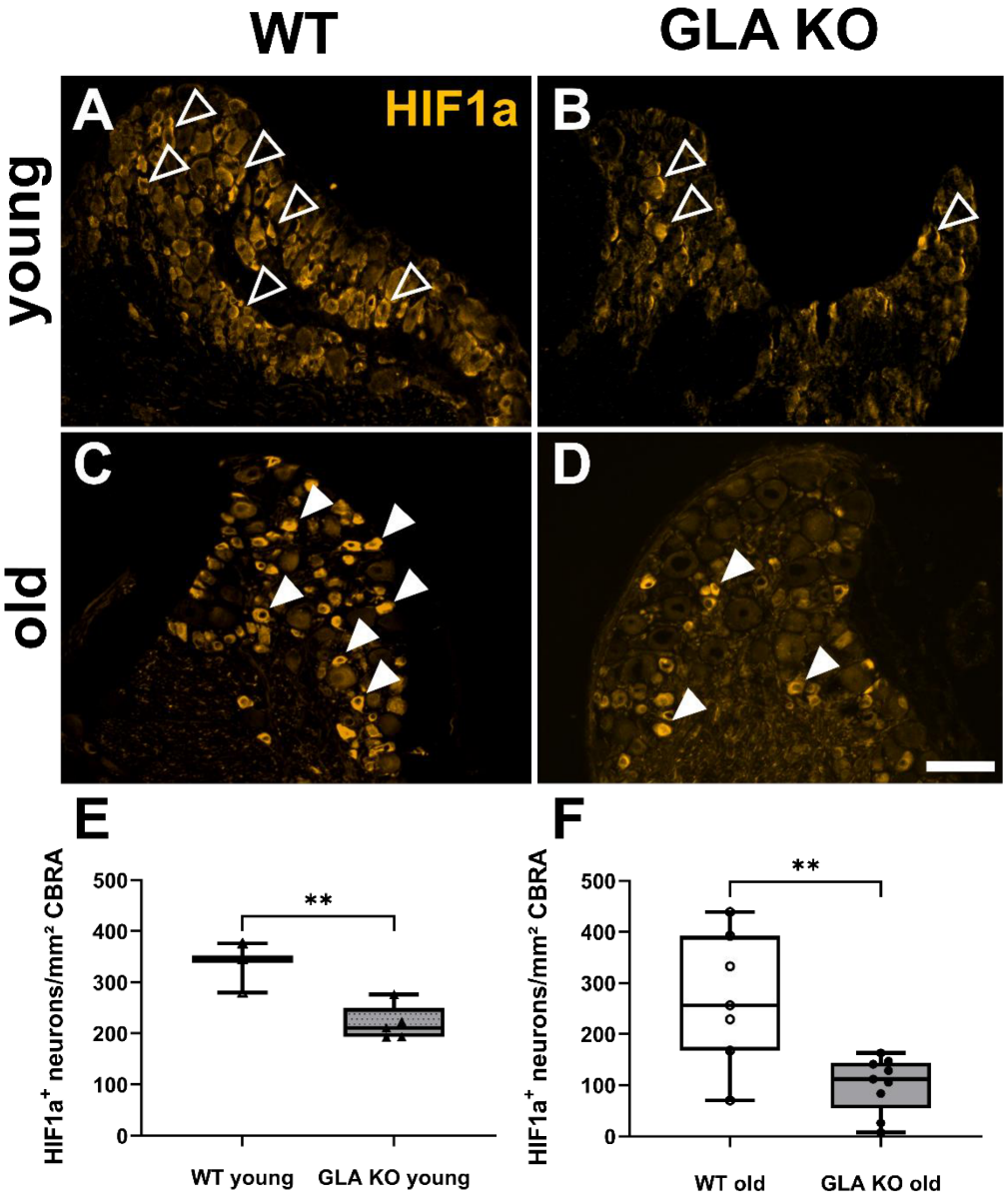

Figure 14: HIF1α⁺ neuron quantification in DRG of young and old WT and GLA KO mice.
(A-D) Representative photomicrographs of DRG cryosections of young (empty white arrow heads) and old (full white arrow heads) WT and GLA KO mice stained against HIF1α⁺ DRG neurons. (E) Quantification of HIF1α⁺ neurons/mm² CBRA in DRG of young WT and GLA KO mice. (F) Quantification of HIF1α+ neurons/mm² CBRA in old WT and GLA KO mice. Abbreviations: CBRA: cell body-rich area; DRG: dorsal root ganglion; GLA KO: alpha-galactosidase A knockout; HIF1α: hypoxia-inducible factor 1 alpha; mm²: square millimeter; WT: wild type. **p<0.01. Scale bar: 100 µm.

5.3.3 HIF1α cyto-nuclear translocation in DRG neurons of old GLA KO mice

To analyze the cyto-nuclear translocation of HIF1α as transcription factor, we performed intensity measurements of HIF1α signal within the nucleus of DRG neurons from WT and GLA KO mice (Fig. 15A,B). Nuclear HIF1α signal did not differ between young groups, while nuclear HIF1α signal was higher in DRG neurons of old GLA KO mice compared to old WT mice (p<0.01, Fig. 15C,D).

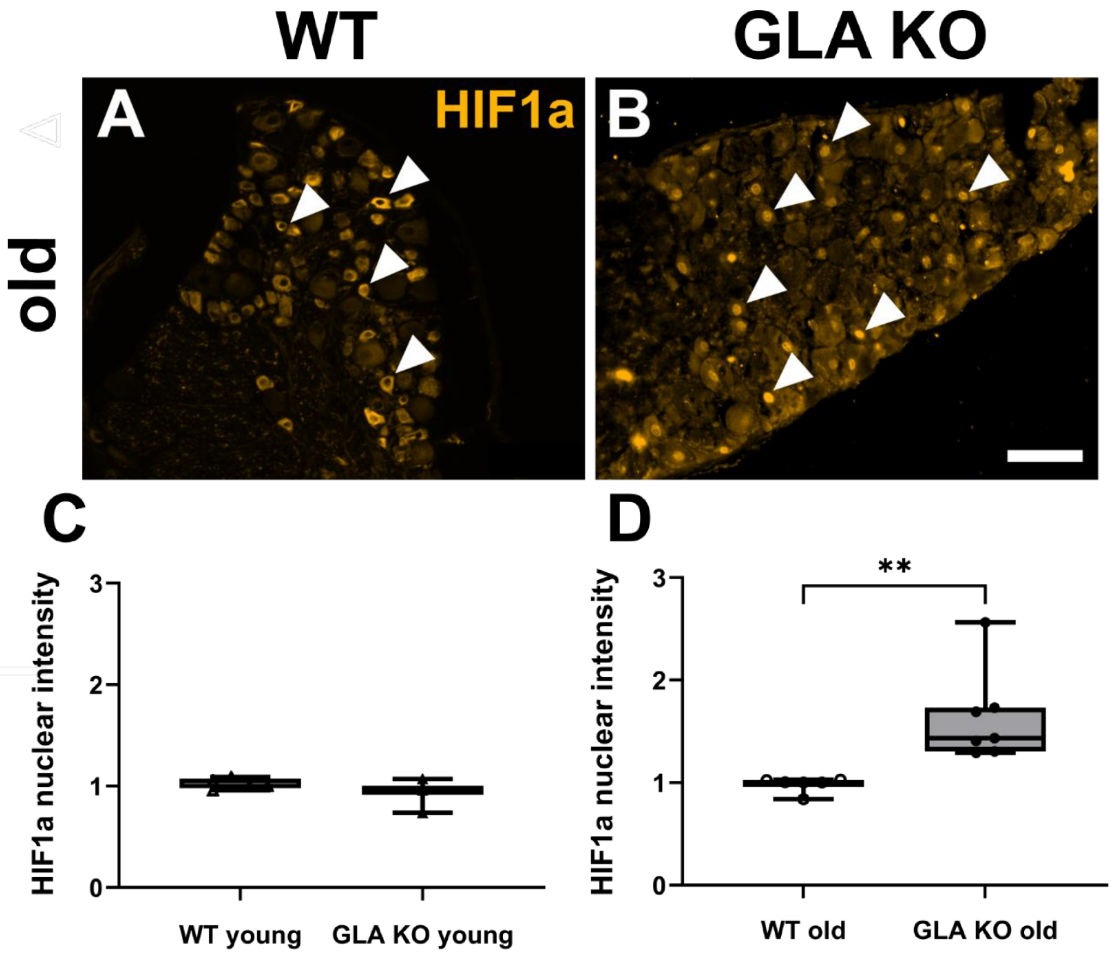

Figure 15: HIF1α nuclear intensity measurements in DRG neurons of young and old WT and GLA KO mice. (A,B) Representative photomicrographs of DRG cryosections of old WT and GLA KO mice stained against HIF1α in DRG neurons of WT (full white arrow heads, cytosolic HIF1α distribution) and GLA KO (full white arrow heads, nuclear HIF1α distribution) mice. (C) Measurement of nuclear HIF1α mean intensity in DRG of young WT and GLA KO mice. (D) Measurement of nuclear HIF1α mean intensity in old WT and GLA KO mice. Abbreviations: DRG: dorsal root ganglion; GLA KO: alpha-galactosidase A knockout; HIF1α: hypoxia-inducible factor 1 alpha; WT: wild type. **p<0.01. Scale bar: 100 µm.

5.3.4 Higher numbers of CA9⁺ neurons in DRG of old GLA KO mice compared to old WT mice

CA9 protein expression as HIF1α downstream target was assessed in murine DRG neurons (Fig. 16A,B). We found no differences in young groups, but higher numbers of CA9⁺ DRG neurons in old GLA KO mice compared to old WT mice (p<0.01, Fig. 16C,D).

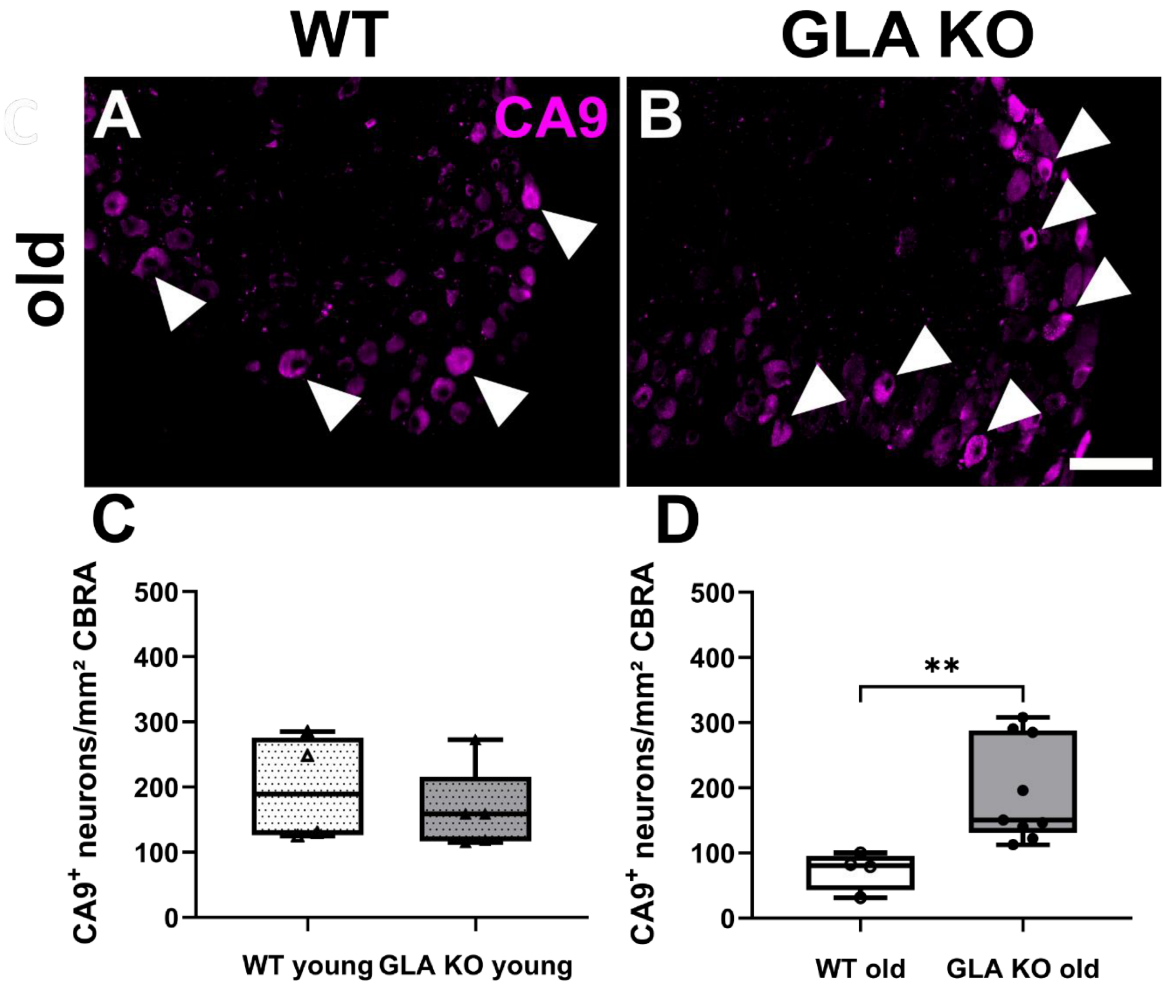

Figure 16: CA9⁺ neuron quantification in DRG of young and old WT and GLA KO mice.
(A,B) Representative photomicrographs of DRG cryosections of old (full white arrow heads) WT and GLA KO mice stained against CA9⁺ DRG neurons. (C) Quantification of CA9⁺ neurons/mm² CBRA in DRG of young WT and GLA KO mice. (D) Quantification of CA9⁺ neurons/mm² CBRA in old WT and GLA KO mice. Abbreviations: CA9: carbonic anhydrase 9; CBRA: cell body-rich area; DRG: dorsal root ganglion; GLA KO: alpha-galactosidase A knockout; mm²: square millimeter; WT: wild type. **p<0.01. Scale bar: 100 µm.

5.3.5 Upregulation of hypoxia-associated target genes in DRG neuronal cell cultures under hypoxic conditions

Gene expression of six hypoxia-associated targets was assessed in DRG neuronal cell cultures of old WT and GLA KO mice under normoxic and hypoxic conditions. *DDIT4*, *HK2*, and *LDHA* were upregulated in DRG neurons of WT and GLA KO mice only under hypoxic conditions compared to the same neuronal cell cultures under normoxic conditions ($p<0.01$, Fig. 17A-C). *LGALS3* was upregulated in GLA KO DRG neuronal cell cultures under normoxia and hypoxia compared to WT DRG neuronal cell cultures cultivated under normoxia and hypoxia, respectively. Upregulated *LGALS3* gene expression in GLA KO DRG neurons compared to WT DRG neurons intensified under hypoxic conditions in both genotypes ($p<0.01$, Fig. 17D). *TFRC* was only upregulated in WT DRG neuronal cell culture cultivated under hypoxic conditions compared to normoxic conditions ($p<0.05$, Fig. 17E).

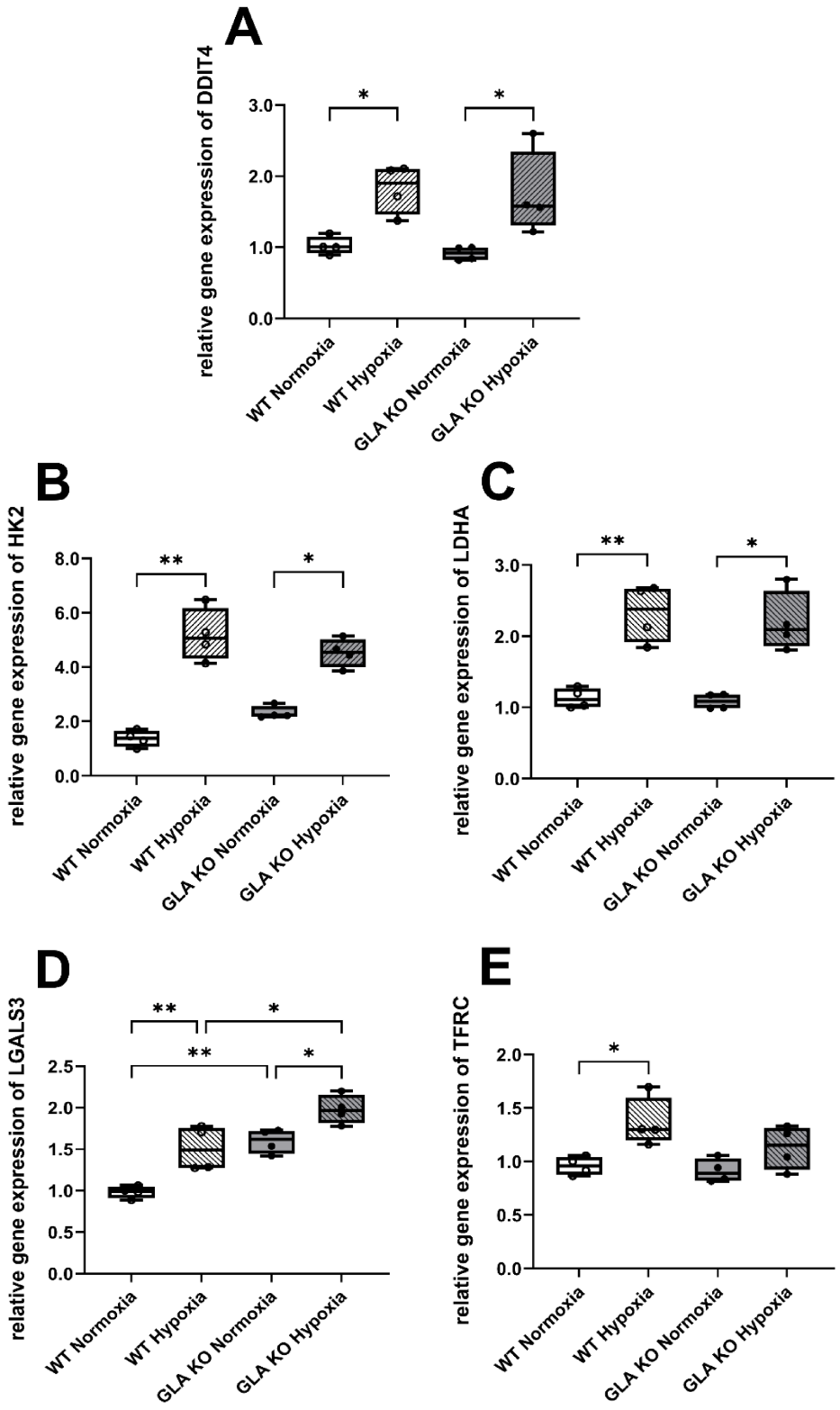

Figure 17: Gene expression analysis of hypoxia-associated targets in DRG neuronal cell cultures of old WT and GLA KO mice after 24h cultivation under normoxic (21% O_2) and hypoxic (2% O_2) conditions.
(A-E) Single duplex qRT PCR of selected hypoxia-associated target genes including *DDIT4* (A), *HK2* (B), *LDHA* (C), *LGALS3* (D), and *TFRC* (E) using DRG neuronal cell cultures cultivated under normoxic and hypoxic conditions of old WT and GLA KO mice. Abbreviations: DDIT4: DNA-damage-inducible transcript 4; DRG: dorsal root ganglion; GLA KO: alpha-galactosidase A knockout; HK2: hexokinase 2; LDHA: lactate dehydrogenase; LGALS3: galectin 3; TFRC: transferrin receptor; WT: wild type. *p<0.05; **p<0.01.

5.3.6 Equal distribution of HIF1α protein in the cytosol and nucleus of DRG neuronal cell cultures under normoxia and hypoxia irrespective of the genotype

Based on upregulated gene expression of hypoxia-associated targets, HIF1α protein distribution was assessed in DRG neuronal cell cultures of old WT and GLA KO mice cultivated under normoxia and hypoxia (Fig. 18A-D). Analysis of HIF1α$^+$ DRG neurons (Fig. 18E) and HIF1α nuclear intensities (Fig. 18F) did not differ between genotypes cultivated under normoxia and hypoxia.

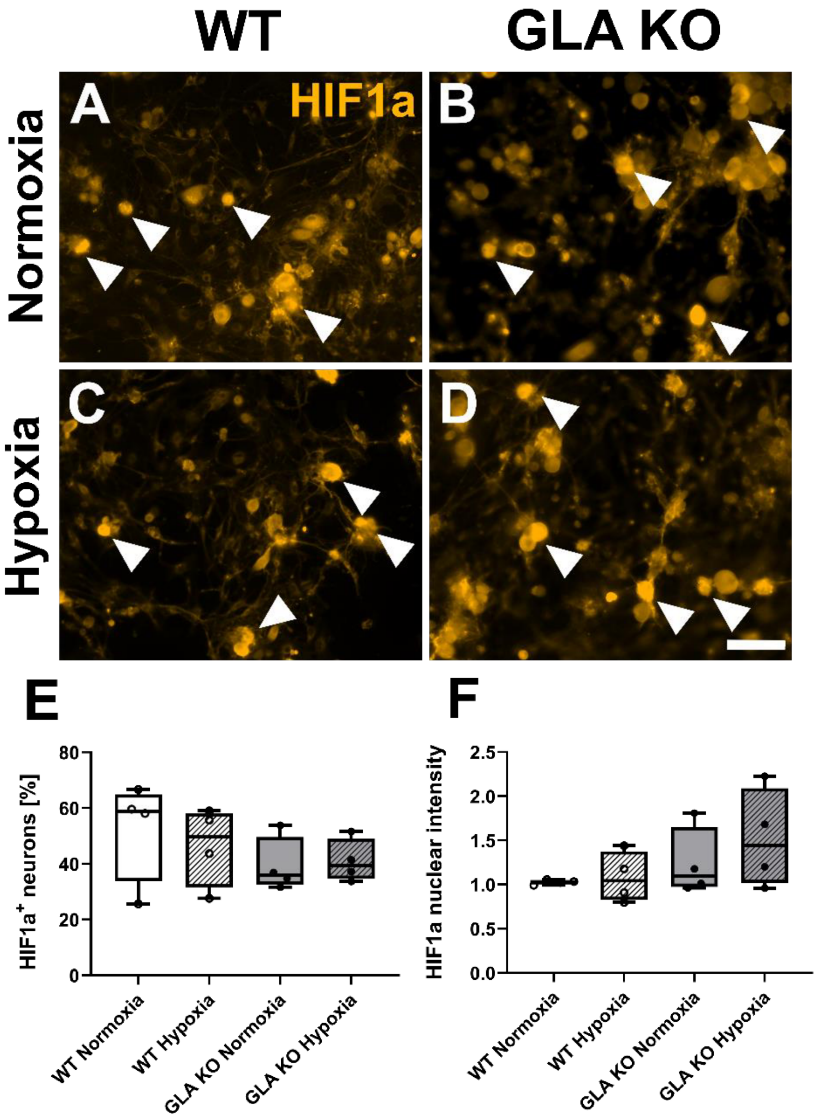

Figure 18: HIF1α protein distribution in DRG neuronal cell cultures of old WT and GLA KO mice after 24h cultivation under normoxic (21% O_2) and hypoxic (2% O_2) conditions.
(A-D) Representative photomicrographs of DRG neuronal cell cultures of old WT and GLA KO mice after 24h cultivation under normoxic (21% O_2) and hypoxic (2% O_2) conditions stained against HIF1α$^+$ DRG neurons (full white arrow heads). (E) Quantification of HIF1α$^+$ neurons in DRG neuronal cell cultures of old WT and GLA KO mice under normoxic and hypoxic conditions. (F) Measurement of HIF1α nuclear mean intensities in DRG neuronal cell cultures of old WT and GLA KO mice under normoxic and hypoxic conditions. Abbreviations: DRG: dorsal root ganglion; GLA KO: alpha-galactosidase A knockout; HIF1α: hypoxia-inducible factor 1 alpha; WT: wild type. Scale bar: 100 µm.

5.3.7 Equal distribution of CA9 protein in DRG neuronal cell cultures under normoxia and hypoxia irrespective of the genotype

Further assessment of $CA9^+$ DRG neurons of old WT and GLA KO mice cultivated under normoxic and hypoxic conditions (Fig. 19A-D) did not reveal differences in CA9 protein expression (Fig. 19E).

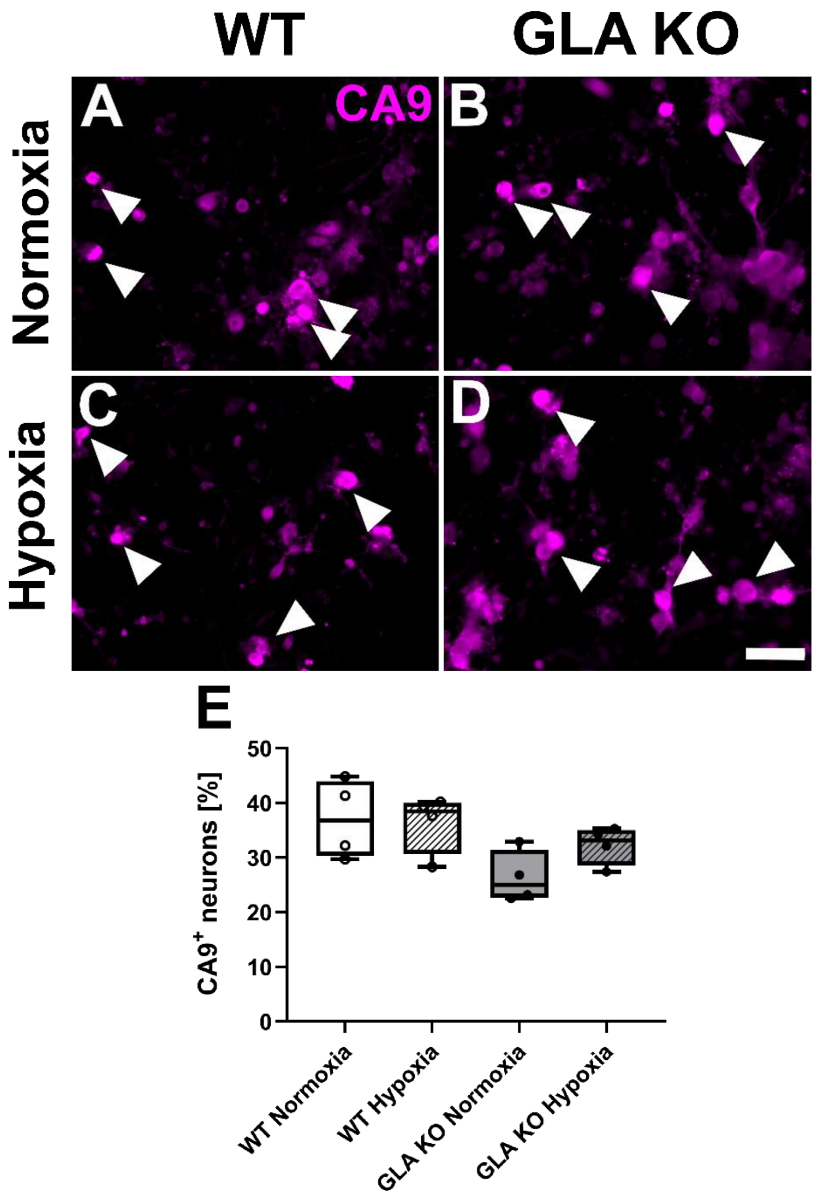

Figure 19: CA9 protein distribution in DRG neuronal cell cultures of old WT and GLA KO mice after 24h cultivation under normoxic (21% O_2) and hypoxic (2% O_2) conditions.
(A-D) Representative photomicrographs of DRG neuronal cell cultures of old WT and GLA KO mice after 24h cultivation under normoxic (21% O_2) and hypoxic (2% O_2) conditions stained against $CA9^+$ DRG neurons (full white arrow heads). (E) Quantification of CA9+ neurons in DRG neuronal cell cultures of old WT and GLA KO mice under normoxic and hypoxic conditions. Abbreviations: CA9: carbonic anhydrase 9; DRG: dorsal root ganglion; GLA KO: alpha-galactosidase A knockout; WT: wild type. Scale bar: 100 µm.

5.4 Reduced vascularization of DRG of GLA KO mice compared to WT mice

Next, we performed analysis of vascularization characteristics of DRG of old WT and GLA KO mice (Fig. 20A-D). We found a bigger cross sectional DRG area in old GLA KO mice compared to young GLA KO mice ($p<0.05$) and old WT mice ($p<0.05$, Fig. 20E). Analysis of vascular characteristics revealed reduced DRG vascularization ($p<0.05$, Fig. 20F), and lower numbers of blood vessel branches in DRG of old GLA KO mice compared to old WT mice ($p<0.05$, Fig. 20G). Total blood vessel length was reduced in DRG of old GLA KO mice compared to young GLA KO mice ($p<0.01$) and old WT mice ($p<0.001$, Fig. 20H). Average blood vessel thickness did not differ between genotypes and age groups (Fig. 20I).

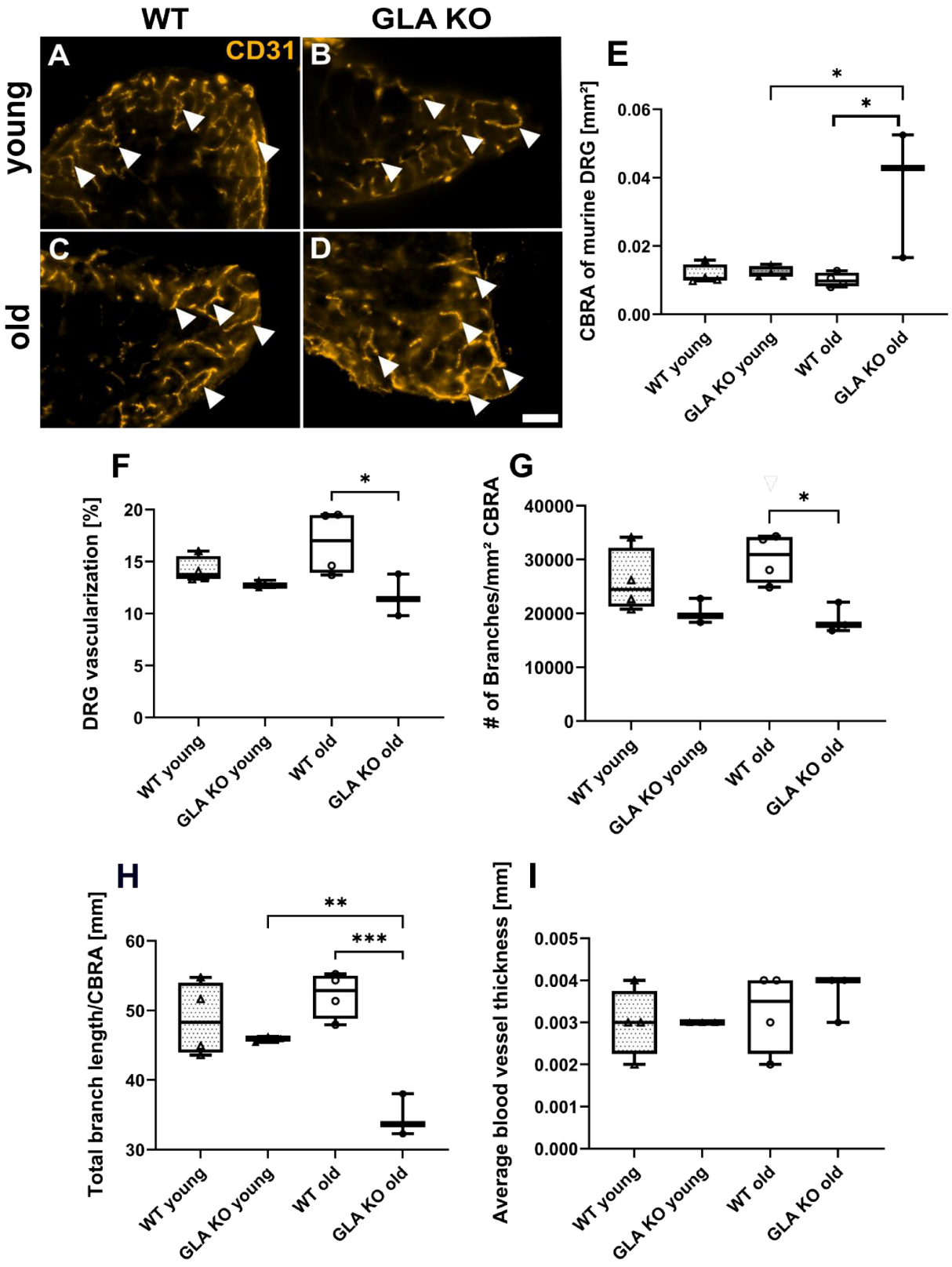

Figure 20: CD31⁺ blood vessel characteristics analysis in DRG of young and old WT and GLA KO mice. (A-D) Representative photomicrographs of CD31⁺ blood vessels in DRG of young and old WT and GLA KO mice (full arrow heads). (E) Measurement of CBRA in DRG cryosections of young and old WT and GLA KO mice. (F) Measurement of total vascularization in DRG of young and old WT and GLA O mice. (G) Quantification of blood vessel branching points/mm² CBRA in DRG of young and old GLA KO mice. (H) Measurement of total blood vessel branch length/mm CBRA in DRG of young and old WT and GLA KO mice. (I) Measurement of the average blood vessel thickness in DRG of young and old WT and GLA KO mice. Abbreviations: CD31: cluster of differentiation 31; DRG: dorsal root ganglion; GLA KO: alpha-galactosidase A knockout; WT: wild type. *p<0.05; **p<0.01; ***p<0.001. Scale bar: 100 µm.

5.5 Behavioral profile of the GLA KO mouse model

5.5.1 No mechanical hypersensitivity and age-dependent heat hyposensitivity in GLA KO mice compared to WT mice

We performed behavioral testing on young and old GLA KO and WT mice after mechanical and heat stimulation. Young and old GLA KO mice do not show differences after mechanical stimulation with von Frey filaments compared to each other on to age-matched WT mice (Fig. 21A). Young and old GLA KO mice show an age-dependent increase in paw withdrawal latencies after heat stimulation with IR (p<0.001, Fig. 21B). Young and old WT mice do show the same age-dependent heat hyposensitivity development after heat stimulation (p<0.001, Fig. 21B).

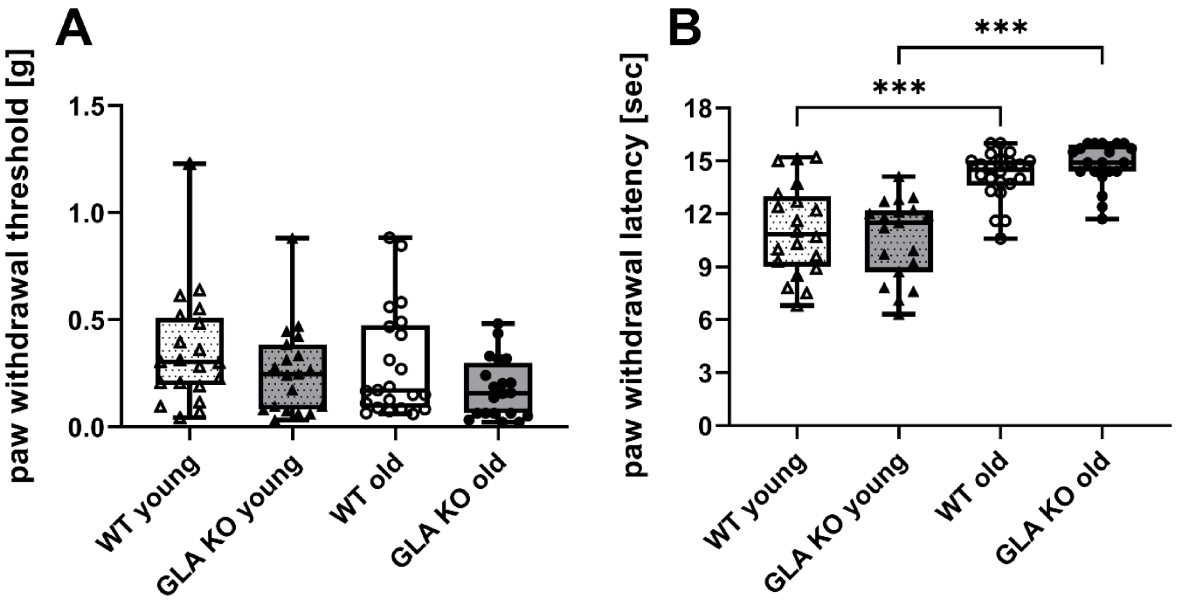

Figure 21: Assessment of the baseline behavioral profile of young and old WT and GLA KO mice in the von Frey and Hargreaves testing.
(A) Paw withdrawal thresholds after mechanical stimulation with von Frey filaments of young and old WT and GLA KO mice. (B) Paw withdrawal latencies after heat stimulation of young and old WT and GLA KO mice. Abbreviations: g: gram; GLA KO: alpha-galactosidase A knockout; sec: seconds; WT: wild type. ***p<0.001.

5.5.2 Mechanical and thermal sensitivities after administration of three capsaicin doses

Asssuming capsaicin hypersensitivity of the GLA KO mice, we systematically tested three capsaicin doses (0.2, 1, and 5 µg capsaicin/10 µl NaCl) to assess the suitable dosage to elicit heat-dependent nocifensive behavior in GLA KO mice but not in WT mice. We included young and old GLA KO and WT mice for capsaicin dosage testing and as control groups treated with 10 µl NaCl. Our results showed no mechanical hypersensitivity after administration of 5 µg capsaicin/10 µl NaCl in any group (Fig. 22). Heat hypersensitivity was not elicited in any group (Fig. 23) except for young WT mice at the dosage of 5 µg capsaicin/10 µl NaCl at 1 h post-capsaicin in the Hargreaves test ($p<0.05$, Fig. 23A). Similar to the administration of 5 µg capsaicin/10 µl NaCl, mechanical or heat hypersensitivity were not elicited under administration of 0.2 (see section 8.10, Fig. 27 and 28, respectively) and 1 µg capsaicin/10 µl NaCl (see section 8.10, Fig. 29 and 30, respectively). The results of the control groups treated with 10 µl

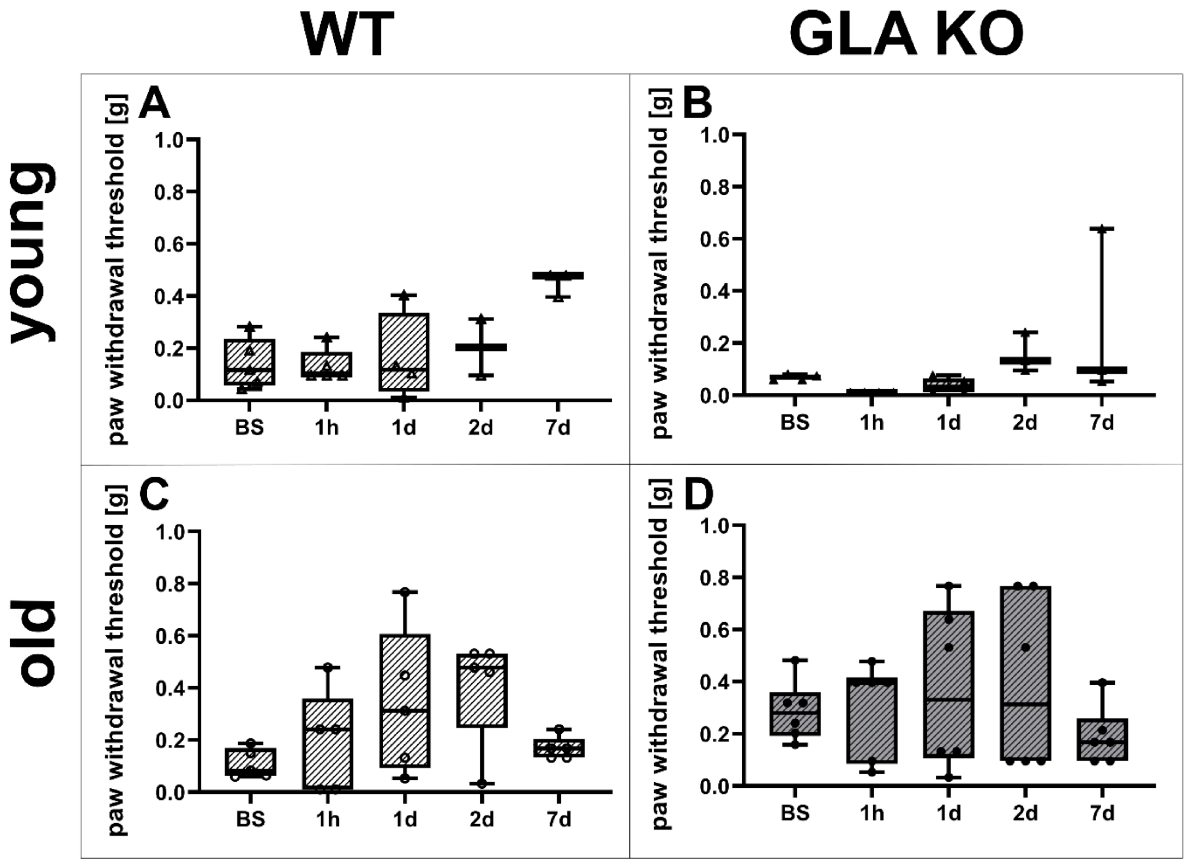

Figure 22: Assessment of the behavioral profile before (at baseline, BS) and after i.pl. 5 µg capsaicin/10 µl NaCl administration of young and old WT and GLA KO mice in the von Frey testing.
(A-D) Paw withdrawal thresholds after mechanical stimulation with von Frey filaments of young and old WT and GLA KO mice before and after i.pl. capsaicin administration at different time points (1h, 1d, 2d, and 7d post-Capsaicin). Abbreviations: BS: baseline; d: days; g: gram; GLA KO: alpha-galactosidase A knockout; h: hour; i.pl.: intraplantar; NaCl: sodium chloride; WT: wild type.

NaCl showed no mechanical and heat hypersensitivity (see section 8.10, Fig. 31 and 32, respectively).

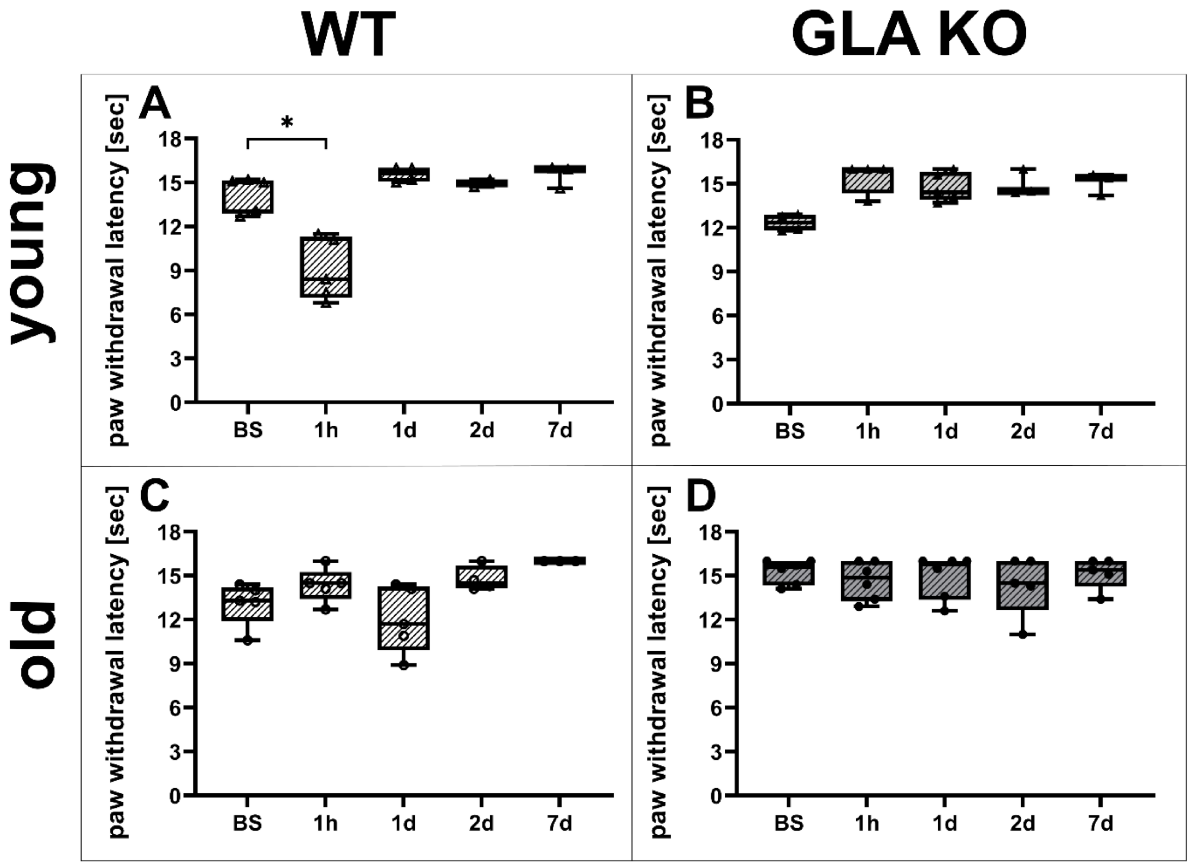

Figure 23: Assessment of the behavioral profile before (at baseline, BS) and after i.pl. 5 µg capsaicin/10 µl NaCl administration of young and old WT and GLA KO mice in the Hargreaves testing.
(A-D) Paw withdrawal latencies after heat stimulation of young and old WT and GLA KO mice before and after i.pl. capsaicin administration at different time points (1h, 1d, 2d, and 7d post-Capsaicin). Abbreviations: BS: baseline; d: days; GLA KO: alpha-galactosidase A knockout; h: hour; i.pl.: intraplantar; sec: seconds; WT: wild type. *p<0.05.

5.5.3 Behavioral long-term evaluation on the GLA KO mouse model after repeated ERT administration

We tested young WT and GLA KO mice, that received ERT administration every other month, over a period of 1.5 years every third month to assess their behavioral profile under treatment and NaCl administration as control condition. We found no differences in mechanical sensitivity of WT and GLA KO under ERT and NaCl (Fig. 24A-D). WT mice under NaCl treatment showed mechanical hypersensitivity development at the age of 3, 6, and 15 months ($p<0.05$, Fig. 24A) compared to BS before treatment, while GLA KO mice under NaCl treatment showed mechanical hypersensitivity development at the age of 3 and 6 months ($p<0.01$, Fig. 24B) compared to BS before treatment. WT mice under ERT developed, as seen in the control NaCl group, mechanical hypersensitivity at the age of 3, 6, and 15 months ($p<0.05$, Fig. 24C) compared to BS before ERT indicating no effect of the ERT on mechanical hypersensitivity development. GLA KO mice developed, similar to the NaCl control group, mechanical hypersensitivity at the age of 6 months ($p<0.05$, Fig. 24D) compared to BS before ERT. WT and GLA KO mice developed heat hyposensitivity over the testing period irrespective of treatment with ERT or NaCl ($p<0.05$, Fig. 25A-D), indicating no efficacy of ERT to maintain heat sensitivities at BS level.

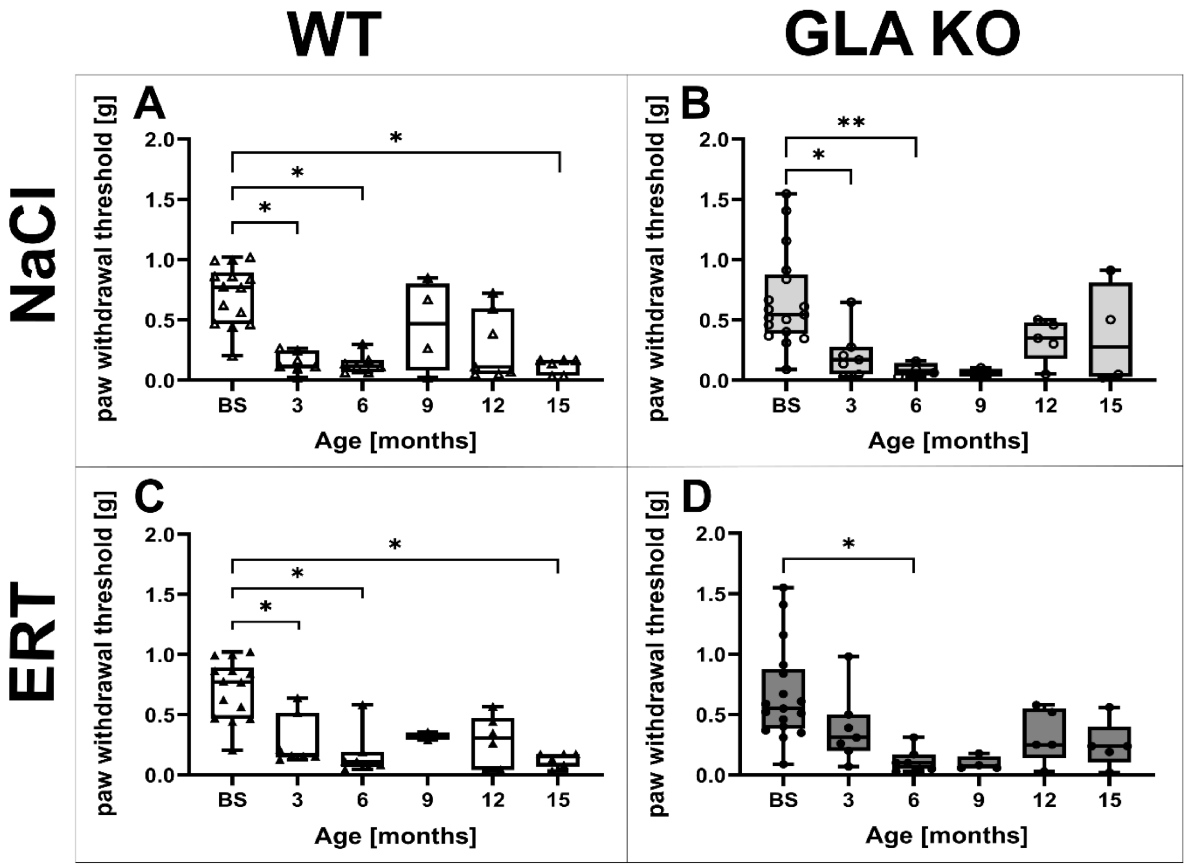

Figure 24: Long-term assessment of the behavioral profile before (at baseline, BS) and after repeated i.v. 1 µg/g BW ERT administration of young WT and GLA KO mice in the von Frey testing.
(A-D) Paw withdrawal thresholds after mechanical stimulation every third month with von Frey filaments of young and old WT and GLA KO mice before and after i.v. ERT administration (every other month). Abbreviations: BS: baseline; BW: body weight; ERT: enzyme replacement therapy; g: gram; GLA KO: alpha-galactosidase A knockout; i.v.: intravenous; NaCl: sodium chloride; WT: wild type. *p<0.05; **p<0.01.

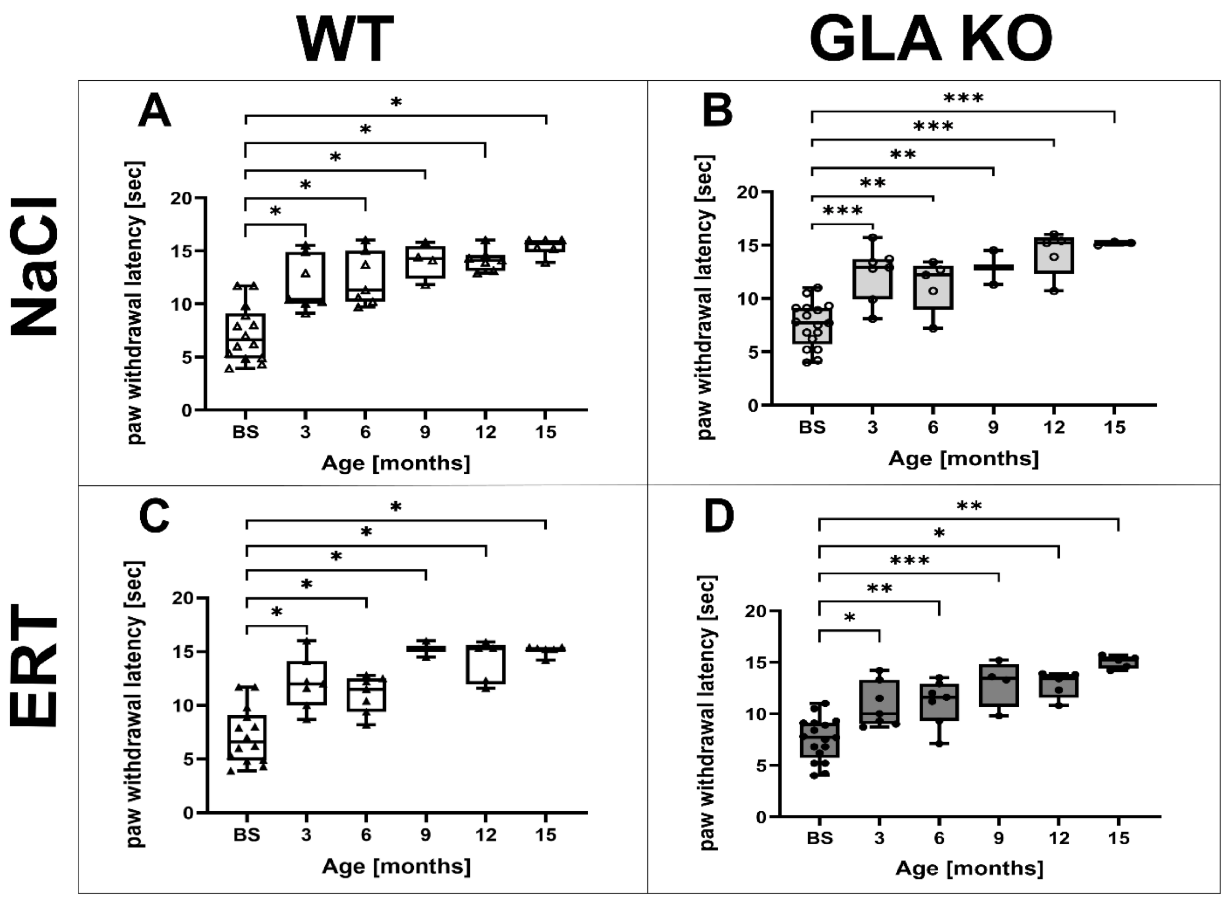

Figure 25: Long-term assessment of the behavioral profile before (at baseline, BS) and after repeated i.v. 1 µg/g BW ERT administration of young WT and GLA KO mice in the Hargreaves testing.
(A-D) Paw withdrawal latencies after heat stimulation every third month of young and old WT and GLA KO mice before and after i.v. ERT administration (every other month). Abbreviations: BS: baseline; BW: body weight; ERT: enzyme replacement therapy; GLA KO: alpha-galactosidase A knockout; i.v.: intravenous; NaCl: sodium chloride; sec: seconds; WT: wild type. *p<0.05; **p<0.01; ***p<0.001.

6. Discussion

6.1 Summary of the main results

This thesis aimed to elucidate the impact of potential inflammatory, hypoxic, and vascular pathomechanisms on the development of a FD pain-like phenotype in the GLA KO mouse model. We found a higher Gb3 load in DRG of young and old GLA KO mice compared to their age-matched WT littermates, which could contribute to physical occlusion and compression of different cell types located within whole DRG and activate inflammatory and hypoxic mechanisms on cellular level in DRG neurons and endothelial cells. Investigations on inflammation-associated targets in DRG tissue of GLA KO and WT mice revealed an overall downregulation of immune responses in terms of reduced pro- and anti-inflammatory markers on gene expression levels and lower numbers of $CD206^+$ macrophages with no clear shift towards a pro- or anti-inflammatory environment on DRG level. Investigations of hypoxia-associated mechanisms in whole DRG and DRG neuronal cell cultures of GLA KO and WT mice showed different results. In whole DRG tissue, hypoxia-associated genes were upregulated in DRG of old GLA KO mice compared to old WT mice paralleled by cytosolic-nuclear translocation of HIF1α and upregulation of its downstream-target CA9 on protein expression level, which indicates involvement of chronic hypoxic mechanisms on DRG level of GLA KO mice (Batie et al., 2022; Lin et al., 2011; Schödel & Ratcliffe, 2019). In DRG neuronal cell cultures cultivated under hypoxic conditions, hypoxia-associated target genes were upregulated in both genotypes under hypoxic conditions compared to normoxic conditions, while the number of $HIF1\alpha^+$ and $CA9^+$ immunoreactive neurons did not differ. This may hint towards an involvement of acute short-term hypoxic mechanisms, which are not sufficient to elicit dysregulation of specific hypoxia-associated key players on protein expression level (Batie et al., 2022; Lin et al., 2011; Schödel & Ratcliffe, 2019). Further, vascularization analysis in DRG of GLA KO and WT mice showed a reduction in several blood vessel properties and total vascularization of whole DRG of GLA KO mice, which either results out of physical occlusion of cells via increased Gb3 accumulation or as a consequence of activated hypoxic, induced DNA-damage, and cellular stress mechanisms. To link the molecular data to the pain-like behavior of the GLA KO mouse model, BS assessment of mechanical and heat sensitivities was performed, which did not show a clear pain-like phenotype as in patients (Üçeyler et al., 2011; Üçeyler et al., 2013; Weissmann et al.,

2021) and previous studies using the GLA KO mouse model (Ashe et al., 2015; Bangari et al., 2015; Marshall et al., 2010; Üçeyler et al., 2016). Additionally in this thesis, the GLA KO mouse model was not triggerable with several capsaicin doses to elicit a nocifensive pain-like profile. Since no clear pain-like profile was present in GLA KO mice, rescue experiments with ERT were not meaningful. Furthermore, ERT did not change mechanical and heat sensitivities in both WT and GLA KO mice.

6.2 Impact of Gb3 accumulation on DRG cellular and molecular pathology

Gb3 is known to accumulate in several cell types including renal, cardiac, endothelial, and neuronal cells (Jabbarzadeh-Tabrizi et al., 2020; Tuttolomondo et al., 2021). In this thesis, the Gb3 load in DRG of young and old GLA KO mice was higher compared to age-matched WT littermates, but did not change in an age-dependent manner within GLA KO mice. Still, the direct impact of pathological Gb3 accumulation on cellular and molecular pathomechanisms of FD is elusive. Different studies suggested that Gb3 can elicit immune responses by activating either toll-like receptors (TLRs) or interfering with calcium-activated potassium 3.1 (KCa3.1) channels leading subsequently to the initiation of inflammatory processes or endothelial cell disturbances (Biancini et al., 2012; Park et al., 2008; Rozenfeld & Feriozzi, 2017; Tuttolomondo et al., 2021). Several studies reported that endothelial cells are disturbed in FD *in vitro* models, which may be caused by functional impairment of the endothelial cell-associated ion channel KCa3.1 (Do et al., 2020; Namdar et al., 2012; Pollmann et al., 2021; Shu & Shayman, 2007; Tuttolomondo et al., 2021). It is suggested that endothelial impairment leads to activation of the inflammatory response and to microvasculopathies in several organs (Namdar et al., 2012; Tuttolomondo et al., 2021). So far, Gb3 accumulations were not known to induce directly hypoxic mechanisms on cellular level, but endothelial cell misfunction might be associated with activation of hypoxia mechanisms on DRG cellular level (Lim et al., 2015). Hypoxic environment in DRG might develop either through simple occlusion of the blood supply in the target organ via Gb3 accumulation in endothelial cells or neurons, or as a reciprocal response to immune responses against cellular Gb3 accumulation (Biancini et al., 2012; Taylor & Colgan, 2017). Further, it is reported that activated hypoxic mechanisms can influence directly or indirectly the functionality and expression of several ion channels, like acid-sensing ion channels (ASICs), transient receptor potential ankyrin (TRPA), transient receptor

potential melastatin (TRPM), transient receptor potential vanilloid ion channels (TRPV), calcium-activated potassium channels (KCa), potassium/sodium hyperpolarization-activated cyclic nucleotide-gated channels (HCN), and voltage-gated sodium channels (NaV), which are associated in different ways with pain-like phenotypes (Burand & Stucky, 2021; Chen et al., 2021; Miyake et al., 2016; Tran et al., 2017; Weissmann et al., 2021). Among pain-associated ion channels, KCa3.1 may link potential endothelial dysfunction with direct impact of Gb3 accumulation on KCa3.1 functionality and mechanical hypersensitivity seen in the GLA KO mouse model (Gao et al., 2010; Spitzel et al., 2022; Staal et al., 2017; Tseng et al., 2017). Another study reported the direct influence of Gb3 accumulation on voltage-gated calcium channels (CaV) in DRG neurons of Bl6 mice (Choi et al., 2015), indicating aberrant cellular Ca^{2+} fluxes in neurons, which can induce neuronal hyperexcitability and endothelial cell dysfunction leading to impaired blood vessel contraction characteristics (Choi et al., 2015; Gao et al., 2010; Tseng et al., 2017; Tuttolomondo et al., 2021). Subsequently, aberrant Ca^{2+} fluxes can influence KCa3.1 channels in endothelial cells and induce ROS production, which leads to inflammatory cascades contributing to the potential inflammation-hypoxia-crosstalk in FD pathophysiology (Taylor & Colgan, 2017; Tseng et al., 2017). Impairment on the level of ion channel expression and functionality, potentially mediated directly via Gb3 or Gb3-associated molecular pathomechanisms, was extensively reported in FD animal and *in vitro* models (Burand & Stucky, 2021; Choi et al., 2015; Hofmann et al., 2018; Lakoma et al., 2016; Namer et al., 2017; Rickert et al., 2020; Spitzel et al., 2022; Weissmann et al., 2021) suggesting a link between ion channel alteration and pain-like behavioral phenotypes in especially in the GLA KO mouse model (Choi et al., 2015; Hofmann et al., 2018; Lakoma et al., 2016; Namer et al., 2017; Spitzel et al., 2022).

6.3 Immune responses in the DRG of the GLA KO mouse model

The involvement of inflammatory pathways in the pathophysiology of FD patients and FD animal models is widely discussed. Several studies with FD patients showed an impact of systemic pro-inflammatory pathways on FD pathophysiology systemically mediated by increased expression of pro-inflammatory cyto- and chemokines, like TNFα, TLR4, and IL-1β, and downregulated anti-inflammatory cyto- and chemokines, like IL4 (De Francesco et al., 2013; Mauhin et al., 2015; Üçeyler et al., 2019). In contrast, animal studies performed with FD rat and mouse models showed contradictory results. In a FD rat model, increased infiltration rates of $CD68^+$ macrophages into the skin of FD rats were reported (Miller et al., 2019). Similarly, in a GLA KO/Gb3 synthase knockin ($Gla^{tm}Tg$ (CAG-A4GALT)) mouse model increased numbers of $F4/80^+$ macrophages were assessed in kidney tissue (Maruyama et al., 2018). Both studies indicate a contribution of pro-inflammatory mechanisms in those FD rodent models, while one study using the GLA KO mouse model demonstrated downregulation of immune response-associated target mRNA levels in DRG of GLA KO mice (Kummer et al., 2017). In this thesis, we reported similar findings as Kummer et al. We demonstrated downregulated immune response-associated markers, including *IL-1β*, *IL10*, *GFAP*, and *LRG1*, and lower numbers of $CD206^+$ macrophages in DRG tissue of GLA KO mice. Our results suggest that on DRG level in GLA KO mice, immune responses potentially against Gb3 or other FD-associated pathomechanisms are shut down irrespective of a pro- or anti-inflammatory shift. Suppression of immune responses can be mediated via pattern recognition receptors (PRR), which are expressed on several immune cells, can recognize damaged and apoptotic cells, and induce phagocytosis. Active PRR can lead to a suppression of immune responses to avoid exaggerated autoimmunity during phagocytosis of apoptotic or Gb3-filled cells (Jeannin et al., 2008). This immune response pathway might explain the overall reduced immune response in DRG of GLA KO mice in this thesis. Another study working with the GLA KO mouse model reported downregulated mRNA levels in DRG of male GLA KO mice being associated with the major histocompatibility complex and interferon-mediated processes, while mRNA expression levels associated with the myeloid immune response were upregulated. Further, the number of $CD68^+$ macrophages was higher in DRG of GLA KO mice indicating the involvement of pro-inflammatory mechanisms in the FD pathophysiology (Choconta et al., 2023). As suggested in other publications (Delprat et al., 2020; Lin et

al., 2023; Parisi et al., 2018; Xu et al., 2017), we assessed the infiltration rates of specific M1 pro- and M2 anti-inflammatory macrophage subtypes with respective markers. Specific classification of macrophages into M1 and M2 macrophages is nevertheless highly debated and thought to not fully capture the role of macrophages being present in the investigated target organs, like DRG of GLA KO mice (Paolicelli et al., 2022). It is elusive how our data of reduced numbers of $CD206^{+}$ macrophages, in this thesis classified as M2, in DRG of GLA KO mice can be interpreted in terms of immune response mechanisms in FD pathophysiology. Thus, the exact immune response mechanisms in FD pathophysiology in FD patients and FD animal models are still controversially discussed.

6.4 Hypoxic mechanisms and vasculopathy in DRG of the GLA KO mouse model

The involvement of hypoxia in FD pathophysiology is barely investigated. Only one publication reported relative hypoxia in extremities of FD patients after performance of semi-ischemic exercises suggesting already a contribution of vasculopathy to a FD pain phenotype (Inagaki et al., 1992). In this thesis, we demonstrated in DRG of GLA KO mice a hypoxic environment reflected by supporting data on gene and protein expression level. Our results suggest the involvement of hypoxic mechanisms in FD molecular pathophysiology due to increased hypoxia-associated target genes, subsequently leading to cellular stress and DNA damage mediated via upregulated gene expression of *DDIT4*, *HK2*, *LGALS3*, and *TFRC*. Several studies revealed that neuronal apoptosis, energy metabolism disturbance, and energy supply imbalance due to impaired mitochondrial functionality are main contributors in FD pathophysiology, which can be linked to DNA damage-associated and cellular stress-inducible genes including those being investigated in this study (Hofmann et al., 2018; Rajan et al., 2021; Tuttolomondo et al., 2021). Further, the cytosolic-nuclear translocation of the transcription factor and hypoxia sensor HIF1α, and increased protein expression of CA9 in DRG of GLA KO mice support additionally our hypothesis of a chronic hypoxic status in this rodent model (Lin et al., 2011; Reiterer et al., 2019; Saxena & Jolly, 2019). Our studies with DRG neuronal cell cultures under short-term (< 24 h) hypoxia revealed differences for specific targets only on gene expression level. Those gene targets were sensitive for hypoxic stimulation but did not differ between genotypes except for

LGALS3, which might be a suitable sensor for short-term changes in hypoxic environments. LGALS3 is known to interact with PRR and is involved in the initiation of immune responses. Further, this molecule interacts closely with glycoproteins and glycolipids at least in different brain cell types (Garcia-Revilla et al., 2022). Hypoxic events can be related to vascular impairment and endothelial dysfunction. There is evidence that vascular alterations are involved in FD pathophysiology in terms of cardiomyopathy (Sorriento & Iaccarino, 2019). Further, involvement of microvasculopathy in FD patients in the central nervous system (CNS) are reflected by stroke events (Inan et al., 2020; Kong et al., 2019; Mishra et al., 2020). FD patients additionally show angiokeratomas and microvasculopathy in kidney and heart suggesting altered of vascular characteristics also in the peripheral nervous system (PNS) (Inan et al., 2020; Kong et al., 2019). Another MRI study demonstrated that in DRG of FD patients, blood vessel perfusion and leakiness is impaired (Godel et al., 2017), supporting our hypothesis that vasculopathy occurs in the PNS. *In vitro* studies working with FD endothelial cells reported endothelial dysfunction in terms of impaired morphology, leakiness, and altered tube formation properties (Choi et al., 2023; Do et al., 2020; Namdar et al., 2012; Pollmann et al., 2021). Those support our data in this thesis, where we found reduced vascularization, number of blood vessel branches, and total blood vessel length in DRG of GLA KO mice. One study investigated potential targets to rescue impaired tube formation of FD endothelial cells mediated via high expression of thrombospondin 1 (TSP1), an angiogenesis suppressor. Using Fasudil, a RhoA/Rho kinase inhibitor, showed a reduction of TSP1 levels in FD endothelial cells, restored endothelial cell morphology and tube formation, increased levels of proangiogenic factors like vascular endothelial growth factor alpha (VEGFα), and reduced inflammation-associated gene expression (Choi et al., 2023). Especially the reduction of inflammatory markers suggests an involvement of dysregulated immune responses. Another study on the impact of Gb3 on FD endothelial cells showed that key endothelial cell pathways, involving cyclooxygenase 1- and -2 (COX1, COX2), were deregulated (Namdar et al., 2012). COX1 and 2 are involved in the proper functionality of blood vessel contraction and can be inhibited via the administration of NSAID (Bindu et al., 2020; Weissmann et al., 2021). Some FD patients reported that NSAID administration alleviated symptoms like pain attacks suggesting that deregulated immune responses and altered blood vessel functionality and perfusion might play indeed a role in pain development in FD patients (Politei et al., 2016;

Weissmann et al., 2021). Still, it is unclear whether hypoxia is caused by disturbed immune responses leading to vasculopathy via cellular stress and apoptosis or hypoxia is caused by vascular impairment and occlusion in morphological level via Gb3 accumulation inducing subsequently a hypoxic environment in different cell types located in the DRG.

6.5 Pain-like characteristics of the GLA KO mouse model and its modulation

The GLA KO mouse model is a well-established FD rodent model to investigate different aspects of FD pathophysiology (Ohshima et al., 1997). Several studies characterized this model in terms of Gb3 deposits in different cell types, molecular mechanisms, and behavioral pain-like profiles (Bangari et al., 2015; Choconta et al., 2023; Hofmann et al., 2018; Jabbarzadeh-Tabrizi et al., 2020; Lakoma et al., 2016; Marshall et al., 2010; Namer et al., 2017; Ohshima et al., 1997; Park et al., 2009; Üçeyler et al., 2016). In particular, pain-like behavioral characteristics and associated *in vitro* studies on DRG neuronal cell cultures using electrophysiology reported different insights into pain-like behavior mimicking FD patients' pain profiles (Choi et al., 2015; Hofmann et al., 2018; Namer et al., 2017; Üçeyler et al., 2016). Still, the GLA KO mouse model displays contradictory behavioral pain-like profiles when investigated by different scientific groups. Two studies reported that GLA KO mice show mechanical hypersensitivity at young and old ages, while heat hyposensitivity developed over time in old animals (Bangari et al., 2015; Üçeyler et al., 2016). In contrast, another study showed no difference in mechanical sensitivity between age- and genotype-groups, and heat hyposensitivity was only present in old groups irrespective of genotype (Hofmann et al., 2018). A fourth study showed mechanical hypersensitivity in WT mice compared to GLA KO mice, while heat hyposensitivity was present in GLA KO mice compared to WT mice (Namer et al., 2017). In this thesis, we demonstrated that no animal groups stratified for age and genotype showed mechanical hypersensitivity, while heat hyposensitivity developed over age in both WT and GLA KO mice. Contradictory results in the GLA KO mouse model pain-like phenotype might occur due to different testing environments, varying performances of different investigators, or different genetic background of the animals (Mogil et al., 2006; Mogil et al., 1999). Further, we were not able to elicit nocifensive responses after i.pl. capsaicin

administration. Capsaicin as a TRPV1 agonist elicits a rapid and transient hypersensitivity in rodent models for several minutes (Brenchat et al., 2009; Carey et al., 2017; Entrena et al., 2009). Our data suggests that nocifensive behavior after capsaicin administration is suppressed or modulated via isoflurane anesthesia, which was necessary during administration. Isoflurane is suspected to interact with different ion channels like TRPM3 or TRPV1 and modulate their functionality (Jorgensen & Domene, 2018; Kelemen et al., 2020). Further, due to no differences in BS behavior in this thesis, potential rescue experiments with ERT were not well interpretable. One study investigating the effect of ERT in GLA KO mice could not alleviate the development of heat hyposensitivity in GLA KO mice. Only by adding SRT to ERT, an efficacy was visible in terms of restored paw withdrawal latencies to BS level in GLA KO mice after heat stimulation (Ashe et al., 2015). Taken together, the GLA KO mouse model gives us valuable insight into molecular alterations potentially being associated with Gb3 accumulation or further not fully understood pathomechanisms of FD, while as a pain-like behavioral model it shows a high variability, which limits its value to investigate behavioral pain-like profiles.

6.6 Potential pathomechanisms in the DRG of the GLA KO mouse model

Based on the data presented in this thesis, we suggest following pathomechanisms in the DRG of GLA KO mice, which might contribute to FD pathophysiology and to FD pain development either directly or indirectly. Gb3 accumulation occurs in particular in DRG neurons and endothelial cells of DRG capillaries. This event potentially causes alterations in two in parallel pathways:

1) Vascular occlusion due to Gb3 in neurons or endothelial cells might lead to a hypoxic environment in DRG.
2) Disturbed immune responses against Gb3 accumulation might lead to cellular stress induction and apoptosis of different cell types including neurons and endothelial cells.

Overall, both altered pathways might lead to high cellular stress levels, reflected by increased expression of DNA damage-associated markers in whole DRG of GLA mice. Alterations in hypoxic and immune response pathways can influence directly ion channel expression and functionality, as suggested in previous work (Spitzel et al., 2022), leading potentially to a pain-like phenotype, which we were not able to

reproduce, but might be an evidence for an involvement of mentioned pathways in FD pain-like behavior. Still in this thesis, pain-like behavior in the GLA KO mouse model was not reproducible at BS level, not triggerable via capsaicin, and not rescuable via ERT administration suggesting that our data gives only robust insight into altered molecular pathomechanisms associated with FD pathophysiology on DRG level of GLA KO mice.

6.7 Outlook

Further investigations will be needed to elucidate in more detail how hypoxic and immune response mechanisms in DRG of GLA KO mice can influence directly pain-like FD phenotypes, which are highly heterogenous even in FD patients. In depth investigation of identified potential key players being involved in FD pathophysiology might lead in future to new therapeutic options for FD patients to alleviated FD pain phenotypes and associated vasculopathies.

7. References

Arends, M., Wanner, C., Hughes, D., Mehta, A., Oder, D., Watkinson, O. T., Elliott, P. M., Linthorst, G. E., Wijburg, F. A., Biegstraaten, M., & Hollak, C. E. (2017, May). Characterization of Classical and Nonclassical Fabry Disease: A Multicenter Study. *J Am Soc Nephrol, 28*(5), 1631-1641. https://doi.org/10.1681/ASN.2016090964

Ashe, K. M., Budman, E., Bangari, D. S., Siegel, C. S., Nietupski, J. B., Wang, B., Desnick, R. J., Scheule, R. K., Leonard, J. P., Cheng, S. H., & Marshall, J. (2015, Apr 30). Efficacy of Enzyme and Substrate Reduction Therapy with a Novel Antagonist of Glucosylceramide Synthase for Fabry Disease. *Mol Med, 21*(1), 389-399. https://doi.org/10.2119/molmed.2015.00088

Azevedo, O., Gago, M. F., Miltenberger-Miltenyi, G., Sousa, N., & Cunha, D. (2020, Dec 28). Fabry Disease Therapy: State-of-the-Art and Current Challenges. *Int J Mol Sci, 22*(1). https://doi.org/10.3390/ijms22010206

Bangari, D. S., Ashe, K. M., Desnick, R. J., Maloney, C., Lydon, J., Piepenhagen, P., Budman, E., Leonard, J. P., Cheng, S. H., Marshall, J., & Thurberg, B. L. (2015, Mar). alpha-Galactosidase A knockout mice: progressive organ pathology resembles the type 2 later-onset phenotype of Fabry disease. *Am J Pathol, 185*(3), 651-665. https://doi.org/10.1016/j.ajpath.2014.11.004

Batie, M., Frost, J., Shakir, D., & Rocha, S. (2022, Mar 31). Regulation of chromatin accessibility by hypoxia and HIF. *Biochem J, 479*(6), 767-786. https://doi.org/10.1042/BCJ20220008

Biancini, G. B., Vanzin, C. S., Rodrigues, D. B., Deon, M., Ribas, G. S., Barschak, A. G., Manfredini, V., Netto, C. B., Jardim, L. B., Giugliani, R., & Vargas, C. R. (2012, Feb). Globotriaosylceramide is correlated with oxidative stress and inflammation in Fabry patients treated with enzyme replacement therapy. *Biochim Biophys Acta, 1822*(2), 226-232. https://doi.org/10.1016/j.bbadis.2011.11.001

Bindu, S., Mazumder, S., & Bandyopadhyay, U. (2020, Oct). Non-steroidal anti-inflammatory drugs (NSAIDs) and organ damage: A current perspective. *Biochem Pharmacol, 180*, 114147. https://doi.org/10.1016/j.bcp.2020.114147

Braunstein, H., Papazian, M., Maor, G., Lukas, J., Rolfs, A., & Horowitz, M. (2020, Oct 7). Misfolding of Lysosomal alpha-Galactosidase a in a Fly Model and Its Alleviation by the Pharmacological Chaperone Migalastat. *Int J Mol Sci, 21*(19). https://doi.org/10.3390/ijms21197397

Brenchat, A., Romero, L., Garcia, M., Pujol, M., Burgueno, J., Torrens, A., Hamon, M., Baeyens, J. M., Buschmann, H., Zamanillo, D., & Vela, J. M. (2009, Feb). 5-HT7 receptor activation inhibits mechanical hypersensitivity secondary to capsaicin sensitization in mice. *Pain, 141*(3), 239-247. https://doi.org/10.1016/j.pain.2008.11.009

Breyer, M., Klein, T., Klug, K., Klopocki, E., & Üçeyler, N. (2022, May). Generation of the induced pluripotent stem cell line UKWNLi005-A derived from a patient with the GLA mutation c.376A > G of unknown pathogenicity in Fabry disease. *Stem Cell Res, 61*, 102747. https://doi.org/10.1016/j.scr.2022.102747

Burand, A. J., Jr., & Stucky, C. L. (2021, May 1). Fabry disease pain: patient and preclinical parallels. *Pain, 162*(5), 1305-1321. https://doi.org/10.1097/j.pain.0000000000002152

Carey, L. M., Gutierrez, T., Deng, L., Lee, W. H., Mackie, K., & Hohmann, A. G. (2017, Apr 20). Inflammatory and Neuropathic Nociception is Preserved in GPR55 Knockout Mice. *Sci Rep, 7*(1), 944. https://doi.org/10.1038/s41598-017-01062-2

Chaplan, S. R., Bach, F. W., Pogrel, J. W., Chung, J. M., & Yaksh, T. L. (1994, Jul). Quantitative assessment of tactile allodynia in the rat paw. *J Neurosci Methods, 53*(1), 55-63. https://doi.org/10.1016/0165-0270(94)90144-9

Chen, J., Zhang, M., Ma, Z., Yuan, D., Zhu, J., Tuo, B., Li, T., & Liu, X. (2021, Aug). Alteration and dysfunction of ion channels/transporters in a hypoxic microenvironment results in the development and progression of gastric cancer. *Cell Oncol (Dordr), 44*(4), 739-749. https://doi.org/10.1007/s13402-021-00604-1

Choconta, J. L., Labi, V., Dumbraveanu, C., Kalpachidou, T., Kummer, K. K., & Kress, M. (2023, May 12). Age-related neuroimmune signatures in dorsal root ganglia of a Fabry disease mouse model. *Immun Ageing, 20*(1), 22. https://doi.org/10.1186/s12979-023-00346-8

Choi, J. B., Seol, D. W., Do, H. S., Yang, H. Y., Kim, T. M., Byun, Y. G., Park, J. M., Choi, J., Hong, S. P., Chung, W. S., Suh, J. M., Koh, G. Y., Lee, B. H., Wee, G., & Han, Y. M. (2023, Apr 5). Fasudil alleviates the vascular endothelial dysfunction and several phenotypes of Fabry disease. *Mol Ther, 31*(4), 1002-1016. https://doi.org/10.1016/j.ymthe.2023.02.003

Choi, L., Vernon, J., Kopach, O., Minett, M. S., Mills, K., Clayton, P. T., Meert, T., & Wood, J. N. (2015, May 6). The Fabry disease-associated lipid Lyso-Gb3 enhances voltage-gated calcium currents in sensory neurons and causes pain. *Neurosci Lett, 594*, 163-168. https://doi.org/10.1016/j.neulet.2015.01.084

Cui, S., Shin, Y. J., Ko, E. J., Lim, S. W., Ju, J. H., Lee, K. I., Lee, J. Y., Yang, C. W., & Chung, B. H. (2021, Mar). Human-induced pluripotent stem cell lines (CMCi006-A and CMCi007-A) from a female and male patient with Fabry disease carrying the same frameshift deletion mutation. *Stem Cell Res, 51*, 102214. https://doi.org/10.1016/j.scr.2021.102214

De Francesco, P. N., Mucci, J. M., Ceci, R., Fossati, C. A., & Rozenfeld, P. A. (2013, May). Fabry disease peripheral blood immune cells release inflammatory cytokines: role of globotriaosylceramide. *Mol Genet Metab, 109*(1), 93-99. https://doi.org/10.1016/j.ymgme.2013.02.003

Delprat, V., Tellier, C., Demazy, C., Raes, M., Feron, O., & Michiels, C. (2020, Jan 21). Cycling hypoxia promotes a pro-inflammatory phenotype in macrophages via JNK/p65 signaling pathway. *Sci Rep, 10*(1), 882. https://doi.org/10.1038/s41598-020-57677-5

Do, H. S., Park, S. W., Im, I., Seo, D., Yoo, H. W., Go, H., Kim, Y. H., Koh, G. Y., Lee, B. H., & Han, Y. M. (2020, Feb). Enhanced thrombospondin-1 causes dysfunction of vascular endothelial cells derived from Fabry disease-induced pluripotent stem cells. *EBioMedicine, 52*, 102633. https://doi.org/10.1016/j.ebiom.2020.102633

Duarte, A. J., Ribeiro, D., Santos, R., Moreira, L., Braganca, J., & Amaral, O. (2020, May). Induced pluripotent stem cell line (INSAi002-A) from a Fabry Disease patient hemizygote for the rare p.W287X mutation. *Stem Cell Res, 45*, 101794. https://doi.org/10.1016/j.scr.2020.101794

Elsaid, H. O. A., Furriol, J., Blomqvist, M., Diswall, M., Leh, S., Gharbi, N., Anonsen, J. H., Babickova, J., Tondel, C., Svarstad, E., Marti, H. P., & Krause, M. (2022, Jun). Reduced alpha-galactosidase A activity in zebrafish (Danio rerio) mirrors distinct features of Fabry nephropathy phenotype. *Mol Genet Metab Rep, 31*, 100851. https://doi.org/10.1016/j.ymgmr.2022.100851

Elsaid, H. O. A., Tjeldnes, H., Rivedal, M., Serre, C., Eikrem, O., Svarstad, E., Tondel, C., Marti, H. P., Furriol, J., & Babickova, J. (2022, Dec 26). Gene Expression Analysis in gla-Mutant Zebrafish Reveals Enhanced Ca(2+) Signaling Similar to Fabry Disease. *Int J Mol Sci, 24*(1). https://doi.org/10.3390/ijms24010358

Entrena, J. M., Cobos, E. J., Nieto, F. R., Cendan, C. M., Baeyens, J. M., & Del Pozo, E. (2009, Jul). Antagonism by haloperidol and its metabolites of mechanical hypersensitivity induced by intraplantar capsaicin in mice: role of sigma-1 receptors. *Psychopharmacology (Berl), 205*(1), 21-33. https://doi.org/10.1007/s00213-009-1513-8

Gao, Y., Balut, C. M., Bailey, M. A., Patino-Lopez, G., Shaw, S., & Devor, D. C. (2010, Jun 4). Recycling of the Ca2+-activated K+ channel, KCa2.3, is dependent upon RME-1, Rab35/EPI64C, and an N-terminal domain. *J Biol Chem, 285*(23), 17938-17953. https://doi.org/10.1074/jbc.M109.086553

Garcia-Revilla, J., Boza-Serrano, A., Espinosa-Oliva, A. M., Soto, M. S., Deierborg, T., Ruiz, R., de Pablos, R. M., Burguillos, M. A., & Venero, J. L. (2022, Jul 20). Galectin-3, a rising star in modulating microglia activation under conditions of neurodegeneration. *Cell Death Dis, 13*(7), 628. https://doi.org/10.1038/s41419-022-05058-3

Germain, D. P., Elliott, P. M., Falissard, B., Fomin, V. V., Hilz, M. J., Jovanovic, A., Kantola, I., Linhart, A., Mignani, R., Namdar, M., Nowak, A., Oliveira, J. P., Pieroni, M., Viana-Baptista, M., Wanner, C., & Spada, M. (2019, Jun). The effect of enzyme replacement therapy on clinical outcomes in male patients with Fabry disease: A systematic literature review by a European panel of experts. *Mol Genet Metab Rep, 19*, 100454. https://doi.org/10.1016/j.ymgmr.2019.100454

Germain, D. P., Levade, T., Hachulla, E., Knebelmann, B., Lacombe, D., Seguin, V. L., Nguyen, K., Noel, E., & Rabes, J. P. (2022, Apr). Challenging the traditional approach for interpreting genetic variants: Lessons from Fabry disease. *Clin Genet, 101*(4), 390-402. https://doi.org/10.1111/cge.14102

Godel, T., Baumer, P., Pham, M., Kohn, A., Muschol, N., Kronlage, M., Kollmer, J., Heiland, S., Bendszus, M., & Mautner, V. F. (2017, Sep 19). Human dorsal root ganglion in vivo morphometry and perfusion in Fabry painful neuropathy. *Neurology, 89*(12), 1274-1282. https://doi.org/10.1212/WNL.0000000000004396

Hargreaves, K., Dubner, R., Brown, F., Flores, C., & Joris, J. (1988, Jan). A new and sensitive method for measuring thermal nociception in cutaneous hyperalgesia. *Pain, 32*(1), 77-88. https://doi.org/10.1016/0304-3959(88)90026-7

Hofmann, L., Hose, D., Griesshammer, A., Blum, R., Doring, F., Dib-Hajj, S., Waxman, S., Sommer, C., Wischmeyer, E., & Üçeyler, N. (2018, Oct 17). Characterization of small fiber pathology in a mouse model of Fabry disease. *Elife, 7*. https://doi.org/10.7554/eLife.39300

Inagaki, M., Ohno, K., Hisatome, I., Tanaka, Y., & Takeshita, K. (1992, Sep). Relative hypoxia of the extremities in Fabry disease. *Brain Dev, 14*(5), 328-333. https://doi.org/10.1016/s0387-7604(12)80153-7

Inan, R., Mese, M., & Bicik, Z. (2020, Dec). Multidisciplinary approach to Fabry disease: from the eye of a neurologist. *Acta Neurol Belg, 120*(6), 1333-1339. https://doi.org/10.1007/s13760-019-01138-y

Ishii, S., Taguchi, A., Okino, N., Ito, M., & Maruyama, H. (2020, Apr 24). Determination of globotriaosylceramide analogs in the organs of a mouse model of Fabry disease. *J Biol Chem, 295*(17), 5577-5587. https://doi.org/10.1074/jbc.RA120.012665

Jabbarzadeh-Tabrizi, S., Boutin, M., Day, T. S., Taroua, M., Schiffmann, R., Auray-Blais, C., & Shen, J. S. (2020, Nov). Assessing the role of glycosphingolipids in the phenotype severity of Fabry disease mouse model. *J Lipid Res, 61*(11), 1410-1423. https://doi.org/10.1194/jlr.RA120000909

Jeannin, P., Jaillon, S., & Delneste, Y. (2008, Oct). Pattern recognition receptors in the immune response against dying cells. *Curr Opin Immunol, 20*(5), 530-537. https://doi.org/10.1016/j.coi.2008.04.013

Jorgensen, C., & Domene, C. (2018, Sep 4). Location and Character of Volatile General Anesthetics Binding Sites in the Transmembrane Domain of TRPV1. *Mol Pharm, 15*(9), 3920-3930. https://doi.org/10.1021/acs.molpharmaceut.8b00381

Kanack, A. J., Aoki, K., Tiemeyer, M., & Dahms, N. M. (2021, Aug). Platelet and myeloid cell phenotypes in a rat model of Fabry disease. *FASEB J, 35*(8), e21818. https://doi.org/10.1096/fj.202001727RR

Kaneski, C. R., Hanover, J. A., & Schueler Hoffman, U. H. (2022a, Jun). Generation of an in vitro model for peripheral neuropathy in Fabry disease using CRISPR-Cas9 in the nociceptive dorsal root ganglion cell line 50B11. *Mol Genet Metab Rep, 31*, 100871. https://doi.org/10.1016/j.ymgmr.2022.100871

Kaneski, C. R., Hanover, J. A., & Schueler Hoffman, U. H. (2022b, Dec). Generation of GLA-knockout human embryonic stem cell lines to model peripheral neuropathy in Fabry disease. *Mol Genet Metab Rep, 33*, 100914. https://doi.org/10.1016/j.ymgmr.2022.100914

Kelemen, B., Lisztes, E., Vladar, A., Hanyicska, M., Almassy, J., Olah, A., Szollosi, A. G., Penzes, Z., Posta, J., Voets, T., Biro, T., & Toth, B. I. (2020, Apr). Volatile anaesthetics inhibit the thermosensitive nociceptor ion channel transient receptor potential melastatin 3 (TRPM3). *Biochem Pharmacol, 174*, 113826. https://doi.org/10.1016/j.bcp.2020.113826

Klein, T., Gunther, K., Kwok, C. K., Edenhofer, F., & Üçeyler, N. (2018, Aug). Generation of the human induced pluripotent stem cell line (UKWNLi001-A) from skin fibroblasts of a woman with Fabry disease carrying the X-chromosomal heterozygous c.708 G > C (W236C) missense mutation in exon 5 of the alpha-galactosidase-A gene. *Stem Cell Res, 31*, 222-226. https://doi.org/10.1016/j.scr.2018.08.009

Kok, K., Zwiers, K. C., Boot, R. G., Overkleeft, H. S., Aerts, J., & Artola, M. (2021, Feb 12). Fabry Disease: Molecular Basis, Pathophysiology, Diagnostics and Potential Therapeutic Directions. *Biomolecules, 11*(2). https://doi.org/10.3390/biom11020271

Kong, D. Z., Lian, Y. H., Wang, L. J., Wang, C. M., Meng, Y. Y., & Zhou, H. W. (2019, Jun 6). Central nervous system vasculopathy caused by Fabry disease: a case report. *BMC Neurol, 19*(1), 115. https://doi.org/10.1186/s12883-019-1348-9

Kummer, K. K., Kalpachidou, T., Kress, M., & Langeslag, M. (2017). Signatures of Altered Gene Expression in Dorsal Root Ganglia of a Fabry Disease Mouse Model. *Front Mol Neurosci, 10*, 449. https://doi.org/10.3389/fnmol.2017.00449

Lakoma, J., Rimondini, R., Ferrer Montiel, A., Donadio, V., Liguori, R., & Caprini, M. (2016). Increased expression of Trpv1 in peripheral terminals mediates thermal nociception in Fabry disease mouse model. *Mol Pain, 12*. https://doi.org/10.1177/1744806916663729

Lee, K., Jin, X., Zhang, K., Copertino, L., Andrews, L., Baker-Malcolm, J., Geagan, L., Qiu, H., Seiger, K., Barngrover, D., McPherson, J. M., & Edmunds, T. (2003, Apr). A biochemical and pharmacological comparison of enzyme replacement therapies for the glycolipid storage disorder Fabry disease. *Glycobiology, 13*(4), 305-313. https://doi.org/10.1093/glycob/cwg034

Lim, T. K., Shi, X. Q., Johnson, J. M., Rone, M. B., Antel, J. P., David, S., & Zhang, J. (2015, Feb 25). Peripheral nerve injury induces persistent vascular dysfunction and endoneurial hypoxia, contributing to the genesis of neuropathic pain. *J Neurosci, 35*(8), 3346-3359. https://doi.org/10.1523/JNEUROSCI.4040-14.2015

Lin, J., Jiang, L., Guo, K., & Feng, N. (2023, Jan 2). Decreased VEGFA alleviates the symptoms of LPS-induced sepsis in a mouse model by inhibiting glycolysis and thereby regulating the polarization of macrophages. *Eur J Histochem, 67*(1). https://doi.org/10.4081/ejh.2023.3528

Lin, Q., Cong, X., & Yun, Z. (2011, Jun). Differential hypoxic regulation of hypoxia-inducible factors 1alpha and 2alpha. *Mol Cancer Res, 9*(6), 757-765. https://doi.org/10.1158/1541-7786.MCR-11-0053

Livak, K. J., & Schmittgen, T. D. (2001, Dec). Analysis of relative gene expression data using real-time quantitative PCR and the 2(-Delta Delta C(T)) Method. *Methods, 25*(4), 402-408. https://doi.org/10.1006/meth.2001.1262

Lorenzen, J. M., Dietrich, B., Fiedler, J., Jazbutyte, V., Fleissner, F., Karpinski, N., Weidemann, F., Wanner, C., Asan, E., Caprio, M., Ertl, G., Bauersachs, J., & Thum, T. (2013, Jan). Pathologic endothelial response and impaired function of circulating angiogenic cells in patients with Fabry disease. *Basic Res Cardiol, 108*(1), 311. https://doi.org/10.1007/s00395-012-0311-3

Marshall, J., Ashe, K. M., Bangari, D., McEachern, K., Chuang, W. L., Pacheco, J., Copeland, D. P., Desnick, R. J., Shayman, J. A., Scheule, R. K., & Cheng, S. H. (2010, Nov 24). Substrate reduction augments the efficacy of enzyme therapy in a mouse model of Fabry disease. *PLoS One, 5*(11), e15033. https://doi.org/10.1371/journal.pone.0015033

Maruyama, H., Taguchi, A., Nishikawa, Y., Guili, C., Mikame, M., Nameta, M., Yamaguchi, Y., Ueno, M., Imai, N., Ito, Y., Nakagawa, T., Narita, I., & Ishii, S. (2018, Aug). Medullary thick ascending limb impairment in the Gla(tm)Tg(CAG-A4GALT) Fabry model mice. *FASEB J, 32*(8), 4544-4559. https://doi.org/10.1096/fj.201701374R

Mauhin, W., Lidove, O., Masat, E., Mingozzi, F., Mariampillai, K., Ziza, J. M., & Benveniste, O. (2015). Innate and Adaptive Immune Response in Fabry Disease. *JIMD Rep, 22*, 1-10. https://doi.org/10.1007/8904_2014_371

Mehta, A., Beck, M., Eyskens, F., Feliciani, C., Kantola, I., Ramaswami, U., Rolfs, A., Rivera, A., Waldek, S., & Germain, D. P. (2010, Sep). Fabry disease: a review of current management strategies. *QJM, 103*(9), 641-659. https://doi.org/10.1093/qjmed/hcq117

Miller, J. J., Aoki, K., Mascari, C. A., Beltrame, A. K., Sokumbi, O., North, P. E., Tiemeyer, M., Kriegel, A. J., & Dahms, N. M. (2019, Jan). alpha-Galactosidase A-deficient rats accumulate glycosphingolipids and develop cardiorenal phenotypes of Fabry disease. *FASEB J, 33*(1), 418-429. https://doi.org/10.1096/fj.201800771R

Miller, J. J., Aoki, K., Moehring, F., Murphy, C. A., O'Hara, C. L., Tiemeyer, M., Stucky, C. L., & Dahms, N. M. (2018, Mar 22). Neuropathic pain in a Fabry disease rat model. *JCI Insight, 3*(6). https://doi.org/10.1172/jci.insight.99171

Mishra, V., Banerjee, A., Gandhi, A. B., Kaleem, I., Alexander, J., Hisbulla, M., Kannichamy, V., Valaiyaduppu Subas, S., & Hamid, P. (2020, Dec 14). Stroke and Fabry Disease: A Review of Literature. *Cureus, 12*(12), e12083. https://doi.org/10.7759/cureus.12083

Miyake, T., Nakamura, S., Zhao, M., So, K., Inoue, K., Numata, T., Takahashi, N., Shirakawa, H., Mori, Y., Nakagawa, T., & Kaneko, S. (2016, Sep 15). Cold sensitivity of TRPA1 is unveiled by the prolyl hydroxylation blockade-induced sensitization to ROS. *Nat Commun, 7*, 12840. https://doi.org/10.1038/ncomms12840

Mogil, J. S., Ritchie, J., Sotocinal, S. G., Smith, S. B., Croteau, S., Levitin, D. J., & Naumova, A. K. (2006, Dec 15). Screening for pain phenotypes: analysis of three congenic mouse strains on a battery of nine nociceptive assays. *Pain, 126*(1-3), 24-34. https://doi.org/10.1016/j.pain.2006.06.004

Mogil, J. S., Wilson, S. G., Bon, K., Lee, S. E., Chung, K., Raber, P., Pieper, J. O., Hain, H. S., Belknap, J. K., Hubert, L., Elmer, G. I., Chung, J. M., & Devor, M. (1999, Mar). Heritability of nociception I: responses of 11 inbred mouse strains on 12 measures of nociception. *Pain, 80*(1-2), 67-82. https://doi.org/10.1016/s0304-3959(98)00197-3

Monticelli, M., Liguori, L., Allocca, M., Bosso, A., Andreotti, G., Lukas, J., Monti, M. C., Morretta, E., Cubellis, M. V., & Hay Mele, B. (2022, May 4). Drug Repositioning for Fabry Disease: Acetylsalicylic Acid Potentiates the Stabilization of Lysosomal Alpha-Galactosidase by Pharmacological Chaperones. *Int J Mol Sci, 23*(9). https://doi.org/10.3390/ijms23095105

Namdar, M., Gebhard, C., Studiger, R., Shi, Y., Mocharla, P., Schmied, C., Brugada, P., Luscher, T. F., & Camici, G. G. (2012). Globotriaosylsphingosine accumulation and not alpha-galactosidase-A deficiency causes endothelial dysfunction in Fabry disease. *PLoS One, 7*(4), e36373. https://doi.org/10.1371/journal.pone.0036373

Namer, B., Orstavik, K., Schmidt, R., Mair, N., Kleggetveit, I. P., Zeidler, M., Martha, T., Jorum, E., Schmelz, M., Kalpachidou, T., Kress, M., & Langeslag, M. (2017). Changes in Ionic Conductance Signature of Nociceptive Neurons Underlying Fabry Disease Phenotype. *Front Neurol, 8*, 335. https://doi.org/10.3389/fneur.2017.00335

Oder, D., Muntze, J., & Nordbeck, P. (2021, Apr). Contemporary therapeutics and new drug developments for treatment of Fabry disease: a narrative review. *Cardiovasc Diagn Ther, 11*(2), 683-695. https://doi.org/10.21037/cdt-20-743

Ohshima, T., Murray, G. J., Swaim, W. D., Longenecker, G., Quirk, J. M., Cardarelli, C. O., Sugimoto, Y., Pastan, I., Gottesman, M. M., Brady, R. O., & Kulkarni, A. B. (1997, Mar 18). alpha-Galactosidase A deficient mice: a model of Fabry disease. *Proc Natl Acad Sci U S A, 94*(6), 2540-2544. https://doi.org/10.1073/pnas.94.6.2540

Paolicelli, R. C., Sierra, A., Stevens, B., Tremblay, M. E., Aguzzi, A., Ajami, B., Amit, I., Audinat, E., Bechmann, I., Bennett, M., Bennett, F., Bessis, A., Biber, K., Bilbo, S., Blurton-Jones, M., Boddeke, E., Brites, D., Brone, B., Brown, G. C., Butovsky, O., Carson, M. J., Castellano, B., Colonna, M., Cowley, S. A., Cunningham, C., Davalos, D., De Jager, P. L., de Strooper, B., Denes, A., Eggen, B. J. L., Eyo, U., Galea, E., Garel, S., Ginhoux, F., Glass, C. K., Gokce, O., Gomez-Nicola, D., Gonzalez, B., Gordon, S., Graeber, M. B., Greenhalgh, A. D., Gressens, P., Greter, M., Gutmann, D. H., Haass, C., Heneka, M. T., Heppner, F. L., Hong, S., Hume, D. A., Jung, S., Kettenmann, H., Kipnis, J., Koyama, R., Lemke, G., Lynch, M., Majewska, A., Malcangio, M., Malm, T., Mancuso, R., Masuda, T., Matteoli, M., McColl, B. W., Miron, V. E., Molofsky, A. V., Monje, M., Mracsko, E., Nadjar, A., Neher, J. J., Neniskyte, U., Neumann, H., Noda, M., Peng, B., Peri, F., Perry, V. H., Popovich, P. G., Pridans, C., Priller, J., Prinz, M., Ragozzino, D., Ransohoff, R. M., Salter, M. W., Schaefer, A., Schafer, D. P., Schwartz, M., Simons, M., Smith, C. J., Streit, W. J., Tay, T. L., Tsai, L. H., Verkhratsky, A., von Bernhardi, R., Wake, H., Wittamer, V., Wolf, S. A., Wu, L. J., & Wyss-Coray, T. (2022, Nov 2). Microglia states and nomenclature: A field at its crossroads. *Neuron, 110*(21), 3458-3483. https://doi.org/10.1016/j.neuron.2022.10.020

Parisi, L., Gini, E., Baci, D., Tremolati, M., Fanuli, M., Bassani, B., Farronato, G., Bruno, A., & Mortara, L. (2018). Macrophage Polarization in Chronic Inflammatory Diseases: Killers or Builders? *J Immunol Res, 2018*, 8917804. https://doi.org/10.1155/2018/8917804

Park, J. L., Shu, L., & Shayman, J. A. (2009, Apr). Differential involvement of COX1 and COX2 in the vasculopathy associated with the alpha-galactosidase A-knockout mouse. *Am J Physiol Heart Circ Physiol, 296*(4), H1133-1140. https://doi.org/10.1152/ajpheart.00929.2008

Park, J. L., Whitesall, S. E., D'Alecy, L. G., Shu, L., & Shayman, J. A. (2008, Oct). Vascular dysfunction in the alpha-galactosidase A-knockout mouse is an endothelial cell-, plasma membrane-based defect. *Clin Exp Pharmacol Physiol, 35*(10), 1156-1163. https://doi.org/10.1111/j.1440-1681.2008.04984.x

Politei, J. M., Bouhassira, D., Germain, D. P., Goizet, C., Guerrero-Sola, A., Hilz, M. J., Hutton, E. J., Karaa, A., Liguori, R., Üçeyler, N., Zeltzer, L. K., & Burlina, A. (2016, Jul). Pain in Fabry Disease: Practical Recommendations for Diagnosis and Treatment. *CNS Neurosci Ther, 22*(7), 568-576. https://doi.org/10.1111/cns.12542

Pollmann, S., Scharnetzki, D., Manikowski, D., Lenders, M., & Brand, E. (2021). Endothelial Dysfunction in Fabry Disease Is Related to Glycocalyx Degradation. *Front Immunol, 12*, 789142. https://doi.org/10.3389/fimmu.2021.789142

Qin, Y., Zhan, J. Q., Ma, C. J., Cao, C. Y., Zhang, Y., Min, Y. T., & Lv, Y. F. (2023, Jun). Generation and characterization of iPS cell line (CTGUi001-A) from skin fibroblasts of a patient with Fabry disease. *Stem Cell Res, 69*, 103063. https://doi.org/10.1016/j.scr.2023.103063

Rajan, J. N., Ireland, K., Johnson, R., & Stepien, K. M. (2021, Sep 15). Review of Mechanisms, Pharmacological Management, Psychosocial Implications, and Holistic Treatment of Pain in Fabry Disease. *J Clin Med, 10*(18). https://doi.org/10.3390/jcm10184168

Reiterer, M., Colaco, R., Emrouznejad, P., Jensen, A., Rundqvist, H., Johnson, R. S., & Branco, C. (2019, Jul 15). Acute and chronic hypoxia differentially predispose lungs for metastases. *Sci Rep, 9*(1), 10246. https://doi.org/10.1038/s41598-019-46763-y

Richards, S., Aziz, N., Bale, S., Bick, D., Das, S., Gastier-Foster, J., Grody, W. W., Hegde, M., Lyon, E., Spector, E., Voelkerding, K., Rehm, H. L., & Committee, A. L. Q. A. (2015, May). Standards and guidelines for the interpretation of sequence variants: a joint consensus recommendation of the American College of Medical Genetics and Genomics and the Association for Molecular Pathology. *Genet Med, 17*(5), 405-424. https://doi.org/10.1038/gim.2015.30

Rickert, V., Wagenhauser, L., Nordbeck, P., Wanner, C., Sommer, C., Rost, S., & Üçeyler, N. (2020, Nov). Stratification of Fabry mutations in clinical practice: a closer look at alpha-galactosidase A-3D structure. *J Intern Med, 288*(5), 593-604. https://doi.org/10.1111/joim.13125

Rozenfeld, P., & Feriozzi, S. (2017, Nov). Contribution of inflammatory pathways to Fabry disease pathogenesis. *Mol Genet Metab, 122*(3), 19-27. https://doi.org/10.1016/j.ymgme.2017.09.004

Saito, S., Ohno, K., & Sakuraba, H. (2011, Jun). Fabry-database.org: database of the clinical phenotypes, genotypes and mutant alpha-galactosidase A structures in Fabry disease. *J Hum Genet, 56*(6), 467-468. https://doi.org/10.1038/jhg.2011.31

Saxena, K., & Jolly, M. K. (2019, Aug 3). Acute vs. Chronic vs. Cyclic Hypoxia: Their Differential Dynamics, Molecular Mechanisms, and Effects on Tumor Progression. *Biomolecules, 9*(8). https://doi.org/10.3390/biom9080339

Schindelin, J., Arganda-Carreras, I., Frise, E., Kaynig, V., Longair, M., Pietzsch, T., Preibisch, S., Rueden, C., Saalfeld, S., Schmid, B., Tinevez, J. Y., White, D. J., Hartenstein, V., Eliceiri, K., Tomancak, P., & Cardona, A. (2012, Jun 28). Fiji: an open-source platform for biological-image analysis. *Nat Methods, 9*(7), 676-682. https://doi.org/10.1038/nmeth.2019

Schödel, J., & Ratcliffe, P. J. (2019, Oct). Mechanisms of hypoxia signalling: new implications for nephrology. *Nat Rev Nephrol, 15*(10), 641-659. https://doi.org/10.1038/s41581-019-0182-z

Shen, J. S., Meng, X. L., Schiffmann, R., Brady, R. O., & Kaneski, C. R. (2007, Sep-Oct). Establishment and characterization of Fabry disease endothelial cells with an extended lifespan. *Mol Genet Metab, 92*(1-2), 137-144. https://doi.org/10.1016/j.ymgme.2007.06.003

Shiozuka, C., Taguchi, A., Matsuda, J., Noguchi, Y., Kunieda, T., Uchio-Yamada, K., Yoshioka, H., Hamanaka, R., Yano, S., Yokoyama, S., Mannen, K., Kulkarni, A. B., Furukawa, K., & Ishii, S. (2011, Feb). Increased globotriaosylceramide levels in a transgenic mouse expressing human alpha1,4-galactosyltransferase and a mouse model for treating Fabry disease. *J Biochem, 149*(2), 161-170. https://doi.org/10.1093/jb/mvq125

Shu, L., & Shayman, J. A. (2007, Jul 20). Caveolin-associated accumulation of globotriaosylceramide in the vascular endothelium of alpha-galactosidase A null mice. *J Biol Chem, 282*(29), 20960-20967. https://doi.org/10.1074/jbc.M702436200

Simonetta, I., Tuttolomondo, A., Daidone, M., Miceli, S., & Pinto, A. (2020). Treatment of Anderson-Fabry Disease. *Curr Pharm Des, 26*(40), 5089-5099. https://doi.org/10.2174/1381612826666200317142412

Sorriento, D., & Iaccarino, G. (2019, Aug 9). Inflammation and Cardiovascular Diseases: The Most Recent Findings. *Int J Mol Sci, 20*(16). https://doi.org/10.3390/ijms20163879

Spitzel, M., Wagner, E., Breyer, M., Henniger, D., Bayin, M., Hofmann, L., Mauceri, D., Sommer, C., & Üçeyler, N. (2022, May 24). Dysregulation of Immune Response Mediators and Pain-Related Ion Channels Is Associated with Pain-like Behavior in the GLA KO Mouse Model of Fabry Disease. *Cells, 11*(11). https://doi.org/10.3390/cells11111730

Staal, R. G. W., Khayrullina, T., Zhang, H., Davis, S., Fallon, S. M., Cajina, M., Nattini, M. E., Hu, A., Zhou, H., Poda, S. B., Zorn, S., Chandrasena, G., Dale, E., Cambpell, B., Biilmann Ronn, L. C., Munro, G., & Mller, T. (2017, Jan 15). Inhibition of the potassium channel KCa3.1 by senicapoc reverses tactile allodynia in rats with peripheral nerve injury. *Eur J Pharmacol, 795*, 1-7. https://doi.org/10.1016/j.ejphar.2016.11.031

Taguchi, A., Ishii, S., Mikame, M., & Maruyama, H. (2023, Mar). Distinctive accumulation of globotriaosylceramide and globotriaosylsphingosine in a mouse model of classic Fabry disease. *Mol Genet Metab Rep, 34*, 100952. https://doi.org/10.1016/j.ymgmr.2022.100952

Taguchi, A., Maruyama, H., Nameta, M., Yamamoto, T., Matsuda, J., Kulkarni, A. B., Yoshioka, H., & Ishii, S. (2013, Dec 15). A symptomatic Fabry disease mouse model generated by inducing globotriaosylceramide synthesis. *Biochem J, 456*(3), 373-383. https://doi.org/10.1042/BJ20130825

Tapia, D., Floriolli, D., Han, E., Lee, G., Paganini-Hill, A., Wang, S., Zandihaghighi, S., Kimonis, V., & Fisher, M. (2021, Dec). Prevalence of cerebral small vessel disease in a Fabry disease cohort. *Mol Genet Metab Rep, 29*, 100815. https://doi.org/10.1016/j.ymgmr.2021.100815

Taylor, C. T., & Colgan, S. P. (2017, Dec). Regulation of immunity and inflammation by hypoxia in immunological niches. *Nat Rev Immunol, 17*(12), 774-785. https://doi.org/10.1038/nri.2017.103

Tran, H., Gupta, M., & Gupta, K. (2017, Nov 30). Targeting novel mechanisms of pain in sickle cell disease. *Blood, 130*(22), 2377-2385. https://doi.org/10.1182/blood-2017-05-782003

Tseng, W. L., Chou, S. J., Chiang, H. C., Wang, M. L., Chien, C. S., Chen, K. H., Leu, H. B., Wang, C. Y., Chang, Y. L., Liu, Y. Y., Jong, Y. J., Lin, S. Z., Chiou, S. H., Lin, S. J., & Yu, W. C. (2017, Mar 13). Imbalanced Production of Reactive Oxygen Species and Mitochondrial Antioxidant SOD2 in Fabry Disease-Specific Human Induced Pluripotent Stem Cell-Differentiated Vascular Endothelial Cells. *Cell Transplant, 26*(3), 513-527. https://doi.org/10.3727/096368916X694265

Tuttolomondo, A., Simonetta, I., Riolo, R., Todaro, F., Di Chiara, T., Miceli, S., & Pinto, A. (2021, Sep 18). Pathogenesis and Molecular Mechanisms of Anderson-Fabry Disease and Possible New Molecular Addressed Therapeutic Strategies. *Int J Mol Sci, 22*(18). https://doi.org/10.3390/ijms221810088

Üçeyler, N., Biko, L., Hose, D., Hofmann, L., & Sommer, C. (2016). Comprehensive and differential long-term characterization of the alpha-galactosidase A deficient mouse model of Fabry disease focusing on the sensory system and pain development. *Mol Pain, 12*. https://doi.org/10.1177/1744806916646379

Üçeyler, N., Ganendiran, S., Kramer, D., & Sommer, C. (2014, Oct). Characterization of pain in fabry disease. *Clin J Pain, 30*(10), 915-920. https://doi.org/10.1097/AJP.0000000000000041

Üçeyler, N., He, L., Schonfeld, D., Kahn, A. K., Reiners, K., Hilz, M. J., Breunig, F., & Sommer, C. (2011, Dec). Small fibers in Fabry disease: baseline and follow-up data under enzyme replacement therapy. *J Peripher Nerv Syst, 16*(4), 304-314. https://doi.org/10.1111/j.1529-8027.2011.00365.x

Üçeyler, N., Kahn, A. K., Kramer, D., Zeller, D., Casanova-Molla, J., Wanner, C., Weidemann, F., Katsarava, Z., & Sommer, C. (2013, May 24). Impaired small fiber conduction in patients with Fabry disease: a neurophysiological case-control study. *BMC Neurol, 13*, 47. https://doi.org/10.1186/1471-2377-13-47

Üçeyler, N., Urlaub, D., Mayer, C., Uehlein, S., Held, M., & Sommer, C. (2019, Jul). Tumor necrosis factor-alpha links heat and inflammation with Fabry pain. *Mol Genet Metab, 127*(3), 200-206. https://doi.org/10.1016/j.ymgme.2019.05.009

Waltz, T. B., Burand, A. J., Jr., Sadler, K. E., & Stucky, C. L. (2021, Aug-Dec). Sensory-specific peripheral nerve pathology in a rat model of Fabry disease. *Neurobiol Pain, 10*, 100074. https://doi.org/10.1016/j.ynpai.2021.100074

Wang, R., Jin, F., & Zhong, H. (2014). A novel experimental hypoxia chamber for cell culture. *Am J Cancer Res, 4*(1), 53-60. https://www.ncbi.nlm.nih.gov/pubmed/24482738

Weidemann, F., Jovanovic, A., Herrmann, K., & Vardarli, I. (2022, Feb 8). Chaperone Therapy in Fabry Disease. *Int J Mol Sci, 23*(3). https://doi.org/10.3390/ijms23031887

Weissmann, C., Albanese, A. A., Contreras, N. E., Gobetto, M. N., Castellanos, L. C. S., & Uchitel, O. D. (2021, Jan-Dec). Ion channels and pain in Fabry disease. *Mol Pain, 17*, 17448069211033172. https://doi.org/10.1177/17448069211033172

Xu, R., Li, C., Wu, Y., Shen, L., Ma, J., Qian, J., & Ge, J. (2017, Feb). Role of KCa3.1 Channels in Macrophage Polarization and Its Relevance in Atherosclerotic Plaque Instability. *Arterioscler Thromb Vasc Biol, 37*(2), 226-236. https://doi.org/10.1161/ATVBAHA.116.308461

Zhu, Y., Zhang, L., Wang, G., Zhao, J., Hou, X., Wu, H., Xu, Y., Mao, J., Liu, Z., & Zhang, J. (2021, Aug). Generation of an induced pluripotent stem cell line (ZJUi007-A) from a 11-year-old patient of Fabry disease. *Stem Cell Res, 55*, 102475. https://doi.org/10.1016/j.scr.2021.102475

8. Appendices

8.1 Technical equipment

accu-jet® pro pipette controller	Brand, Wertheim, Germany
Analog Vortex Mixer	VWR, Radnor, USA
Behavioral testing set-up	
Hargreaves setup & IR device	Ugo Basile Inc., Comerio, Italy
Touch Test™ Monofilaments	FMI GmbH, Seeheim-Ober Beerbach, Germany
Cameras/Detectors	
Axiocam 506 mono	Carl Zeiss, Oberkochen, Germany
DMC2900	Leica Microsystems, Wetzlar, Germany
Cell culture consumables	
Cellstar Tissue Culture Dishes 35 x 10 mm	Greiner Bio One, Frickenhausen, Germany
Cellstar Tubes 15 ml, 50 ml	Greiner Bio One, Frickenhausen, Germany
Nunclon™ Delta Surface 4-Well plates	Greiner Bio One, Frickenhausen, Germany
Poly-D-Lysine/Laminin 12 mm round coverslips	Corning, Inc., Corning, NY, USA
Centrifuges	
Rotina 420R	Hettich, Tuttlingen, Germany
Eppendorf Centrifuge 4517R	Eppendorf, Hamburg, Germany
Coverslips 0.13-0.16 thickness 18 x 18 mm 24 x 40 mm 24 x 50 mm 24 x 32 mm	R. Langenbrinck, Emmendingen, Germany
Cryoboxes (with divider) 130 x 130 x 45 mm	GLW® Storing Systems, Würzburg, Germany

Cryostat CM3050 S	Leica, Wetzlar, Germany
Excitation light sources for microscopy	
Colibri 7 LED	Zeiss, Oberkochen, Germany
Freezer comfort -20°C	Liebherr, Biberach, Germany
Freezer TSX Series -80°C	Thermo Fisher Scientific, Waltham, MA, USA
Gas-tight adhesive tape	DIOP, Rosbach, Germany
Gelaire® BSB4A laminar flow hood	Flow Laboratories, Meckenheim, Germany
Hamilton Syringe #1710 100 µl	Hamilton Co., Reno, NV, USA
HERAcell™ VIOS 150i	Thermo Fisher Scientific, Waltham, MA, USA
CO_2 incubator	
Homogenizer Polytron PT 1600	Kinematika AG, Luzern, Switzerland
MicroAmp® Fast 96-well	Applied Biosystems, Darmstadt, Germany
Reaction Plate (0.1 ml)	
MicroAmp® Optical Adhesive Film	Applied Biosystems, Darmstadt, Germany
Microscopes	
Apotome 2	Zeiss, Oberkochen, Germany
Axio Imager M.2	Zeiss, Oberkochen, Germany
DMi8	Leica Microsystems, Wetzlar, Germany
DMI IL LED	Leica Microsystems, Wetzlar, Germany
Microscope slides 76 x 26 mm	R. Langenbrinck, Emmendingen, Germany
Micro tube 1.5 & 2 ml	Sarstedt, Nümbrecht, Germany
Micro tube „Schraubröhre“ 2 ml	Sarstedt, Nümbrecht, Germany
Micro scale ALS 120-4	KERN & Sohn,
NanoDrop™ One	Thermo Fisher Scientific, Waltham, MA, USA
Parafilm “M” Laboratory Film	Bemis Company, Inc., Neenah, WI, USA
PCR Tubes 0.2 ml	Eppendorf, Hamburg, Germany
Pipettes Research® plus	Eppendorf, Hamburg, Germany
1 µl, 2 µl, 10 µl, 20 µl, 100µl,	
200 µl, 1000 µl	
Pipette tips	Sarstedt, Nümbrecht, Germany
10 µl, 20 µl, 100 µl, 200 µl,	
1000 µl	

Software	
GraphPad Prism 9	GraphPad Software, San Diego, CA, USA
Image J 2.1.0/1.53c	Wayne Rasband, National Institutes of Health, USA
LAS X V4.12	Leica Microsystems, Wetzlar, Germany
Office 2019	Microsoft, Redmond, WA, USA
SPSS IBM Version 29	IBM, Ehningen, Germany
StepOne Plus Software v2.3	Thermo Fisher Scientific, Waltham, MA, USA
ZEN2 Blue Edition	Zeiss, Oberkochen, Germany
Specimen bags 70 x 100 mm	A. Hartenstein, Würzburg, Germany
Sterican® Needle 30G x 1/2" / Ø 0,30 x 12 mm, yellow	B.Braun, Melsungen, Germany
SuperFrost™ Plus microscope slides 25 x 75 x 1.0 mm	VWR International bvba, Leuven, Belgium
Super PAP Pen Liquid Blocker NEU	Science Services, Munich, Germany
Surgical cutlery	
Blades	B.Braun, Melsungen, Germany
Dumont #5 Fine Forceps	FST, Heidelberg, Germany
Extra Fine Bonn Scissors	FST, Heidelberg, Germany
Mouse Brain Slicer	Zivic Instruments, Pittsburgh, PA, USA
Narrow Pattern Forceps	FST, Heidelberg, Germany
Spatula	FST, Heidelberg, Germany
Vannas Spring Scissors 2 mm	FST, Heidelberg, Germany
Wagner Bone Scissors 30 mm	FST, Heidelberg, Germany
Thermocycler	
peqSTAR 2X	Peqlab, Erlangen, Germany
peqSTAR	Peqlab, Erlangen, Germany
StepOne Plus	Applied Biosystems, Darmstadt, Germany
Thermo shaker PCMT Grant Bio HC24N 24 x 1.5 ml	Grant Instruments Ltd., Cambridgeshire, UK
Tissue-Tek® cryomolds	Sakura, Staufen, Germany

10x10x5 mm
15x15x5 mm
25x20x5 mm

Water bath	Memmert, Büchenbach, Germany

8.1.1 Customized technical equipment

Manufactured by the scientific workshop of the University Hospital Würzburg, Department of Neurology:

Acrylic glass boxes (100 x 100 x 80 mm) for behavioral testing (see Fig. 3 in section 4.9.1 and Fig. 4 in section 4.9.2)
Hypoxia chamber of acrylic glass (300 x 200 x 160 mm) with valves customized according to (Wang et al., 2014) (see Fig. 2 in section 4.4)
Wire mesh set up for von Frey testing (see Fig. 3 in section 4.9.1)

Self-customized equipment:

Catheter for i.v. ERT administration (Fig. 26)

BD Micro-Fine Ultra™ Pen-Needle 0.33 mm (29G) x 12.7 mm	BD Medical, Heidelberg, Germany
Polyethylene tube SX03	A. Hartenstein, Würzburg, Germany
SHRINK-KON® Heat shrink tubing HSB46	ABB, Zürich, Switzerland
Hot air gun	LUX Tools, Wermelskirchen, Germany

A Pen-Needle was carefully removed out of the surrounding plastic cover and inserted into a 50 mm long piece of polyethylene (PE) tube. Needle and PE tube were fused together with a 10 mm long piece of shrinking tube fixed via using a hot air gun.

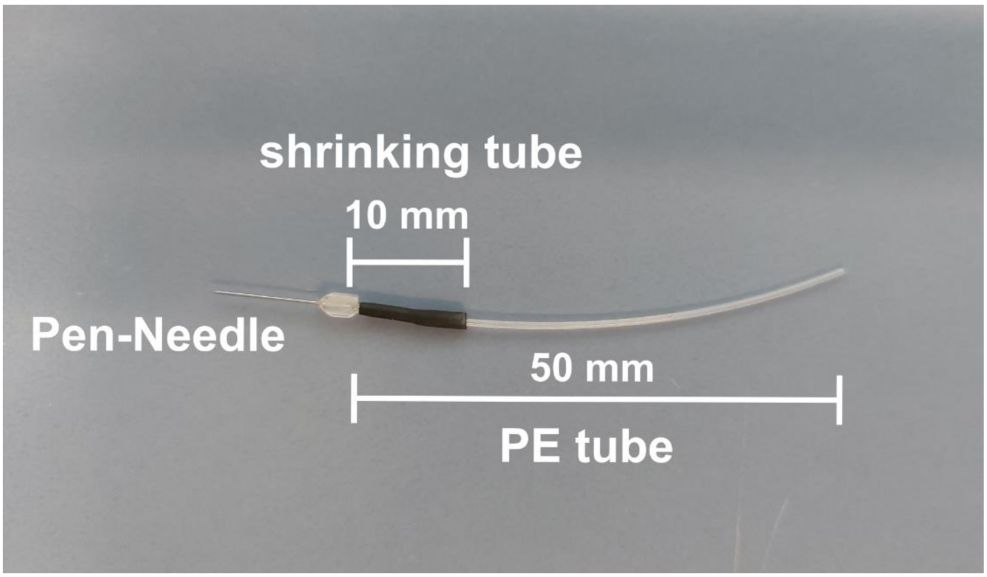

Figure 26: Self-customized catheter for i.v. ERT administration.
A pen-needle with attached PE tube (50 mm length) and fixed with a shrinking tube (10 mm length) using a hot air gun. Abbreviations: mm: millimeter; PE: polyethylene.

8.2 Reagents

2-Methylbutane	Carl Roth, Karlsruhe, Germany
Agalsidase-β	Genzyme, Cambridge, MA, USA
Aqua ad iniectabilia 10 ml	B.Braun, Melsungen, Germany
Aqua-Poly/Mount	Polysciences, Warrington, PA, USA
Avidin/Biotin blocking kit	Vector Laboratories, Burlingame, CA, USA
BSA	Sigma-Aldrich, St. Louis, MS, USA
Capsaicin	Sigma-Aldrich, St. Louis, MS, USA
CoverGrip™ coverslip sealant	Biotium, Fremont, CA, USA
DAB substrate kit, peroxidase (with nickel)	Vector Laboratories, Burlingame, CA, USA
DEPC	Sigma-Aldrich, St. Louis, MS, USA
DMSO	Carl Roth, Karlsruhe, Germany
DRG medium	
DMEM/F-12 (1:1) (1x) + GlutaMAX™	Thermo Fisher Scientific, Waltham, MA, USA
FBS	Merch, Darmstadt, Germany
Penicillin/Streptomycin	Thermo Fisher Scientific, Waltham, MA, USA
Dulbecco's Phosphate Buffer Saline	Sigma-Aldrich, St. Louis, MS, USA
Ethanol	Sigma-Aldrich, St. Louis, MS, USA

Hematoxylin-eosin	Sigma-Aldrich, St. Louis, MS, USA
Isoflurane CP® 1ml/ml	CP Pharma, Burgdorf, Germany
Isotonic sodium chloride NaCl 0,9%	Fresenius Kabi, Bad Homburg, Germany
Liberase TH Research Grade	Roche, Basel, Switzerland
Liberase TM Research Grade	Roche, Basel, Switzerland
Milk powder	Sigma-Aldrich, St. Louis, MO, USA
Native mouse nerve growth factor (NGF) 2.5S protein 99% (10 µg/ml)	Alomone Labs, Jerusalem, Israel
Nuclease free water	Qiagen, Hilden, Germany
Nucleic acid extraction kits	
DNeasy® Blood & Tissue kit (250)	Qiagen, Hilden, Germany
miRNeasy® mini Kit (50)	Qiagen, Hilden, Germany
O_2 21% normoxia gas mixture (21% O_2, 5% CO_2, 74% N_2 [v/v])	Rießner Gase GmbH, Lichtenfels, Germany
O_2 2% hypoxia gas mixture (2% O_2, 5% CO_2, 93% N_2 [v/v])	Rießner Gase GmbH, Lichtenfels, Germany
PBS	Sigma-Aldrich, St. Louis, MO, USA
PFA	Merck Millipore, Darmstadt, Germany
(qRT)-PCR reagents	
Primers (see section 8.3)	Invitrogen, Carlsbad, CA, USA
TaqMan™ Fast Advanced Master Mix	Thermo Fisher Scientific, Waltham, MA, USA
TaqMan™ Probes (see section 8.5)	Thermo Fisher Scientific, Waltham, MA, USA
10x PCR Buffer II	Thermo Fisher Scientific, Waltham, MA, USA
$MgCl_2$ solution	Thermo Fisher Scientific, Waltham, MA, USA
dNTP Mix 10mM	Thermo Fisher Scientific, Waltham, MA, USA
Oligo$(dT)_{16}$ 50µM	Invitrogen, Carlsbad, CA, USA
Random Hexamer 50 µM	Invitrogen, Carlsbad, CA, USA
RNase Inhibitor 2000 U, 20 U/µl	Thermo Fisher Scientific, Waltham, MA, USA
MultiScribe Reverse Transcriptase 50 U/µl	Thermo Fisher Scientific, Waltham, MA, USA

Saponin	Sigma-Aldrich, St. Louis, MS, USA
Sekusept™ PLUS	Ecolab Inc., St. Paul, MN, USA
StxB	Sigma-Aldrich, St. Louis, MS, USA
Tissue-Tek® O.C.T.™ Compound	Sakura Finetek, Tokyo, Japan
Triton™ X-100	Sigma-Aldrich, St. Louis, MS, USA
VECTASHIELD Antifade Mounting Medium (with DAPI)	Vector Laboratories, Newark, CA, USA
Vitro-Clud®	R. Langenbrinck, Teningen, Germany
Xylole	Carl Roth, Karlsruhe, Germany

8.3 Primer sequences for murine genotyping

Table 1: Primer sequences for murine genotyping of WT, heterozygous, and GLA KO mice.

Genotype	Sequence (5' → 3')	Catalog#	Company
WT	5`GCCAGAGGCCACTTGTGTAG3`	oIMR7415	Invitrogen,
Heterozygous	5`GCAAGTTGCCCTCTGACTTC3`	oIMR5948	Carslbad,
GLA KO	5`AGGTCCACAGCAAAGGATTG3`	oIMR5947	CA, USA

8.4 qRT PCR arrays

Table 2: qRT PCR arrays target gene screening.

Array targets	Catalog#	Company
TaqMan® Array Mouse Immune Response	4414079	Thermo Fisher Scientific, Waltham, MA, USA
RT² Profiler PCR Array, Mouse Hypoxia Signaling Pathway	PAMM-032ZA	Qiagen, Hilden, Germany

8.5 qRT PCR probes

Table 3: TaqMan™ probes.

Target gene	Target protein	Assay ID
Bcl2	apoptosis regulator Bcl 2	Mm00477631_m1
BNIP3	BCL2 interacting protein 3	Mm01275600_g1
C3	complement 3	Mm01232779_m1
CA9	carbonic anhydrase 9	Mm01349478_m1
CASP3	caspase 3	Mm01195085_m1
CCL2	C-C motif chemokine 2	Mm00441242_m1
CCL5	C-C motif chemokine 5	Mm01302427_m1
CD28	cluster of differentiation 28	Mm01253994_m1
CD4	cluster of differentiation 4	Mm00442754_m1
CD40	cluster of differentiation 40	Mm00441891_m1
CD40lg	cluster of differentiation 40 ligand	Mm00441911_m1
CD68	cluster of differentiation 68	Mm03047343_m1
CD80	cluster of differentiation 80	Mm00711660_m1
DDIT4	DNA damage inducible factor 4	Mm00512504_g1
EGLN3	Egl-9 family hypoxia inducible factor 3	Mm00472200_m1
EPO	erythropoietin	Mm00433126_m1
FOS	FBJ osteosarcoma oncogene	Mm00487425_m1
GFAP	glial fibrillary acidic protein	Mm01253033_m1
HIF1α	hypoxia inducible factor 1 alpha	Mm00468869_m1
HK2	hexokinase 2	Mm00443385_m1
HMOX1	heme oxygenase 1	Mm00516005_m1
ICAM1	intercellular adhesion molecule 1	Mm00516023_m1
IKBKB	inhibitor of nuclear factor kappa-B kinase subunit beta	Mm01222247_m1
IL-1β	interleukin-1beta	Mm00434228_m1
IL4	interleukin 4	Mm00445259_m1
IL6	interleukin 6	Mm00446190_m1
IL10	interleukin 10	Mm01288386_m1
LDHA	lactate dehydrogenase A	Mm01612132_g1

LGALS3	lectin galactose binding soluble 3	Mm00802901_m1
LRG1	leucine-rich alpha-2-glycoprotein 1	Mm01278767_m1
MMP2	matrix metalloproteinase 2	Mm00439498_m1
MMP3	matrix metalloproteinase 3	Mm00440295_m1
MMP9	matrix metalloproteinase 9	Mm00442991_m1
NFATC3	nuclear factor of activated T-cells, cytoplasmic 3	Mm01249200_m1
NLRP3	NACHT, LRR, and PYD domain-containing protein 3	Mm00840904_m1
PDK1	phosphoinositide-dependent kinase 1	Mm0054300_m1
RPL13a (endogenous control)	ribosomal protein L13a	Mm01612986_gH
SLC2A1 (GLUT1)	solute carrier family 2 (glucose transporter 1)	Mm00441480_m1
STAT3	signal transducer and activator of transcription 3	Mm01219775_m1
TFRC	transferrin receptor	Mm00441941_m1
TGF1β	transforming growth factor 1 beta	Mm01178820_m1
TNFα	tumor necrosis factor alpha	Mm00443258_m1
VEGFα	vascular endothelial growth factor A	Mm00437306_m1

8.6 Antibodies for ICC/IHC

Table 4: Primary antibodies for murine samples.

Reactivity	**Host**	**Company**	**Catalog #**	**Dilution**
β3 Tubulin	Rat	Santa Cruz	sc-80005	1:100
CA9	Rabbit	Invitrogen	PA1-16592	1:100
CD3	Rat	Bio-Rad	MCA1477	1:100
CD11b	Rat	Bio-Rad	MCA711	1:250
CD31	Rat	Bio-Rad	MCA2388	1:100
CD80	Goat	R&D Systems	AF740	1:50
CD206	Rat	Bio-Rad	MCA2235	1:100

F4/80	Rat	Bio-Rad	MCA497	1:300
HIF1α	Goat	R&D Systems	AF1935	1:100
PGP9.5	Guinea Pig	Sigma-Aldrich	AB5898	1:100
PGP9.5	Rabbit	Zytomed Systems	516-3344	1:100
PRPH	Rabbit	Sigma-Aldrich	AB1530	1:100
STxB ::	---	Sigma-Aldrich/	SML0562/	coupled
Alexa Fluor® 555	---	Jena Bioscience	APC-003	1:5000

Table 5: Secondary antibodies for murine samples.

Reactivity	**Host**	**Company**	**Catalog #**	**Dilution**
DAPI	---	Sigma-Aldrich	32670 UV	1:10 000
Goat-IgG	Donkey	Jackson Immunoresearch	705-165-147 Cy3	1:400
Guinea Pig-IgG	Donkey	Jackson Immunoresearch	706-546-148 AF®488	1:400
Rabbit-IgG	Donkey	Jackson Immunoresearch	711-605-152 AF®647	1:400
Rat-IgG	Donkey	Jackson Immunoresearch	712-165-150 Cy3	1:400
Rat-IgG	Goat	Jackson Immunoresearch	112-165-167 Cy3	1:400
Rat-IgG Mouse-absorbed	Rabbit	Vector Laboratories	BA-4001 biotinylated	1:50

8.7 Media for cultivation

DRG medium

Medium / Supplement	**Final concentration**
DMEM/F-12 (1:1) (1x) + GlutaMAX™	89%
FBS	10%
Pen/Strep	1%
NGF	100 ng/ml

8.8 Buffers and solutions

Buffer/Solution	**Final concentration**
DEPC-H_2O	0.01% DEPC Dissolved in distilled water Autoclaved
PBS (1x)	137 mM NaCl 2.7 mM KCl 1.5 mM KH_2PO_4 8.1 mM Na_2PO_4 pH 7.4

8.9 cDNA reverse transcription and duplex qRT PCR protocols

8.9.1 cDNA reverse transcription protocol for whole murine DRG tissue

Table 6: TaqMan™ Reverse Transcription Reagents mixture and cycler protocol for whole murine DRG tissue.

TaqMan™ reagents	**Mastermix per probe [µl]**
10x Buffer II	10
$MgCl_2$ solution	22
dNTP Mix	20
Random hexamer	5
RNase Inhibitor	2
Multiscribe Reverse Transcriptase	6.2
TOTAL	**65.2**

34.8 µl RNA-nuclease-free-H_2O-mixture containing 250 ng RNA per probe was added to the TaqMan™ Reverse Transcription Reagents mixture and run at following cycling conditions:

Temperature [°C]	Time [min]
25°C	10 min
37°C	60 min
95°C	5 min

8.9.2 cDNA reverse transcription protocol for murine DRG neuronal cell culture

32.5 µl RNA-nuclease-free-H_2O-mixture containing 250 ng RNA per probe was mixed with 5 µl Random Hexamer and was incubated for 3 min at 85°C in a cycler. To the RNA-nuclease-free-H_2O-Random-Hexamer-mixture 62.2 µl of the following mastermix was added per probe and run at following conditions.

Table 7: TaqMan™ Reverse Transcription Reagents mixture and cycler protocol for murine DRG neuronal cell culture.

TaqMan™ reagents	Mastermix per probe [µl]
10x Buffer II	10
$MgCl_2$ solution	22
dNTP Mix	20
RNase Inhibitor	2
Multiscribe Reverse Transcriptase	6.2
Oligo$(dT)_{16}$	2
TOTAL	**62.2**

Temperature [°C]	Time [min]
25°C	10 min
48°C	60 min
95°C	5 min

8.10 Behavioral data after 0.2 and 1 µg capsaicin/10 µl NaCl administration and after 10 µl NaCl administration

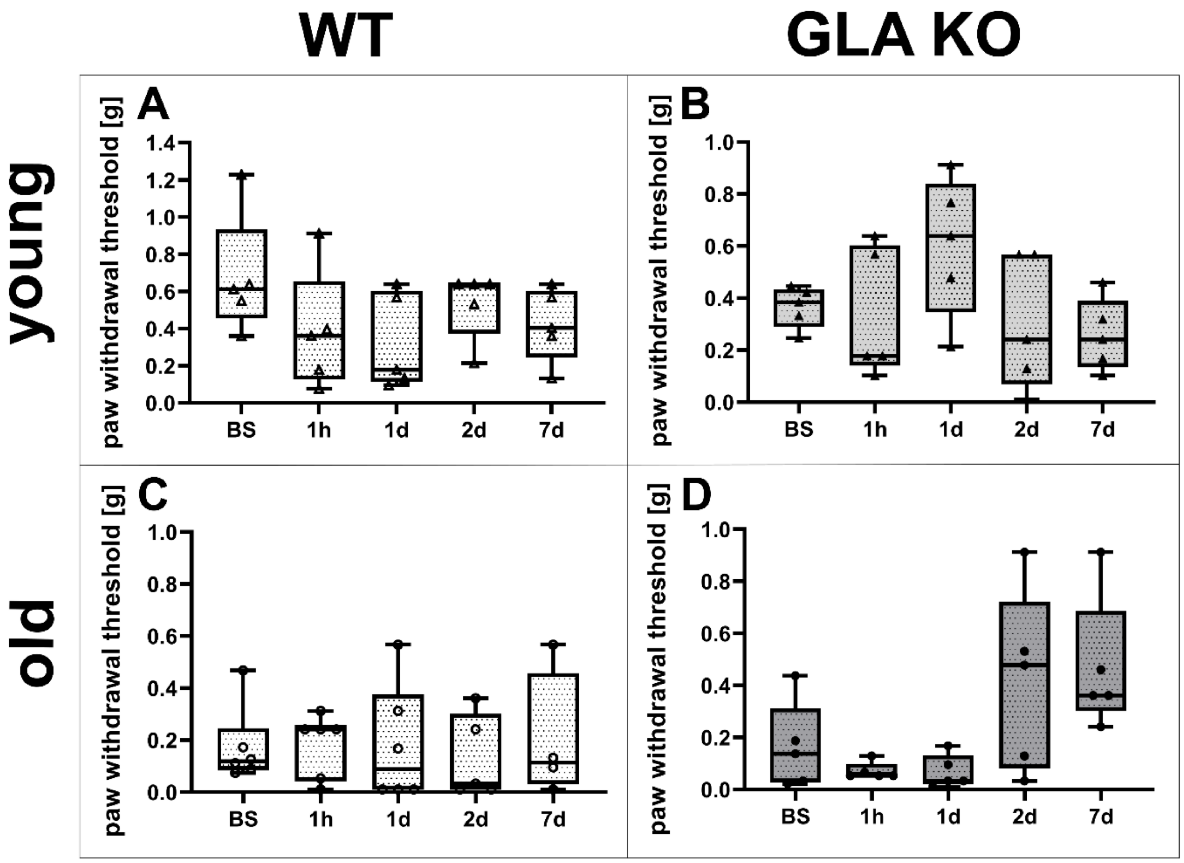

Figure 27: Assessment of the behavioral profile before (at baseline, BS) and after i.pl. 0.2 µg capsaicin/10 µl NaCl administration of young and old WT and GLA KO mice in the von Frey testing.
(A-D) Paw withdrawal thresholds after mechanical stimulation with von Frey filaments of young and old WT and GLA KO mice before and after i.pl. capsaicin administration at different time points (1h, 1d, 2d, and 7d post-Capsaicin). Abbreviations: BS: baseline; d: days; g: gram; GLA KO: alpha-galactosidase A knockout; h: hour; i.pl.: intraplantar; NaCl: sodium chloride; WT: wild type.

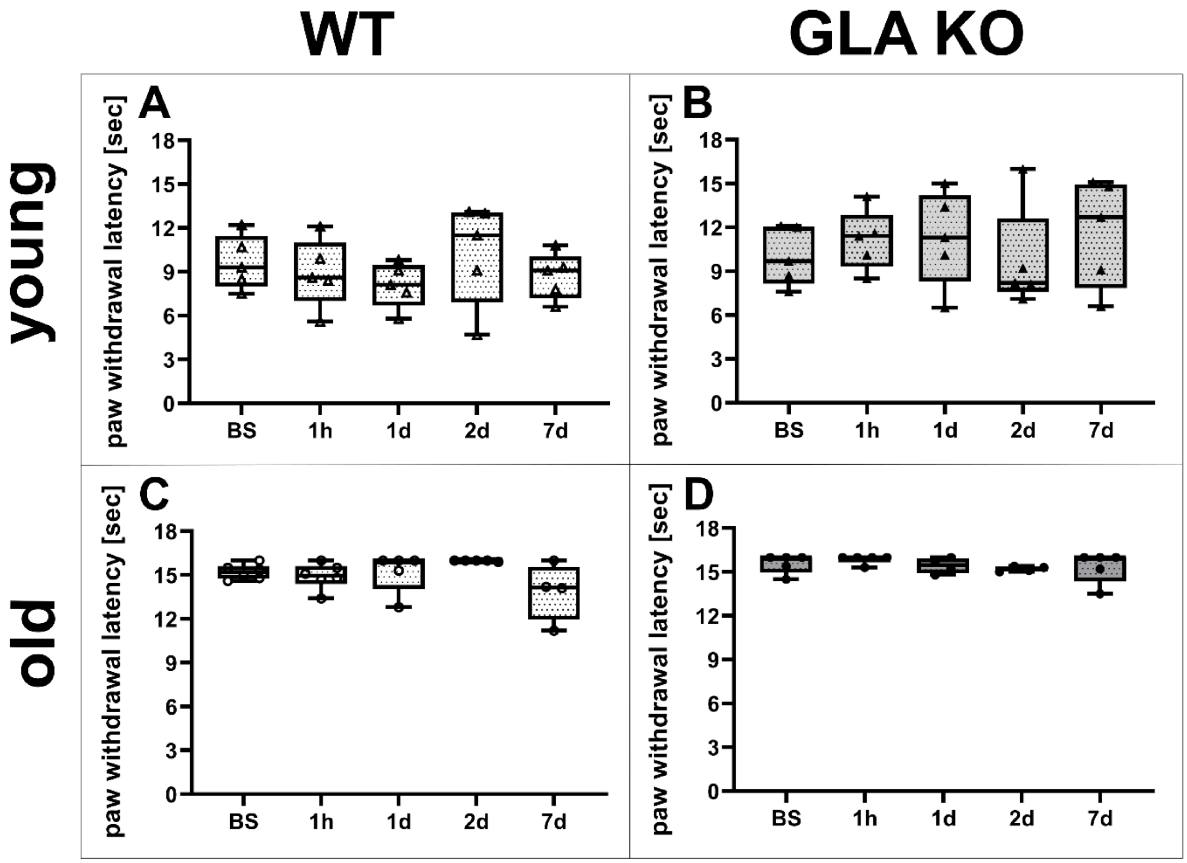

Figure 28: Assessment of the behavioral profile before (at baseline, BS) and after i.pl. 0.2 µg capsaicin/10 µl NaCl administration of young and old WT and GLA KO mice in the Hargreaves testing.
(A-D) Paw withdrawal latencies after heat stimulation of young and old WT and GLA KO mice before and after i.pl. capsaicin administration at different time points (1h, 1d, 2d, and 7d post-Capsaicin). Abbreviations: BS: baseline; d: days; GLA KO: alpha-galactosidase A knockout; h: hour; i.pl.: intraplantar; NaCl: sodium chloride; sec: seconds; WT: wild type.

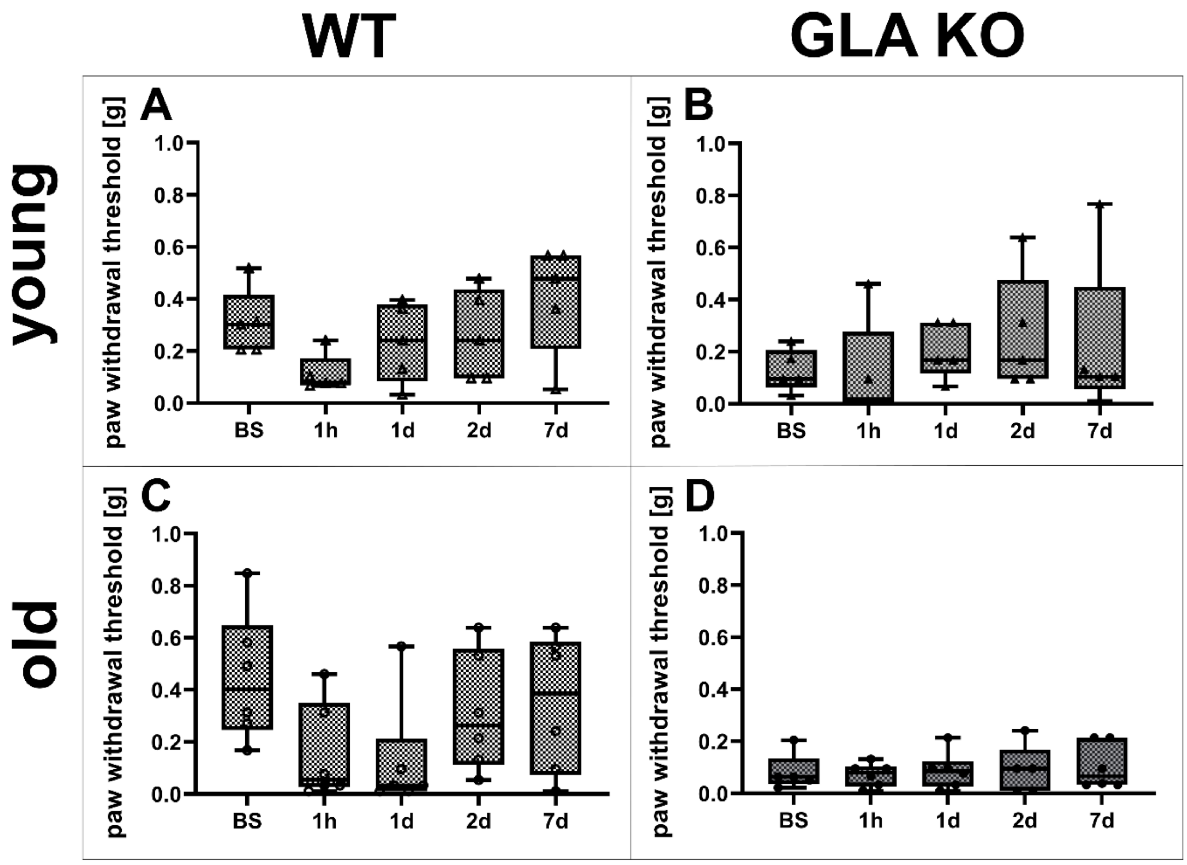

Figure 29: Assessment of the behavioral profile before (at baseline, BS) and after i.pl. 1 µg capsaicin/10 µl NaCl administration of young and old WT and GLA KO mice in the von Frey testing.
(A-D) Paw withdrawal thresholds after mechanical stimulation with von Frey filaments of young and old WT and GLA KO mice before and after i.pl. capsaicin administration at different time points (1h, 1d, 2d, and 7d post-Capsaicin). Abbreviations: BS: baseline; d: days; g: gram; GLA KO: alpha-galactosidase A knockout; h: hour; i.pl.: intraplantar; NaCl: sodium chloride; WT: wild type.

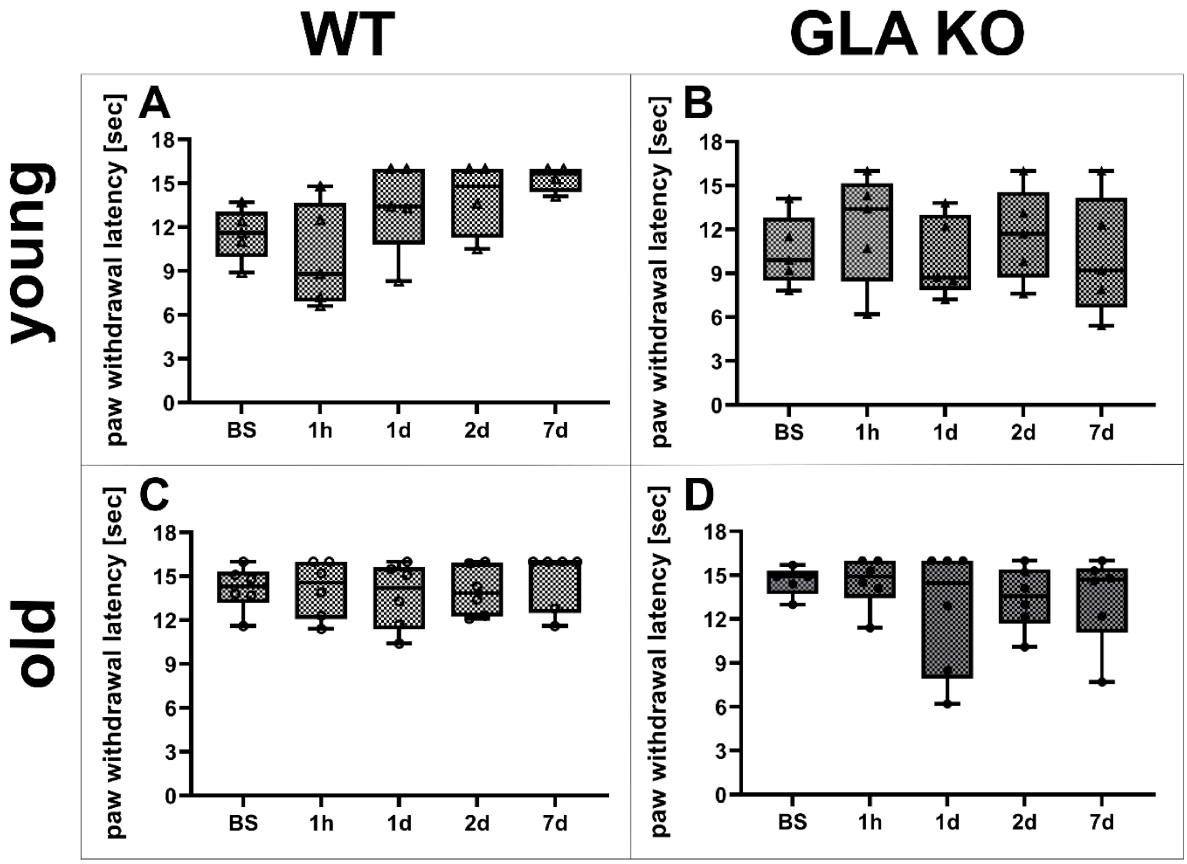

Figure 30: Assessment of the behavioral profile before (at baseline, BS) and after i.pl. 1 µg capsaicin/10 µl NaCl administration of young and old WT and GLA KO mice in the Hargreaves testing.
(A-D) Paw withdrawal latencies after heat stimulation of young and old WT and GLA KO mice before and after i.pl. capsaicin administration at different time points (1h, 1d, 2d, and 7d post-Capsaicin). Abbreviations: BS: baseline; d: days; GLA KO: alpha-galactosidase A knockout; h: hour; i.pl.: intraplantar; NaCl: sodium chloride; sec: seconds; WT: wild type.

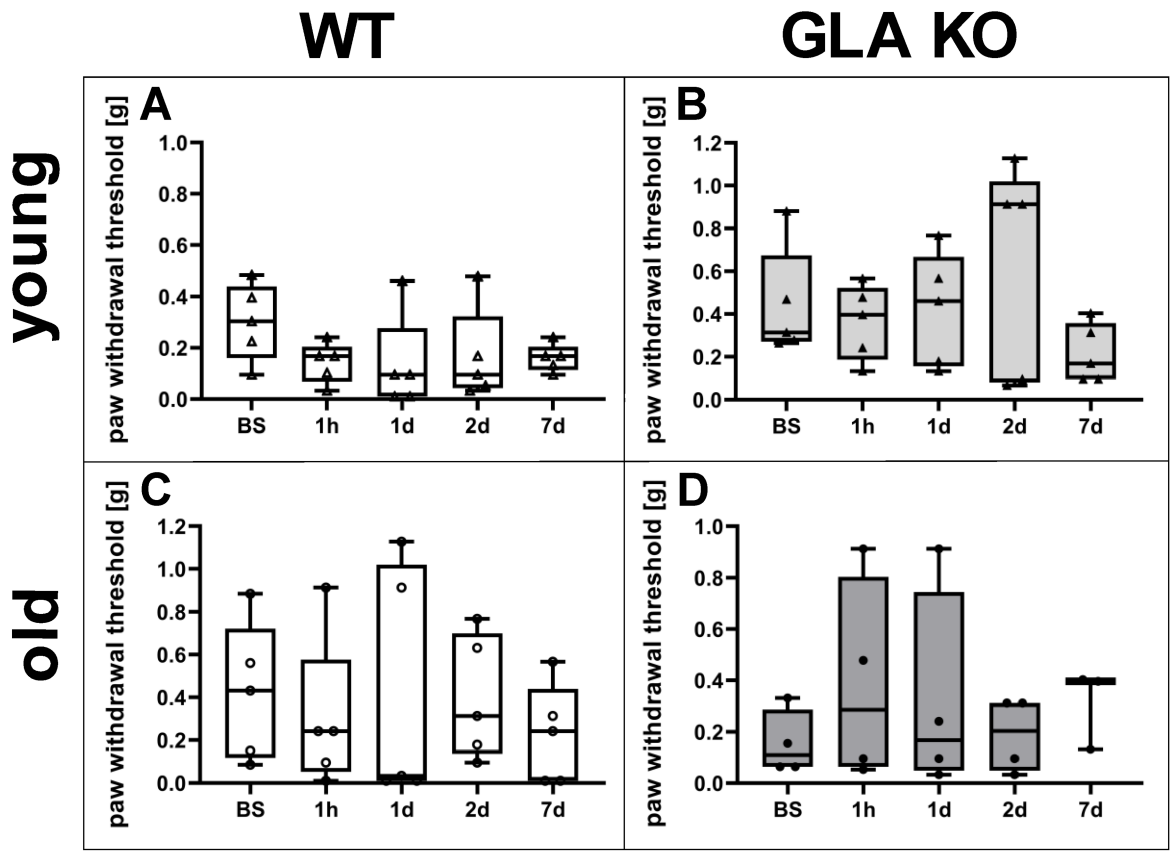

Figure 31: Assessment of the behavioral profile before (at baseline, BS) and after i.pl. 10 µl NaCl administration of young and old WT and GLA KO mice in the von Frey testing.
(A-D) Paw withdrawal thresholds after mechanical stimulation with von Frey filaments of young and old WT and GLA KO mice before and after i.pl. NaCl administration at different time points (1h, 1d, 2d, and 7d post-Capsaicin). Abbreviations: BS: baseline; d: days; g: gram; GLA KO: alpha-galactosidase A knockout; h: hour; i.pl.: intraplantar; NaCl: sodium chloride; WT: wild type.

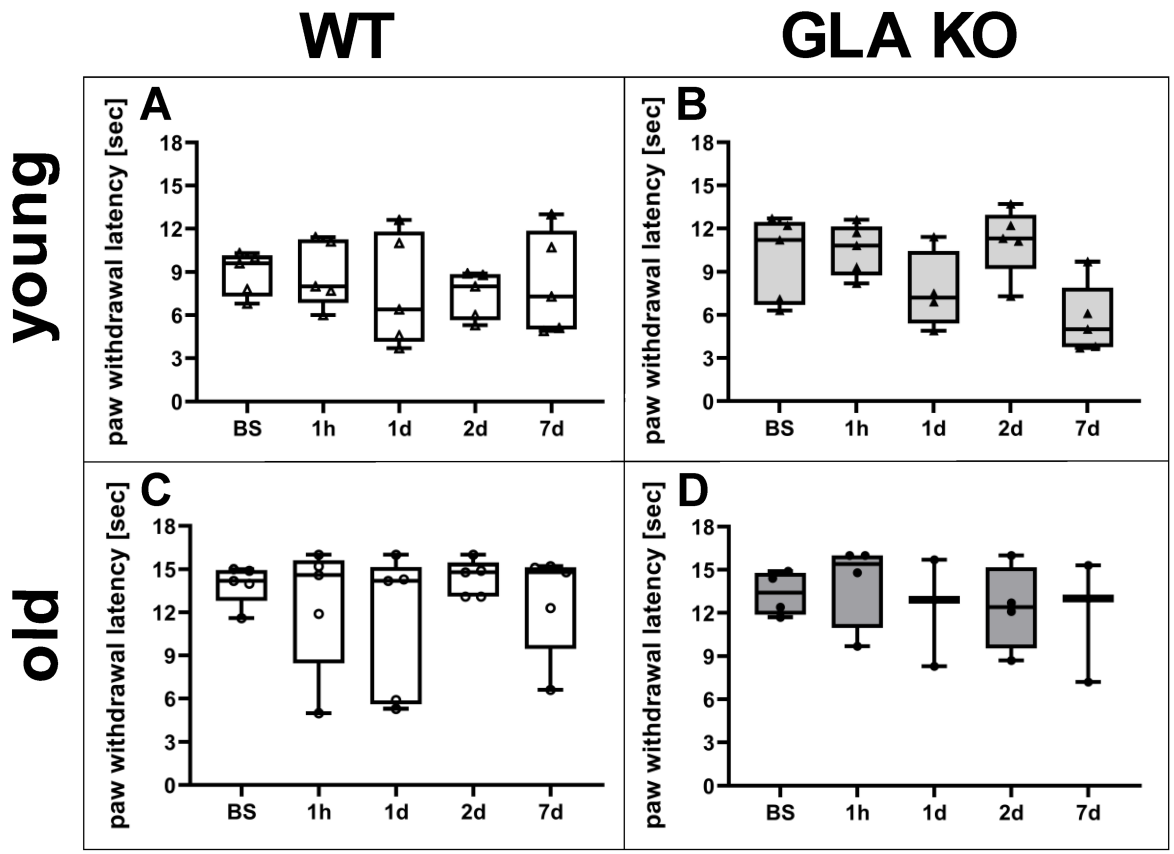

Figure 32: Assessment of the behavioral profile before (at baseline, BS) and after i.pl. 10 µl NaCl administration of young and old WT and GLA KO mice in the Hargreaves testing.
(A-D) Paw withdrawal latencies after heat stimulation of young and old WT and GLA KO mice before and after i.pl. capsaicin administration at different time points (1h, 1d, 2d, and 7d post-Capsaicin). Abbreviations: BS: baseline; d: days; GLA KO: alpha-galactosidase A knockout; h: hour; i.pl.: intraplantar; NaCl: sodium chloride; sec: seconds; WT: wild type.

9. Abbreviation

3D	three-dimensional
°C	degree Celsius
%	percent
(ΔΔ)Ct	(delta-delta) cycle threshold
µg	microgram
µl	microliter
µm	micrometer
µM	micromolar
AF®	Alexa Fluor®
ASIC	acid-sensing ion channel
BS	baseline
BSA/PBS	bovine serum albumin/phosphate-buffered saline
BSA/Tris	bovine serum albumin/tris-hydroxymethyl-aminomethane
BW	body weight
C3	complement 3
CA9	carbonic anhydrase 9
CaV	voltage-gated calcium channel
CBRA	cell body-rich area
CCL2/5	C-C motif chemokine 2/5
CD	cluster of differentiation
cDNA	complementary deoxyribonucleic acid
CNS	central nervous system
COX1/2	cyclooxygenase 1/2
CO_2	carbon dioxide
Ct value	cycle threshold value
CXCL10	C-X-C motif chemokine ligand 10
Cy3	Cyanine 3
d	days
DAB	3,3'-diaminobenzidine
DAPI	4',6-diamidino-2-phenylindole
DDIT4	DNA damage inducible factor 4
DNA	desoxyribonucleic acid
DRG	dorsal root ganglion

ERT	enzyme replacement therapy
E.W.	Elise Wagner, Cand. med.
F1 offspring	filial 1 offspring
F2 offspring	filial 2 offspring
F4/80	pan-macrophages marker
FAM™-MGB	fluorescein amidite-minor groove binder
FCS	fetal calf serum
FD	Fabry disease
FOS	proto-oncogene cFOS
g	gram
Gb3	globotriaosylceramide
GFAP	glial fibrillary acidic protein
GLA	alpha-galactosidase A
h	hour
H	height
H_2O_2	hydrogen peroxide
HCN	hyperpolarization-activated cyclic nucleotide-gated channel
HIF1α	hypoxia-inducible factor 1 alpha
HK2	hexokinase 2
HMOX1	heme oxygenase 1
ICAM1	intercellular adhesion molecule 1
ICC	immunocytochemistry
ID	identification number
IENFD	intraepidermal nerve fiber density
IgG	immunoglobulin G
IHC	immunohistochemistry
IKBKB	inhibitor of nuclear factor kappa-B kinase subunit beta
IL	interleukin
i.pl.	intraplantar
iPSC	induced pluripotent stem cells
IR	infrared
i.v.	intravenous
KCa3.1	calcium-activated potassium 3.1 channel

kg	kilogram
KI	knockin
KO	knockout
L	length
L3/4/5	vertebral level lumbar 3/4/5
LDHA	lactate dehydrogenase A
lg	ligand
LGALS3	galectin 3
LOX	lysyl oxidase
LRG1	leucine rich alpha-2-glycoprotein 1
Lyso-Gb3	globotriaosylsphingosine
M0	pan-macrophage
M1	pro-inflammatory macrophage
M2	anti-inflammatory macrophage
mg	milligram
min	minute
ml	milliliter
mm	millimeter
mm^2	square millimeter
mM	millimolar
mo	month
MRI	magnetic resonance imaging
mRNA	messenger ribonucleic acid
M.S.	Marlene Spitzel
N_2	nitrogen
NaCl	sodium chloride
NaV	voltage-gated sodium channel
NFATC3	nuclear factor of activated T-cells, cytoplasmic 3
NGF	nerve growth factor
N. isch.	Nervus ischiadicus
NSAID	non-steroidal anti-inflammatory drugs
O_2	oxygen
PBS	phosphate-buffered saline
PBMC	peripheral blood mononuclear cells

PE	polyethylene
PFA	paraformaldehyde
PGP9.5	protein gene product 9.5
PIM1	proto-oncogene Pim1
PNS	peripheral nervous system
PRPH	peripherin
PRR	protein recognition receptor
(qRT) PCR	(quantitative real-time) polymerase chain reaction
(RM) ANOVA	(repeated measurements) analysis of variance
RNA	ribonucleic acid
ROI	region of interest
RPL13A	ribosomal protein L13a
rpm	revolutions per minute
RT	room temperature
S1	vertebral level sacral 1
SC	spinal cord
sec	seconds
SFN	small fiber neuropathy
SLC2A3	solute carrier family 2 member 3
SRT	substrate reduction therapy
STxB	Shiga toxin 1, subunit B
TFRC	transferrin receptor 1
TLR4	toll-like receptor 4
TNFα	tumor necrosis factor alpha
TRPA	transient receptor potential ankyrin
TRPM	transient receptor potential melastatin
TRPV	transient receptor potential vanilloid
TSP1	thrombospondin 1
U	unit
UV	ultraviolet
VEGFα	vascular endothelial growth factor alpha
VIC™-MGB	phosphor amidite-minor groove binder
v/v	percentage by volume
W	width

WT	wild type
ZEMM	Zentrum für Experimentelle Molekulare Medizin

10. List of Figures and Tables

11. Curriculum vitae

……..

Place, Date Signature

12. Publications

Original Articles

Spitzel M., Wagner E., Breyer M., Henniger D., Bayin M., Hofmann L., Mauceri D., Sommer C., Üçeyler N. (2022). Dysregulation of Immune Response Mediators and Pain-Related Ion Channels Is Associated with Pain-like Behavior in the GLA KO Mouse Model of Fabry Disease. *Cells 11*(11), 1730.

Kreß L., Hofmann L., Klein T., Klug K., Saffer N., **Spitzel M.**, Bär F., Sommer C., Karl F., Üçeyler N. (2021). Differential impact of keratinocytes and fibroblasts on nociceptor degeneration and sensitization in small fiber neuropathy. *PAIN* 162(4):p 1262-1272.

Poster presentations at international conferences

Spitzel M., Schindehütte M., Üçeyler N., Sommer C. (2020). The role of hypoxia in the pathophysiology of pain in a mouse model of Fabry disease. EUREKA! 2020 Online Symposium, Würzburg, Germany.

Spitzel M., Sommer C., Üçeyler N. (2021). The contribution of hypoxic and inflammatory pathways in pain generation of Fabry disease. European Neuroscience Conference for Doctoral Students (ENCODS) Online Conference, Glasgow, Scotland.

Spitzel M., Wagner E., Breyer M., Sommer C., Üçeyler N. (2022). The Interplay of Inflammatory Mechanisms and Ion Channel Gene Expression in the Alpha-Galactosidase A-Deficient Mouse Model of Fabry Disease. 7th International Update on Fabry Disease, Würzburg, Germany.

Spitzel M., Klug K., Sommer C., Üçeyler N. (2023). Impact Of Hypoxia On Small Fiber Neuropathy In A Mouse Model Of Fabry Disease. Peripheral Nerve Society (PNS) Annual Meeting, Copenhagen, Denmark.

13. Danksagung

Mein Dank geht an Frau Prof. Dr. Claudia Sommer für das Vertrauen in mich und meine Fähigkeiten, für die Chance an diesem speziellen Projekt arbeiten zu dürfen und für die aufregende Zeit als Doktorandin in ihrer AG. Danke auch an die AG Sommer für die professionelle Unterstützung im Labor und eine schöne Zeit auch im privaten Umfeld.

Mein weiterer Dank geht an Frau Prof. Dr. Nurcan Üçeyler für die unermüdliche Unterstützung in jeglicher Lage, für das Mentoring und dem Wachstum, den ich dank ihr und ihrer AG erfahren durfte.

Den Mitgliedern meines Promotionskomitees, Herrn Prof. Dr. Robert Blum und Frau Prof. Dr. Carmen Ruiz de Almódovar, möchte ich ebenfalls für die professionelle Unterstützung danken. Der wissenschaftliche Input und das Feedback waren besonders wertvoll für mich.

Weiterhin danke ich dem Team rund um das SFB1158 Projekt A10, Herrn Prof. Dr. Mirko Pham und besonders Kampfi, Flo und Magnus. Es ist ein Geschenk mit solchen Kollegen an einem Projekt arbeiten zu dürfen. Danke für eure Unterstützung sowohl beruflich als auch privat.

Mein weiterer Dank geht an Herrn Prof. Dr. Peter Jakob für die Möglichkeit an der EP5 frei arbeiten zu dürfen und besonders an die Mitglieder der EP5 Frau Sabine Voll, Herrn Prof. Dr. Volker Behr und Dr. Patrick Vogel. Ihr habt dazu beigetragen, dass mir die manchmal überwältigende Zeit am Hubland in guter Erinnerung geblieben ist und ich mich wie ein vollwertiges Mitglied gefühlt habe.

Ein besonderer Dank, den man gar nicht in Worte fassen kann, geht an die AG Üçeyler, die mich von Tag 1 adoptiert hat und mir immer das Gefühl gegeben hat Teil des Teams zu sein. Besonders danke ich Katharina K., Thomas K., Franziska, Christoph, Max, Danilo, Daniela, Julia, Nicole und Luisa für eure professionelle Unterstützung im turbulenten Laboralltag, aber noch mehr für den Zusammenhalt in privaten Lebenslagen und besonders während der schwierigen Lockdownzeit. Mit so einem Team lassen sich auch die größten Herausforderungen meistern.

Ein großer Dank geht auch an die technischen Assistenten Frau Barbara Dekant, Frau Lydia Biko, Babsi, Kathleen, Antonia, Sonja, Hiltrud und Bettina. Ohne euch würde nichts im Labor laufen! Eure Hilfe ist einfach unermesslich für mich. Danke für die Hilfe, netten Gespräche und aufschlussreichen Kaffeepausen.

Mein weiterer Dank geht an die Tierpfleger im ZEMM, u.a. Frau Anja Weidner, und besonders im Biozentrum am Hubland. Ihr leistet eine wertvolle Arbeit, die zu sehr unterschätzt wird. Besonders Frau Sarah Hess möchte ich für ihre kompetente und immer lässige Art und Hilfe danken.
Die Liste mit den Menschen, denen ich danken könnte, ist noch lange nicht zu Ende. Allerdings muss auch diese Doktorarbeit zu einem Ende kommen.
Daher danke ich nochmals allen Beteiligten, denen ich während meiner Zeit als Doktorandin begegnet bin, die mich geprägt und mich begleitet haben.
Mein letzter Dank geht an meine Familie und meine Freunde, die mir die Kraft für diese Lebensphase und diese Aufgabe gegeben haben, die stolz auf mich sind und mir immer Mut zugesprochen haben. **DANKE.**